Evaluation of O_3, H_2O, CO and NO_y climatologies simulated by four global models in the upper troposphere–lower stratosphere with the IAGOS measurements

Yann Cohen[1,2], Didier Hauglustaine[2], Nicolas Bellouin[1,3], Marianne Tronstad Lund[4], Sigrun Matthes[5], Agnieszka Skowron[6], Robin Thor[5], Ulrich Bundke[7], Andreas Petzold[7,8], Susanne Rohs[7], Valérie Thouret[9], Andreas Zahn[10], and Helmut Ziereis[5]

[1]Institut Pierre-Simon Laplace, Sorbonne Université/CNRS, Paris, France

[2]Laboratoire des Sciences du Climat et de l'Environnement, LSCE-IPSL (CEA-CNRS-UVSQ), Université Paris-Saclay, 91191 Gif-sur-Yvette, France

[3]Department of Meteorology, University of Reading, Reading, UK

[4]CICERO Center for International Climate Research, Oslo, Norway

[5]Deutsches Zentrum für Luft und Raumfahrt, Institut für Physik der Atmosphäre, Oberpfaffenhofen, Germany

[6]Faculty of Science and Engineering, Manchester Metropolitan University, Manchester, United Kingdom

[7]Forschungszentrum Jülich GmbH, Institute of Energy and Climate Research 8 - Troposphere, Jülich, Germany

[8]Institute for Atmospheric and Environmental Research, University of Wuppertal, Wuppertal, Germany

[9]Laboratoire d'Aérologie, Université de Toulouse, CNRS, UPS, France

[10]Institute of Meteorology and Climate Research, Karlsruhe Institute of Technology, Karlsruhe, Germany

Correspondence: yann.cohen.09@gmail.com

Abstract.

Assessing global models in the upper troposphere (UT) and in the lowermost stratosphere (LS) is an important step towards a better understanding of the chemical composition near the tropopause. For this purpose, the current study focuses on an evaluation of long-term simulations from four chemistry-climate/transport models, based on the In-service Aircraft for a Global Observing System (IAGOS) measurements. Most simulations span over the 1995–2017 period, and follow a common protocol among the models. The assessment focuses on climatological averages of ozone (O_3), water vapour (H_2O), carbon monoxide (CO), and reactive nitrogen (NO_y). In the extra-tropics, the models reproduce the seasonality of ozone, H_2O, and NO_y in both

UT and LS, but none of them reproduces CO springtime maximum in the UT. Tropospheric tracers (CO, H_2O) tend to be underestimated, consistently with an overestimation of cross-tropopause exchanges. Most models systematically overestimate ozone in the UT, and nitrogen oxides (NO_x) background appears as the main contributor to ozone variability across the models. The partitioning between NO_y species changes drastically across the models, and acts as a source of uncertainty on NO_x mixing ratio and on its impacts on atmospheric composition. However, we highlight some well-reproduced geographical variations, as the ITCZ seasonal shifts above Africa, or extratropical ozone (H_2O) in the LS (UT) correlated with the observations. These features are encouraging regarding the simulated dynamics in both layers. The current study confirms the importance of separating the UT and the LS with a dynamical tracer for model results evaluation, and for model intercomparisons.

1 Introduction

The upper troposphere–lower stratosphere (UTLS) is a complex transition region between the troposphere and the stratosphere (Gettelman et al., 2011). Its dynamical structure limits the exchanges of air between the two layers, thus playing an important role in their respective quantities of short-lived tracers as ozone (O_3), water vapour (H_2O), carbon monoxide (CO) and nitrogen oxides (NO_x) that are classified as essential climate variables (Bojinski et al., 2014). The UTLS is also a key region regarding radiative forcing, as its colder temperatures maximize the difference between absorbed and emitted long-wave radiation by several radiatively active species (e.g. Lacis et al., 1990). Changes in greenhouse gas concentrations like ozone and water vapour thus have more impact on surface temperature when they are located at these altitudes (e.g. Iglesias-Suarez et al., 2018; Riese et al., 2012; de F. Forster and Shine, 1997).

NO_x is a necessary ingredient for ozone formation in the troposphere. Its emissions mostly take place at the surface, yet the short NO_x lifetime in the boundary layer limits considerably its transport into the upper troposphere (UT). In contrast, NO_x injected directly into these altitudes contribute significantly to NO_x mixing ratios, lightning in particular (Allen et al., 2010; Cooper et al., 2009), but also aviation, whose traffic has increased since the 1950s (Lee et al., 2021). Due to the lower NO_x background favouring the NO_x-limited regime, NO_x emitted in the upper troposphere is more efficient in producing ozone than in the boundary layer (e.g. Nussbaumer et al., 2023; Hoor et al., 2009, for lightning and aviation respectively). Combined with the presence of water vapour, ozone production enhances the concentrations of hydroxyl radical (OH) which acts as a sink of methane and CO and converts the background sulfur dioxide (SO_2) into sulfate (SO_4), thus enhancing the aerosol production in the UTLS (e.g. Joppe et al., 2024).

Modelling the UTLS behaviour accurately is an important step towards a better representation of its sensitivity to free-tropospheric NO_x emissions. Its main reservoir species (nitric acid, HNO_3) is soluble and can be washed out rapidly in moist

conditions, which acts as a sink of NO_y species. As NO_x are converted back and forth into other NO_y species (mostly HNO_3 at these altitudes, but also PAN, provided that peroxyacetyl radicals are present), HNO_3 scavenging is a sink for NO_x as well. NO_y lifetime thus depends on the model parameterization of precipitation, but also on OH quantities that convert NO_x into HNO_3, hence making NO_y more vulnerable to scavenging. The tropopause height and the cross-tropopause exchanges can

40   be critical parameters as well. As each global chemistry-climate model (CCM) and chemistry-transport model (CTM) has its own chemical scheme, as well as its own convection parameterization, the uncertainties in modelled chemical background partly arise from the intermodel differences. For example, according to the results from ACCMIP (Atmospheric Chemistry and Climate Model Intercomparison Project: Lamarque et al., 2013) modeling experiment, Finney et al. (2016) found a 6.5 ± 4.7 ratio in ozone production efficiency between lightning NO_x (LNO_x) and surface NO_x, the high variability originating mainly

45   from the altitude of LNO_x emissions and on the treatment of volatile organic compounds (VOCs) in the models.

Assessing the models' abilities in reproducing the climatological chemical background in the UTLS provides a degree of confidence in a diversity of model results. Notably, it helps in understanding the sensitivity of the models' responses to the aircraft and lightning emissions in the background conditions. It can also help to identify the modelled physical and chemical processes whose representation needs to be improved. Since the UTLS is not a homogeneous layer, the assessment in this

50   area takes benefit from a separation of the air masses into several categories treated separately. In the extratropics, the UTLS can be divided into an upper troposphere (UT), a transition zone enveloping the tropopause, and a lowermost stratosphere (LMS, or LS as noted hereafter). Ozone and NO_y are abundant in the lowermost stratosphere while CO and water vapour are abundant in the upper troposphere (e.g. Cohen et al., 2018; Stratmann et al., 2016; Petzold et al., 2020; Zahn et al., 2014). Their comparisons with observations in the different layers can thus be used to assess the stratosphere–troposphere exchange. More

55   precisely in the LS, ozone and NO_y can be used to assess the models' ability to reproduce the effects of stratospheric processes as the Brewer–Dobson circulation. CO is mostly emitted by combustion processes, such as biomass burning and surface anthropogenic emissions (aviation being a low CO emitter), and can thus be used to assess surface emissions, convection, and troposphere-to-stratosphere transport. Last, NO_y is emitted by combustion processes and by lightning, thus it can also be used to identify aviation emissions, lightning emissions, or surface emissions uplifted in ascending motions.

60   A wide variety of observation data sets are available and commonly used in model assessments. Satellite measurements regularly cover a large area, but their vertical resolution is too coarse to characterize a region as thin as the UTLS. On the contrary, ozonesondes (Hodnebrog et al., 2011) and Lidar (Light Detection and Ranging) provide regular and accurate vertical profiles but are limited to the vicinity of the ground stations. Airborne campaigns sample the atmospheric composition up to 16 km above sea level, and their merged climatologies (Tilmes et al., 2010) have been used in several multi-model assessments

65 (e.g. Hegglin et al., 2010; Gettelman et al., 2010), but the data are sparse in space and time which limits the representativeness of the measurement climatologies. In the framework of the IAGOS (In-service Aircraft for a Global Observing System: Petzold et al., 2015) research infrastructure, regular in situ measurements on board several commercial aircraft provide accurate information in the extratropical UTLS and the tropical UT, though the very top of the latter is higher than cruise altitudes. The monitoring began in 1994 for ozone and H_2O, 1997 for NO_y, and 2001 for CO, with an abundant sampling in most of the

70 northern extratropics (above and below the tropopause) and several tropical transects.

The IAGOS database has already been involved in model assessments, but either on a short period (Law et al., 2000; Brunner et al., 2003), on a restricted area (Gaudel et al., 2015; Tilmes et al., 2016; Young et al., 2018; David et al., 2019), and/or without a IAGOS mask applied to the model output. For this purpose, the Interpol-IAGOS software (Cohen et al., 2021) projects the whole IAGOS data set onto the model grid, and applies a mask on the non-sampled grid cells. As a first application, it has been

75 used in Cohen et al. (2021) to assess (bi-)decadal climatologies in ozone and CO for the MOCAGE (Josse et al., 2004; Guth et al., 2016) model with monthly output for the Chemistry-Climate Model Initiative (CCMI: Eyring et al., 2013), and to assess climatologies in ozone, water vapour, CO, and NO_y for the LMDZ–INCA model with daily output (Cohen et al., 2023), and has proven useful to highlight some model skills as well as biases, either in the UT and LS separately or in the whole UTLS without airmass distinction.

80 The current study aims to extend the former assessment to the climatologies from long-term simulations from four state-of-the-art CCMs/CTMs involved in the ACACIA (Advancing the Science for Aviation and Climate) European Union project, which focuses on the non-CO_2 effects from subsonic aviation on climate. For this purpose, a multi-model experiment has been performed using a set of runs from five state-of-the-art CCMs or CTMs. This modelling experiment aims to investigate the present-day and future impact of aircraft NO_x and aerosol emissions on the atmospheric composition and therefore on climate,

85 and consists of the analysis of runs with and without aircraft emissions, as presented in companion papers (Cohen et al., in prep; Staniaszek et al., in prep.; Bellouin et al., in prep.). While a companion paper focuses on the present-day sensitivity of the modelled atmospheric composition to aviation emissions (Cohen et al., in prep.), the current paper is a preliminary step consisting of assessing (bi-)decadal climatologies derived from the main run of every model against the IAGOS data, in the UT and the LS separately, as done in Cohen et al. (2023) for the LMDZ–INCA model. The IAGOS database fits particularly well

90 with the ACACIA project since the spatial distribution of the measurements coincides with the aircraft traffic, thus providing essential information on a region where aviation emissions have their strongest impact (Hoor et al., 2009; Hodnebrog et al., 2011, 2012; Søvde et al., 2014; Terrenoire et al., 2022).

In this paper, Section 2 describes the participating models and their output, the common simulation setup, the IAGOS observations, and their use in assessing the model climatologies. The results are shown in Section 3, starting with an overview of the models' biases in the whole area covered by IAGOS (Section 3.1), followed by the analysis of the models' skill in the extratropical UTLS (Section 3.2), then in the tropical UT (Section 3.3). The conclusion of this analysis is provided in Section 4.

2   Materials and methodology

This section presents the tools involved in this study. The first part is dedicated to the description of the setup for the standard runs that are compared to the observations. The second part describes the participating models. The third subsection describes the observation data set and the method used in the assessment of the models.

In this experiment, each model output is projected onto a common grid, with a horizontal resolution of 1.875° E x 1.25° N combining the most resolved longitude and latitude coordinates separately among the models, and a vertical resolution of 20 hPa at cruise altitudes. Initially, the models' vertical resolution at cruise altitudes ranges between 15–20 hPa (EMAC and UKESM1.1) and 25–40 hPa (LMDZ–INCA). As each model output, the common grid has a daily resolution. Except for MOZART3, each model also provided an Ertel potential vorticity field (PV) to separate UT and LS.

2.1   Simulation setup

The historical global anthropogenic emissions are taken from the Community Emissions Data System inventories (CEDS: Hoesly et al., 2018), and the historical biomass burning emissions from the BB4CMIP inventory (biomass burning emissions for CMIP6: van Marle et al., 2017). The emissions after 2014 are taken from the SSP3-7.0 scenario (Gidden et al., 2019). The aircraft emissions are taken from the anthropogenic emissions inventories as well (both historical and future scenarios), after applying the corrections presented in Thor et al. (2023). The historical runs generally cover the period 1994–2017 (2001–2017 for OsloCTM3), providing robust climatologies that are compared with aircraft observations over the same period. In order to assess the model's ability to simulate the mean UTLS composition, it is important to provide simulations with the most realistic transport conditions. This is why the runs from the CCMs are nudged by horizontal winds taken from a reanalysis, indicated in Table 1. Three models are CCMs and are nudged with ERA-Interim (EMAC and LMDZ-INCA) or ERA5 (UKESM1.1), and one model is a CTM forced by the ECMWF OpenIFS product (OsloCTM3), similar to ERA-Interim. The simulation from another CTM participating in the ACACIA project (MOZART3, forced by ERA-Interim) has been included to present the model behaviour during 1997–2007, but the dynamical field is a cyclic repetition of the year 2007, which removes the

Table 1. Description of the participating models. The acronyms and abbreviations are explained here. In the first column, the abbreviations horiz., vert., hom., phot., and het. have the respective meanings: horizontal, vertical, homogeneous, photolytic, and heterogeneous. Among the aerosol categories, SO_4, NO_3, BC, OC, and OM represent respectively sulfate, nitrate, black carbon, organic carbon, and organic matter. In the references, G2001 stems for Grewe et al. (2001), PR92 and PR97 stem for Price and Rind (1992) and Price et al. (1997), O2010 stems for Ott et al. (2010), and P1998 stems for Pickering et al. (1998).

Model	EMAC	LMDZ-INCA	MOZART3	OsloCTM3	UKESM1.1
Operated	DLR	LSCE (IPSL)	MMU	CICERO	UREAD
Model type	CCM (CTM mode)	CCM (CTM mode)	CTM	CTM	CCM (nudged)
Reanalysis	ERA-Interim	ERA-Interim	ERA-Interim	ECMWF OpenIFS	ERA5
GCM	ECHAM5	LMDZ	–	–	UM
Horiz. resolution	2.8°E x 2.8°N	2.5°E x 1.3°N	2.8°E x 2.8°N	2.25°E x 2.25°N	1.875°E x 1.25°N
Vertical levels	90	39	60	60	85
Vert. resolution (hPa) near cruise levels	15–20	25–40	20–25	25–30	15–20
Top level (hPa)	0.010	0.012 (80 km)	0.10	0.10	0.002
Chemistry					
Total species	160	123	108	190	81
Aerosol species	–	23	–	56	
Hom. reactions	265	234	218	263	224
Phot. reactions	82	43	71	61	59
Het. reactions	12	30	–	18	5
Aerosol categories	–	SO_4, NO_3, BC, OC, dust, sea-salt	–	SO_4, NO_3, BC, OC, dust, sea-salt	SO_4, NO_3, BC, OM, dust, sea-salt
Emissions					
Lightning	G2001	PR92; O2010	PR97; P1998	PR92; O2010	PR92 (calibrated)
Biogenic VOCs		ORCHIDEE model	POET	MEGAN-MACC	Dedicated scheme
Biomass burning		BB4CMIP	BB4CMIP	BB4CMIP	BB4CMIP

120 interannual variability of atmospheric transport and thus cannot be treated as a model assessment, except to comment on the seasonality.

2.2 Participating models

In this section, Table 1 summarizes the key model characteristics. In the next sections (Sections 2.2.1–2.2.5), further detail is given for each model, notably the tropospheric and stratospheric chemical schemes implemented in the models.

125 ### 2.2.1 EMAC

The ECHAM/MESSy Atmospheric Chemistry (EMAC) model is a numerical chemistry and climate simulation system that includes sub-models describing tropospheric and middle atmosphere processes and their interaction with oceans, land, and human influences (Jöckel et al., 2010). It uses the second version of the Modular Earth Submodel System (MESSy2) to link multi-institutional computer codes. As described in Jöckel et al. (2016), MESSy is a software package providing a framework

130 for a standardized, bottom-up implementation of Earth system models with flexible complexity (Modular Earth Submodel

System). The core atmospheric model is the 5th generation European Centre Hamburg general circulation model (ECHAM5, Roeckner et al., 2006). The physics subroutines of the original ECHAM code have been modularized and reimplemented as MESSy submodels and have continuously been further developed. Only the spectral transform core, the flux-form semi-Lagrangian large-scale advection scheme, and the nudging routines for Newtonian relaxation remain from ECHAM. For the present study, we applied EMAC (MESSy version 2.55.2) in the T42L90MA-resolution, i.e. with a spherical truncation of T42 (corresponding to a quadratic Gaussian grid of approximately 2.8 by 2.8 degrees in latitude and longitude) with 90 vertical hybrid pressure levels up to 0.01 hPa. In ECHAM5, the nudging applies to vorticity, temperature, logarithm of the surface pressure, and divergence with a relaxation time being 6 h, 24 h, 24 h, and 48 h respectively. Using a so-called quasi chemistry–transport mode (QCTM, Deckert et al., 2011) enables binary identical simulations with respect to atmospheric dynamics and perturbations in chemistry can be detected with a high signal-to-noise ratio. The applied model setup comprised the Module Efficiently Calculating the Chemistry of the Atmosphere (MECCA) used for tropospheric and stratospheric chemistry calculations with the possibility of extending to the mesosphere and oceanic chemistry (Sander et al., 2019). Reaction mechanisms include ozone, methane, HO_x, NO_x, NMHCs, halogens, and sulfur chemistry. Radiative transfer calculations are performed using the submodel RAD (Dietmüller et al., 2016).

2.2.2   LMDZ–INCA

The LMDZ-INCA global chemistry-aerosol-climate model (hereafter referred to as INCA) couples online the LMDZ general circulation model (Laboratoire de Météorologie Dynamique, version 6: Hourdin et al., 2006) and the INCA model (INteraction with Chemistry and Aerosols, version 5: Hauglustaine et al., 2004). The interaction between the atmosphere and the land surface is ensured through the coupling of LMDZ with the ORCHIDEE dynamical vegetation model (ORganizing Carbon and Hydrology In Dynamic Ecosystems, version 9: Krinner et al., 2005). In the present configuration, the model includes 39 hybrid vertical levels extending up to 70 km. The horizontal resolution is 1.25° in latitude and 2.5° in longitude. The primitive equations in the general circulation model (GCM) are solved with a 3-minute time-step, large-scale transport of tracers is carried out every 15 min, and physical and chemical processes are calculated at a 30-minute time interval. For a more detailed description and an extended evaluation of the GCM, we refer to Hourdin et al. (2006).

INCA initially included a state-of-the-art CH_4-NO_x-CO-NMHC-O_3 tropospheric photochemistry (Hauglustaine et al., 2004; Folberth et al., 2006). The tropospheric photochemistry and aerosols scheme used in this model version is described through a total of 123 tracers including 22 tracers to represent aerosols. The model includes 234 homogeneous chemical reactions, 43 photolytic reactions, and 30 heterogeneous reactions. The gas-phase version of the model has been extensively compared to

observations in the lower troposphere and the upper troposphere. For aerosols, the INCA model simulates the distribution of aerosols with anthropogenic sources such as sulfates, nitrates, black carbon, and particulate organic matter, as well as natural aerosols such as sea salt and dust. Ammonia and nitrate aerosols are considered as described by Hauglustaine et al. (2014). The model has been extended to include an interactive chemistry in the stratosphere and mesosphere. Chemical species and reactions specific to the middle atmosphere were added to the model. A total of 31 species were added to the standard chemical scheme, mostly belonging to the chlorine and bromine chemistry, and 66 gas-phase reactions and 26 photolytic reactions (Terrenoire et al., 2022; Pletzer et al., 2022).

In this study, meteorological data from the European Center for Medium-Range Weather Forecasts (ECMWF) ERA-Interim reanalysis have been used to constrain the GCM meteorology and allow a comparison with measurements. The relaxation of the GCM winds towards ECMWF meteorology is performed by applying at each time step a correction term to the GCM zonal and meridional wind components with a relaxation time of 3.6 h. The ECMWF fields are provided every 6 hours and interpolated onto the LMDZ grid.

The ORCHIDEE vegetation model has been used to calculate offline the biogenic surface fluxes of isoprene, terpenes, acetone, and methanol as well as NO soil emissions as described by Messina et al. (2016). The lightning NO_x parameterization is described in Jourdain and Hauglustaine (2001). The lightning frequency follows the parameterization from Price and Rind (1992). In this simulation, a rescaling constrains the mean global flash rate at 46.3 flash yr^{-1}, consistent with the annual climatologies derived from both Lightning Imaging Sensor and Optical Transient Detector (LIS–OTD) satellite instruments in Cecil et al. (2014), from 1995 until 2010. This rescaling accounts for the different LIS and OTD sampled latitude bands, and their different sampling periods. The lightning NO_x (LNO_x) emissions are then redistributed vertically, based on Ott et al. (2010).

2.2.3 MOZART3

Model for OZone And Related chemical Tracers, version 3 (MOZART3) is an offline, global chemical transport model, extensively evaluated (Kinnison et al., 2007) and used for a range of various applications (Liu et al., 2009; Wuebbles et al., 2011), including studies dealing with the impact of aviation emissions on atmospheric composition (Søvde et al., 2014; Skowron et al., 2015). MOZART3 accounts for advection based on the flux-form semi-Lagrangian scheme (Lin and Rood, 1996), shallow and mid-level convection (Hack, 1994), deep convective routine (Zhang and McFarlane, 1995), boundary layer exchanges (Holtslag and Boville, 1993), or wet and dry deposition (Brasseur et al., 1998; Müller, 1992).

The model reproduces detailed chemical and physical processes from the troposphere through the stratosphere. The chemical mechanism consists of 108 species, 218 gas-phase reactions, and 71 photolytic reactions including the photochemical reactions associated with organic halogen compounds. The species included within this mechanism are members of O_x, NO_x, HO_x, ClO_x, and BrO_x chemical families, along with CH_4 and its degradation products. A non-methane hydrocarbon oxidation scheme is also represented. The kinetic and photochemical data is based on the NASA/JPL evaluation (Sander et al., 2006).

The horizontal resolution used in this study is T42 (2.8° x 2.8°) and vertically the model domain spans 60 layers between the surface and 0.1 hPa. Vertical resolution is 700–900 m at aircraft cruise altitudes (250–200 hPa). The transport of chemical compounds as well as the hydrological cycle is driven by the meteorological fields from ECMWF Interim 6-h reanalysis (ERA-Interim).

The surface and aviation emissions represent the years 2014–2018. The anthropogenic and biomass burning emissions are taken from CEDS version 2021 and GFEDv4, respectively, while the biogenic emissions are taken from POET (Granier et al., 2005). The parameterization of NO_x emissions from lightning follows the assumption that the lightning frequency depends on the convective cloud top height and the ratio of cloud-to-cloud versus cloud-to-ground lightning depends on the cold cloud thickness (Price et al., 1997). The lightning NO_x emissions are distributed vertically through the convective column according to observed profiles based on Pickering et al. (1998). The lightning source is scaled to provide a total of 4.7 Tg(N) yr^{-1}, with daily and seasonal fluctuations based on the model meteorology. The patterns of lighting NO_x distribution in MOZART3 show a general agreement with LIS and OTD climatology datasets (Skowron et al., 2021). Simulations were preceded by a one-year spin-up.

2.2.4 OsloCTM3

OsloCTM3 is a global, offline chemical transport model, driven by 3-hourly meteorological forecast data from the European Centre for Medium-Range Weather Forecasts (ECMWF) Integrated Forecast System (IFS) model (Søvde et al., 2012). The default horizontal resolution is 2.25° x 2.25°, with an option to run at 1° x 1°. In the vertical, the model has 60 levels with the uppermost centered at 0.1 hPa. The model code is openly available from Github: https://github.com/NordicESMhub/OsloCTM3.

The chemistry of the OsloCTM3 covers both tropospheric and stratospheric chemistry, treated by separate modules (Berntsen and Isaksen, 1997; Stordal et al., 1985). The tropospheric code is stand-alone, but the stratospheric code needs the tropospheric chemistry module to work. The kinetics are based on JPL 2006 (Sander et al., 2006), while the photodissociation coefficients are calculated online using the Fast-JX scheme (Prather, 2009). The numerical integration of chemical kinetics is done by applying the Quasi Steady State Approximation (QSSA: Hesstvedt et al., 1978), using three different integration methods

depending on the chemical lifetime of the species. The model also treats the main anthropogenic and natural aerosol species

215 (sulfate, nitrate/ammonium, black carbon, primary and secondary organic aerosol, dust, and sea salt). The aerosol schemes are described in more detail in Lund et al. (2018).

The model transport covers large-scale advection treated by the second order moments (SOM) scheme (Prather, 1986), convective transport based on Tiedtke (1989), and boundary layer mixing based on Holtslag et al. (1990). Scavenging covers dry deposition, i.e. uptake by soil or vegetation at the surface, and washout by convective and large-scale rain (Søvde et al.,

220 2012).

For ACACIA, the output is made of a succession of one-year simulations, each one with 6 months spin-up. Anthropogenic emissions are from CEDS version 2021 with GFEDv4 biomass burning and MEGAN-MACC year 2010 biogenic emissions. Lightning NO_x emissions are calculated online (Søvde et al., 2012), as are dust and sea salt fluxes (Lund et al., 2018, and references therein).

225 Lightning NO_x emissions are calculated from the convective fluxes provided by the meteorological input data using the algorithm based on cloud-top height from Price and Rind (1992), with a scaling that matches lightning flash rates observed by OTD and LIS. The in-cloud flash rate depends on whether the surface is land or ocean. The model distributes LNO_x emissions vertically through the convective column according to observed profiles (Ott et al., 2010) for 4 world regions. These profiles are scaled vertically to match the height of each convective plume in the CTM and already account for vertical mixing of lightning

230 NO_x within the cloud. Geographic region definitions are from Allen et al. (2010) and Murray et al. (2012).

2.2.5 UKESM1.1

The U.K. Earth System Model version 1 (UKESM1: Sellar et al., 2019) is a global climate model made by coupling atmosphere, ocean, sea ice, and land surface models. In this study, UKESM1 is used in its atmosphere-only configuration, where ocean sea-surface temperature and sea ice distributions are prescribed from previous simulations with the fully coupled model. The

235 atmosphere model is built on the Met Office Unified Model (Walters et al., 2019), decomposing the atmosphere in 85 terrain-following hybrid vertical levels up to an altitude of 85 km. The horizontal resolution is $1.25° \times 1.875°$.

Atmospheric chemistry is simulated by the stratosphere–troposphere StratTrop chemistry scheme (Archibald et al., 2020) of the UK Chemistry and Aerosols (UKCA) sub-model. StratTrop unifies two originally separate tropospheric and stratospheric chemistry modules, described by O'Connor et al. (2014) and Morgenstern et al. (2009), respectively. StratTrop simulates O_x,

240 HO_x, and NO_x chemistry based on 15 emitted species, including NO, CO, and aerosol precursor gases, and 7 long-lived species including CH_4, which are constrained by surface concentrations. Tracer advection, convective transport, and boundary

layer mixing are simulated by the Unified Model (Walters et al., 2019). Wet deposition follows Giannakopoulos et al. (1999), while dry deposition depends on the surface types simulated by the land surface model, as described in Archibald et al. (2020). Photolysis rates are computed interactively by the Fast-JX scheme (Neu et al., 2007) depending on three-dimensional radiation. In terms of aerosols, UKCA simulates the mass and number of sulfate, nitrate, black carbon, primary and secondary organic, mineral dust, and sea salt aerosols (Mulcahy et al., 2018). Horizontal winds are nudged with a relaxation time of 6 h.

Lightning NO_x emissions are described in section 2.6.3 of Archibald et al. (2020). They are calculated following Price and Rind (1992), where lightning flash density depends on cloud top height and surface type (land or ocean). The scheme distinguishes the energy discharged by cloud-to-cloud and cloud-to-ground flashes and uses a spatial calibration factor to make the scheme independent of model resolution. The scheme is only applied when cloud depth reaches at least 5 km according to the convection scheme. NO_x emissions are distributed linearly with the logarithm of pressure. They have been calibrated to reach an average global annual emission rate of 5.98 TgN yr^{-1} over the period 2005–2014.

In this study, UKESM1 simulated the period 1990–2018, using CMIP6 historical and, from 2015 onwards, SSP3-7.0 emissions as monthly distributions. The CMIP6 aircraft emission inventories were corrected for the mistake identified by Thor et al. (2023). Emissions of sea-salt and mineral-dust aerosols, and biogenic VOCs, are interactive. The model was nudged to 6-hourly horizontal wind speed distributions from ERA5.

2.3 The IAGOS data

The IAGOS research infrastructure (http://www.iagos.org, last access: November 2022) provides long-term routine in situ observations of chemical species on board a fleet of several passenger aircraft. Its predecessors MOZAIC (Measurements of water vapor and OZone by Airbus In-service airCraft: Marenco et al., 1998) and CARIBIC (Civil Aircraft for the Regular Investigation Based on an Instrument Container: Brenninkmeijer et al., 1999, 2007; Stratmann et al., 2016) relied on the same principle. The MOZAIC measurements began on board five equipped aircraft measuring ozone and water vapour in August 1994. CO observations began in December 2001 and NO_y measurements were operational on one aircraft between April 2001 and May 2005. CARIBIC samples a wide variety of atmospheric species since 1997 from one single aircraft, including the ones measured by MOZAIC. Since the merge of the two programs in 2008, their respective databases are referred to as IAGOS-CORE and IAGOS-CARIBIC. In the present study, we consider them as a single database called IAGOS hereafter, an approach validated by Blot et al. (2021) for ozone and CO. The period we are analyzing spreads from Aug. 1994 until Dec. 2017, hence the 1994–2017 (or 2001–2017) period covered by the models' run. The most sampled altitudes are between 180 and 310 hPa,

and the vertical distribution of sampling varies geographically. The methodology used for the models' assessment using the IAGOS data is described in Section 2.4.

The main characteristics of the IAGOS instruments relevant to this study are indicated in Table 2. Concerning the IAGOS-CORE instruments, further information is available in Thouret et al. (1998) for ozone, in Nédélec et al. (2003); Nédélec et al. (2015) for CO, in Helten et al. (1998); Neis et al. (2015a, b); Rolf et al. (2023) for water vapour, and in Volz-Thomas et al. (2005); Pätz et al. (2006) for NO_y. Note that the IAGOS-CORE water vapour measurements have an accuracy of 6 % RHL (relative humidity with respect to liquid water) in the vicinity of the mid-latitude thermal tropopause (Smit et al. (2014); Petzold et al. (2020)). Due to a moist bias in the IAGOS-CORE H_2O observations for the driest air masses (RHL < 5 %) which are encountered in the lower stratosphere, this study does not quantify the model H_2O biases elsewhere than in the upper troposphere. Concerning the IAGOS-CARIBIC instruments, further information is available in Zahn et al. (2012) for ozone, in Scharffe et al. (2012) for CO, in Zahn et al. (2014); Dyroff et al. (2015) for water vapour, and in Ziereis et al. (2000); Stratmann et al. (2016) for NO_y. More precisely, the latter has a total measurement uncertainty of 6.5 % (8 %) for a measured mixing ratio of 1 ppb (0.5 ppb). For both programs, the time response of the water vapour sensors decreases with the measured water content.

Table 2. Characteristics of the IAGOS instruments measuring ozone, CO, water vapour, and NO_y. The last column shows the time period covered by the measurements. The periods ending with a hyphen mean that the measurements are still ongoing.

Observation system	Species	Instrument	Accuracy	Precision	Time response	Period
IAGOS-CORE	O_3	UV absorption spectrometer	2 ppb	2 %	4 s	1994–
	CO	IR absorption spectrometer	5 ppb	5 %	30 s	2001–
	H_2O	Capacitive hygrometer	5 % RHL		5–300 s	1994–
	NO_y	Chemiluminescence gold converter	5 ppt	5 %	4 s	2001– 2005
IAGOS-CARIBIC	O_3	Dry chemiluminescence detector & UV absorption spectrometer	1.5 ppb	1 %	0.2 s 4 s	1997– 1997–
	CO	UV resonance fluorescence	< 2 ppb	1–2 ppb	2 s	1997–
	H_2O	Photoacoustic laser spectrometer & frost-point hygrometer	< 1 ppm	< 3 %	4–20 s 5–90 s	1997– 1997–
	NO_y	Chemiluminescence gold converter	6.5–8 %		1 s	1997–

2.4 Methodology for assessing modelled mixing ratios of chemical species in the UTLS

The Interpol-IAGOS software (Cohen et al., 2021) aims to facilitate the assessment of the model output with the IAGOS data by deriving two respective products that are directly comparable. It consists of a projection of the scattered IAGOS data onto the regular model grid, day by day, followed by a monthly average. For a given model, the subsequent gridded IAGOS

product is then denoted as IAGOS-DM-model, the -DM suffix referring to the distribution onto the model grid. For further simplicity in this study, we refer to it as IAGOS–model, and the IAGOS-DM-model products in their ensemble are called "IAGOS–DM products". Concerning the model output, a daily mask is applied with respect to the IAGOS sampling (Cohen et al., 2023), excluding the non-sampled daily gridpoints. This way, the subsequent monthly products are representative of the same gridpoints and the same days. As in Cohen et al. (2023), their whole name is model–M (the –M suffix referring to the IAGOS mask), but except in this section where there can be confusion, we refer to it simply using the model name. The monthly average is calculated for each layer separately. It implies that for each grid cell included in both UT and LS during a month, a monthly average is calculated for both layers. Last, the seasonal and annual climatologies are then derived from the monthly means with the same method and filtering as in Cohen et al. (2023). For each model, the couple of products IAGOS-DM-model and model–M are thus representative of the same time period as well.

For each model, the tropopause is defined dynamically as the isosurface of 2 PVU (potential vorticity units) derived from the model output. The UT spreads from 400 hPa up to the tropopause level but excludes the top grid cell in order to avoid the strongest mixing zone, directly impacted by both layers (e.g. Thouret et al., 2006; Cohen et al., 2018). The LS corresponds to all the sampled grid cells above the 3 PVU isosurface. In order to limit the impact of errors in the modelled PV on the evaluation, we exclude the cases where the modelled PV value and the daily average of the observed ozone mixing ratios are very likely to represent different layers. As in the previous studies (Cohen et al., 2021, 2023), a daily grid cell in the UT (LS) is filtered out when the average ozone from IAGOS is more than 140 ppb (less than 60 ppb). Last, the non-separated UTLS represents all the measurement points above 400 hPa, and has been added to this paper in order to include the output from the MOZART3 model without a PV field. In the tropics, the tropopause altitude does not allow the aircraft to sample stratospheric air masses. Consequently, only the upper troposphere is represented between 25° S and 25° N, and includes all the measurements above 300 hPa, though the uppermost part of the tropical troposphere remains higher than cruise altitudes. In the framework of the CCMI modeling experiment, Orbe et al. (2020) reports that the nudging process tends to enhance the transport variability between the CCMs and can generate artificial transport in regions of strong gradients. This issue might be partly addressed by our methodology, notably the definition for the layers that enhances the isolation between them, and the exclusion of the grid cells with an inconsistent PV value regarding ozone observations. The mean pressure differences between observations and the model 2-PVU tropopause shown in Supplementary Material (Figs. S1–S5) do not exhibit noticeable differences between the models: mostly, they are less than 5 hPa (except in winter and spring for ozone and NO_y), and are always less than 10 hPa. It might still be problematic for water vapour in the LMS as the vertical gradient from the tropopause is particularly high, including two orders of magnitude (Zahn et al., 2014), but as described above, the model skills do not cover water vapour in

Table 3. Characteristics of the chosen tropical regions.

Region	Delimitation	Set of seasons
South America/Atlantic Ocean	60° W–15° W	DJF–MAMJ–JA–SON
Africa	5° W–30° E	DJFM–AM–JJASO–N
South Asia	60° E–90° E	DJF–MAM–JJAS–ON

the LMS. For each species and layer, the distance between the sampled grid cells and the tropopause does not vary enough across the models to play a significant role in the inter-model discrepancies, as there is no visible correlation with the chemical tracers.

As in Cohen et al. (2023), the chosen metrics are the modified normalized mean bias (MNMB) with the fractional gross error (FGE), and Pearson's correlation coefficient, all defined in Supplementary Material (Eqs. S1–S4). Since the models have different PV fields and some of them have a different time period, each model is compared to its own IAGOS–model reference product. This study is divided into comparisons in the extratropics and in the tropics. The results in the extra-tropics are generally represented with several sets of metrics (quantiles, biases, and linear regression metrics). On the contrary, as the sampling in the tropics is more heterogeneous, three regions have been chosen as in Cohen et al. (2023) and are represented with mean zonal cross sections: West Atlantic–South America (called South America hereafter), Africa and South Asia. Respectively, their zonal cross sections are averaged through the following longitude bands: 60° W–15° W, 5° W–30° E, and 60° E–90° E, as a compromise between an efficient sampling and a spatial uniformity for the observed species. For each of these regions, the year is divided into seasons that depend on the mean position of the intertropical convergence zone (ITCZ). As in Cohen et al. (2023), the tropical season definitions were based on the months with the northernmost and southernmost position of the ITCZ (located with the observed horizontal winds and water vapour), as an extension of Lannuque et al. (2021) that focused on Africa. They are summarized in Table 3 taken from Cohen et al. (2023).

3 Modelled reactive species compared to IAGOS observational data

This section is divided into two approaches. We first present introductory results showing global annual maps of model mean biases, then treat more precisely the northern extra-tropics in the UT and the LS separately and, to a lesser extent, in the non-separated UTLS, and finally move into the (sub-)tropical UT characterization. It is worth reminding that the principal criterion for the UT and LS definition beyond $\pm 25°$ N is the 2-PVU isosurface from the nudged CCMs/forced CTM, and that the tropical UT comprises every sampled grid cell above 300 hPa (as our sampling does not reach the tropical tropopause layer).

3.1 Horizontal distributions

The annual climatologies of the model biases in the UT and the LS are shown in Figs. 1–4 for the four models with an available PV field. A climatology is also shown for one of the gridded IAGOS products (called hereafter IAGOS–DM products, see Section 2.4) in order to provide a view of the expected features, but each bias remains relative to a different IAGOS–DM product, notably because of the different time periods. Since the IAGOS–DM climatologies are relatively similar through the simulations with the same duration (not shown), we chose only one of the IAGOS–DM climatologies with the longest time period (by default IAGOS–EMAC, i.e. the gridded IAGOS product on EMAC model's grid, as explained in Section 2.4). We can notice the sampling differences between the climatologies from OsloCTM3 (2001—2017) and the other three assessed models (1994-–2017). Interannual variability is therefore likely to cause moderate differences in the observed climatologies for ozone and water vapour in OsloCTM3, which time period is 25 % shorter than for the other models. It does not apply to CO and NO_y as their IAGOS-CORE observations started in 2001.

On a yearly average, we first notice common features between the models. The four models exhibit a geographical anticorrelation between ozone and CO biases in the LS (Figs. 1 and 2). The O_3/CO ratio shown in Fig. A1 summarizes well this pattern by an MNMB decreasing with latitude. On the other hand, upper-tropospheric ozone is overestimated in the mid-latitudes, whereas CO tends to be underestimated. These combined features suggest that the four models tend to overestimate the overall impact of stratosphere–troposphere exchanges across the extratropical tropopause. Most of the models also overestimate ozone in the tropics, which is analyzed in detail in Sect. 3.3. We can notice that the models showing a more positive (negative) bias in ozone (CO) in the low-latitude LS have the same tendency in the tropical UT, possibly as an impact of isentropic cross-tropopause exchanges that can extend biases to the adjacent layer. Figure 3 shows that contrary to the other species, each model NO_y climatology is simultaneously characterized by either low and high biases, but few grid cells with a weak bias. The map derived from the observations is heterogeneous too, with upper-tropospheric minima over Northwest America, the North Atlantic corridor, and near the Azores anticyclone (less than 400 ppt). A regional-scale maximum is visible over Northeast America (800–1400 ppt) and tropical Africa. The four models generally underestimate the magnitude of these geographical extrema, showing too small variability. Last, in Fig. 4, upper-tropospheric water vapour tends to be underestimated in the northern extratropics and, at least, in the northern tropics.

3.2 Northern extra-tropics

In this subsection, we compare and characterize the observation and model seasonal cycles together, then show synthesizing metrics to assess the model geographical distributions in the extra-tropics. Figures 5–8 provide an overview of the seasonal

O₃ − Whole year
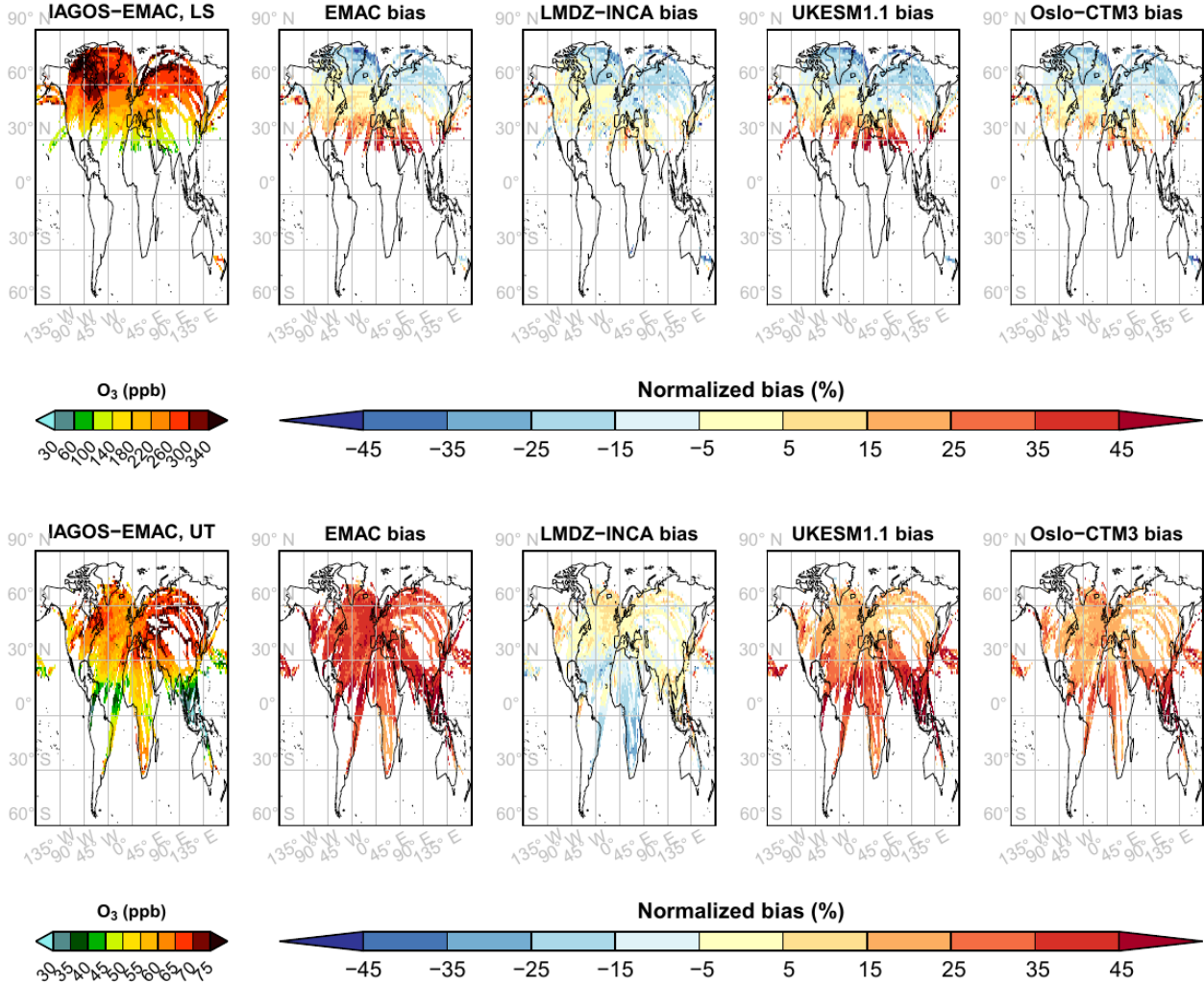
Figure 1. Ozone mean horizontal distributions on annual averages from December 1994 until November 2017, for the IAGOS–EMAC product (left) and the biases for the masked output from EMAC, LMDZ–INCA, UKESM1.1, and OsloCTM3 (from left to right) normalized with respect to the mean values between each model output and their corresponding IAGOS–DM product, in the UT (bottom) and the LS (top).

CO − Whole year
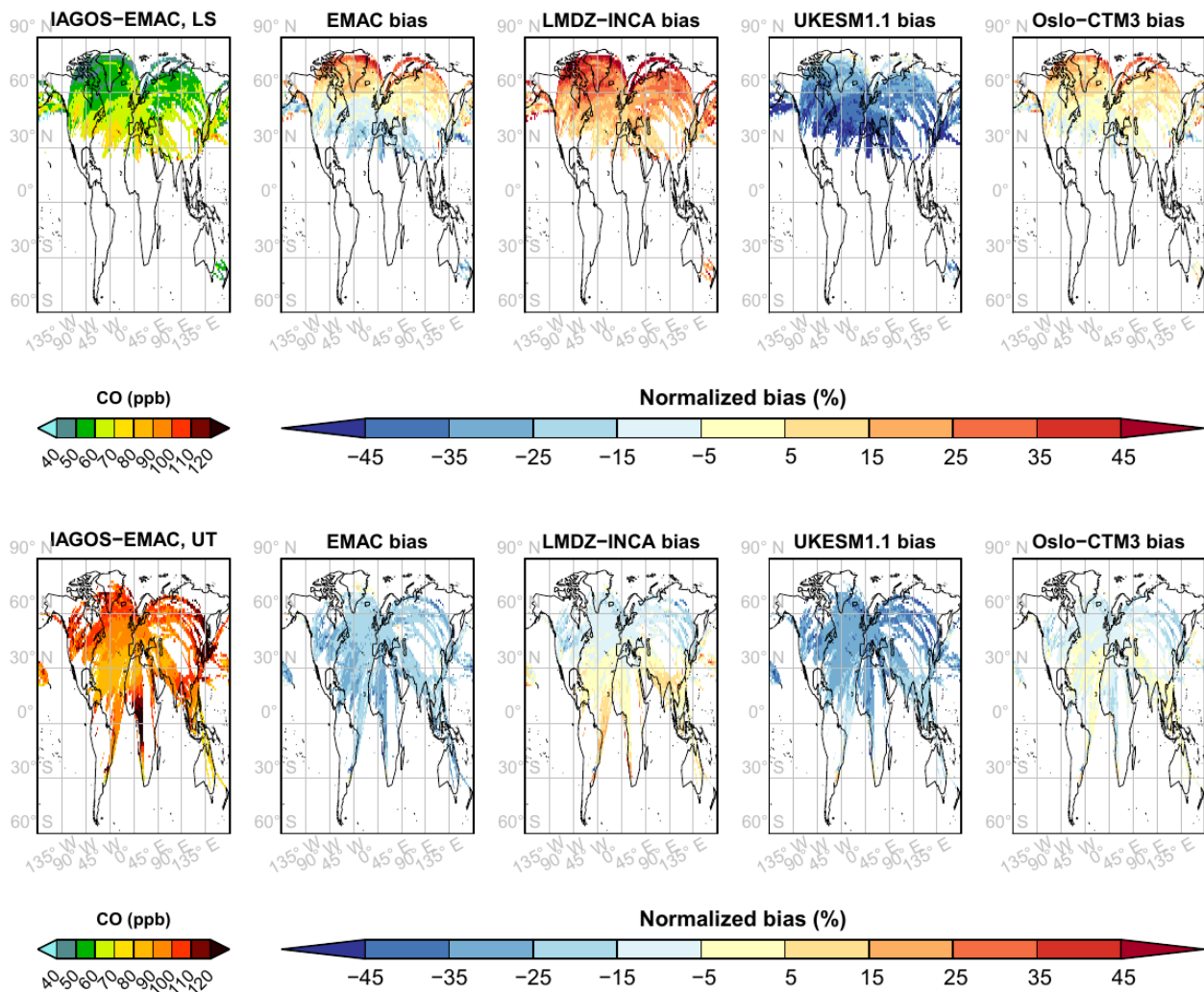
Figure 2. Same as Fig. 1 for carbon monoxide, over the period 2002–2017.

NO$_y$ − Whole year
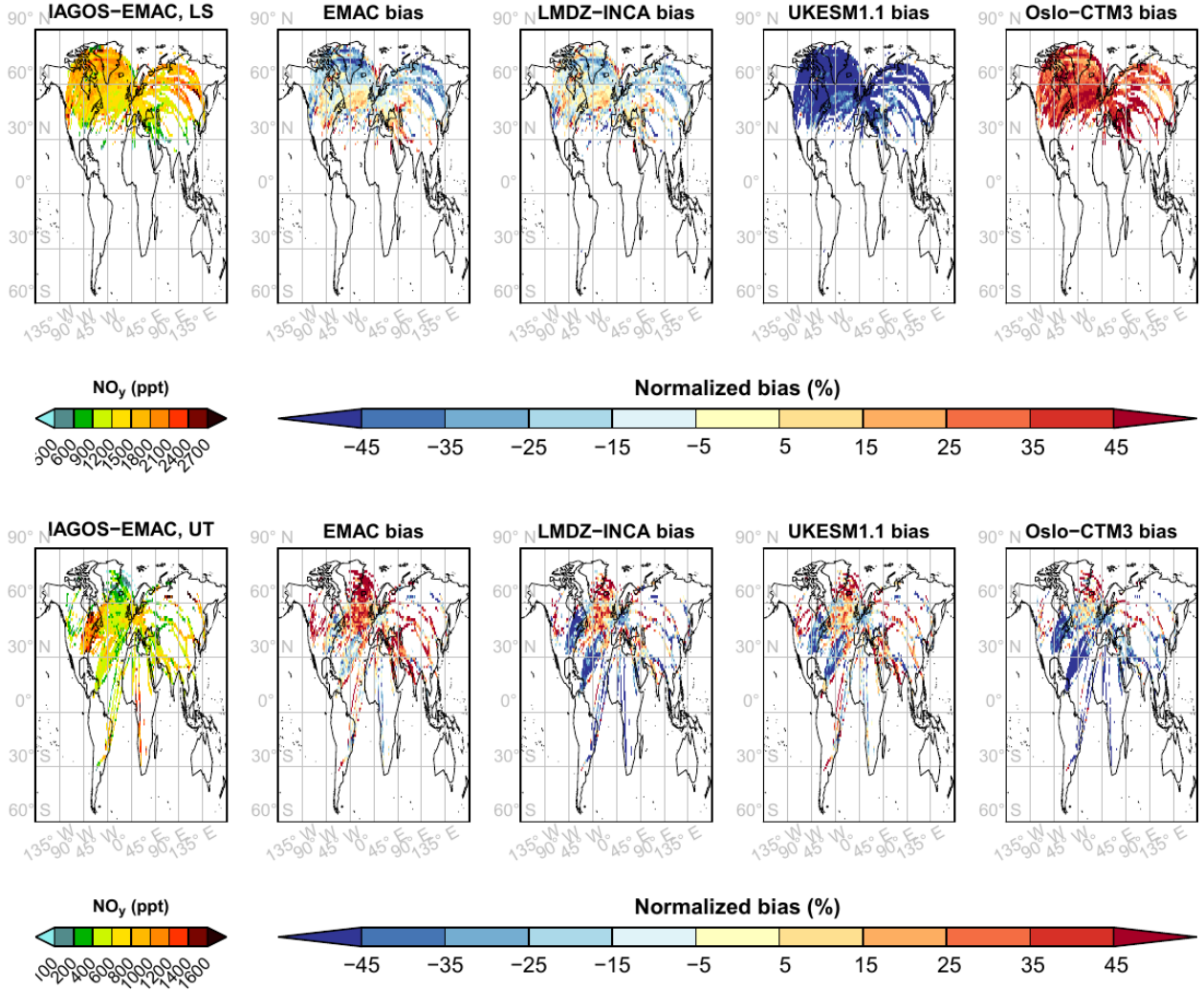
Figure 3. Same as Fig. 1 for nitrogen reactive species, over the period 1997–2017 but with a more frequent sampling over the period 2001–2005.
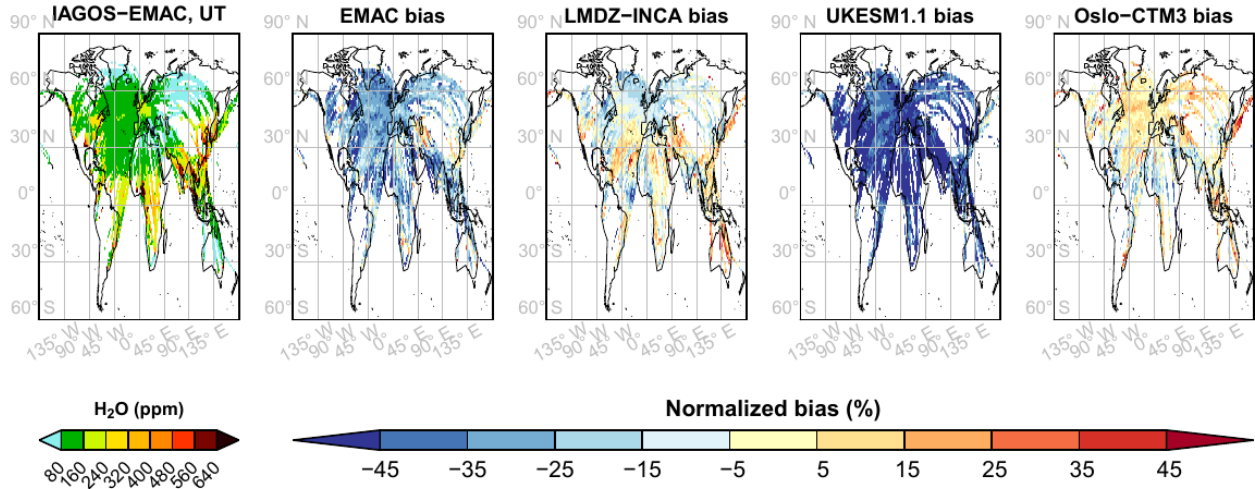
Figure 4. Same as Fig. 1 for water vapour in the upper troposphere.

climatologies in the UT and the LS, and Fig. 9 in the non-separated UTLS. Please note that observed lower-stratospheric water vapour in Fig. 5 is displayed as an indication for the seasonality, but due to the reasons explained in Sect. 2.3, part of its values are probably overestimated and it cannot serve for a bias quantification. The height of the boxplots illustrates the geographical variability. Water vapour seasonality in the UT shown in Fig. 5 is well approximated in the simulations, with a wintertime minimum and a summertime maximum directly linked with convection and temperature that governs saturation vapour pressure. The lower stratosphere shows a similar pattern, though the contrast between the summertime water vapour maximum and the rest of the year is more pronounced than in the UT. This feature is consistent with the increased impact from the troposphere during this season, and the extremely steep vertical gradient in water vapour. Based on CARIBIC measurements between 2005 and 2013, Zahn et al. (2014) found that the summertime maximum was primarily due to shallow cross-tropopause mixing in the extratropics. It takes place during all the year, thus the summertime H_2O maximum in the UT increases the upward moisture flux. The other two pathways for moisture transport into the LS, i.e. localized deep convection events and, higher in the LS, quasi-isentropic mixing with the tropical transition layer (TTL), mostly take place during summer (and early autumn for the latter) but were found to have a lesser contribution to the summertime moisture maximum.

The models have more difficulties in reproducing CO seasonality, according to Fig. 6. The observed springtime peak has been explained by an accumulation of CO in the lower troposphere during winter followed by an increase in the convective transport during spring (Cohen et al., 2018), then allowing the lower-tropospheric CO reservoir to impact the UT. This springtime maximum is not visible in the simulations, its magnitude is underestimated as well, and contrary to the observations, the

springtime distribution is similar to winter, a feature that extends up to the LS. The comparison with the realistic water vapour cycles in the UT tends to exclude convective transport from the causes of this discrepancy, except pyroconvection. It is possible that CO lifetime or CO emissions are underestimated, which reduces the wintertime accumulation in the lower troposphere and then upward CO flux during spring. The lower values in the two tropospheric tracers (H_2O and CO) in both UT and LS with UKESM1.1 suggest an underestimation in the upward fluxes from the surface up to the UT, which favours an underestimation in the LS too.

Figure 7 shows that in the upper troposphere, ozone maximum takes place in summer with a peak in photochemical activity, and the minimum during winter. In the lowermost stratosphere, ozone maximum takes place during spring with the effects of the descending branch of the Brewer–Dobson circulation, transporting ozone-rich air masses down from the deeper extratropical stratosphere, whereas the minimum takes place during fall. The models reproduce well these features, but also the dichotomy in the UT between high-ozone seasons (spring and summer) and low-ozone seasons (winter and fall). Though most models are positively biased, the magnitude of the seasonal cycle is similar to the observations. In the LS, ozone distribution is harder to reproduce during summer and fall, with a geographical variability only spreading over the lower half of the observed distribution. It is characterized by a tendency to overestimate the low-latitude ozone minima and underestimate the high-latitude ozone maxima (e.g. Fig. 1). Similarly with ozone, both observed and modelled NO_y mixing ratios show a springtime maximum in the LS and a summertime maximum in the UT. In the UT, the summertime maximum is linked to photochemical activity, enhanced lightning frequency, more intense boreal forest fires, and enhanced convection that uplifts diverse ozone precursors from the lower troposphere. It is consistent with the detailed individual NO_y species in Figs. B1–B3, where each of the models generally shows a summertime maximum in NO_x, PAN, and especially HNO_3. The latter is notably affected by the conversion from NO_x with the photochemical activity (Stratmann et al., 2016). In the LS, the impact of the Brewer–Dobson circulation coupled with HNO_3 production from nitrous oxide decomposition in the stratosphere is reproduced, as shown in Fig. B3. The only exception is the UKESM1.1 model that rather shows an upper-tropospheric seasonality in the LS, though the influence of the Brewer–Dobson circulation remains visible through more elevated springtime mixing ratios compared to the UT seasonal cycle. On the contrary, the OsloCTM3 model shows higher NO_y values in the LS. As ozone amounts are within the same range as the other models, it excludes the stratospheric circulation from the possible causes of NO_y discrepancies. For UKESM1.1 (OsloCTM3), the lower (higher) HNO_3 values in the LS (Fig. B3) might thus be due to an underestimation (overestimation) of N_2O flux into the stratosphere, to overestimated (underestimated) N_2O lifetime in the stratosphere, or to underestimated (overestimated) HNO_3 lifetime against stratospheric aerosol uptake. The latter is a possible contributor for OsloCTM3, as its mass density of particular sulfate and nitrate is lower by 10 % than in the LMDZ-INCA simulation. Lower
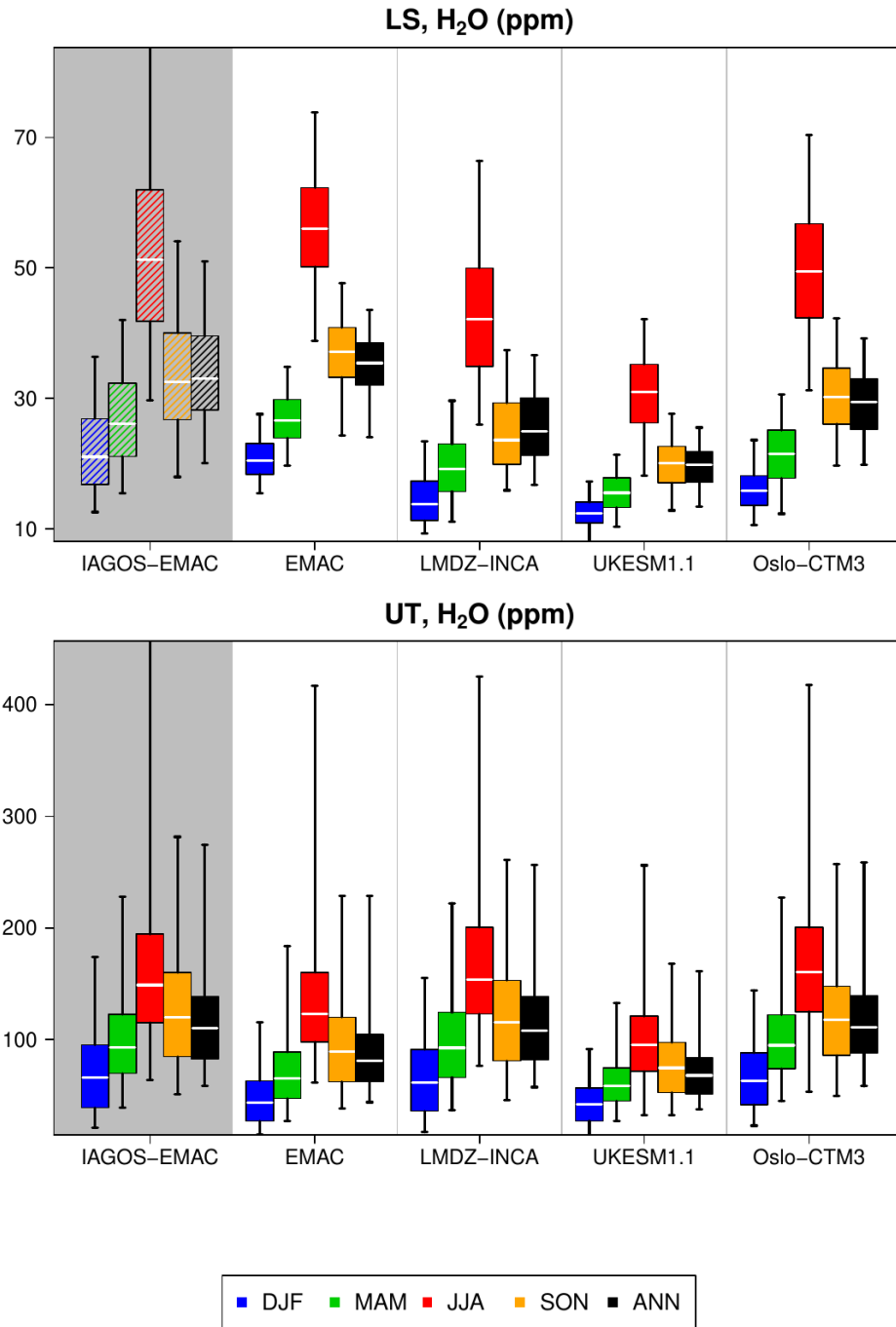
Figure 5. Boxplots synthesizing the mean geographical distribution in extratropical water vapour in the LS (top) and the UT (bottom), for the IAGOS–EMAC product and for the model products (from left to right). Each color corresponds to a season, and the black boxes represent the annual means. For a given boxplot, the white line represents the median, the box corresponds to the interquartile interval, and the whiskers represent the values between the 5 and 95 percentiles. Please note that due to its uncertainty, the observed H_2O in the LS shown here cannot be used for accurate quantification, hence the dashed boxplots.
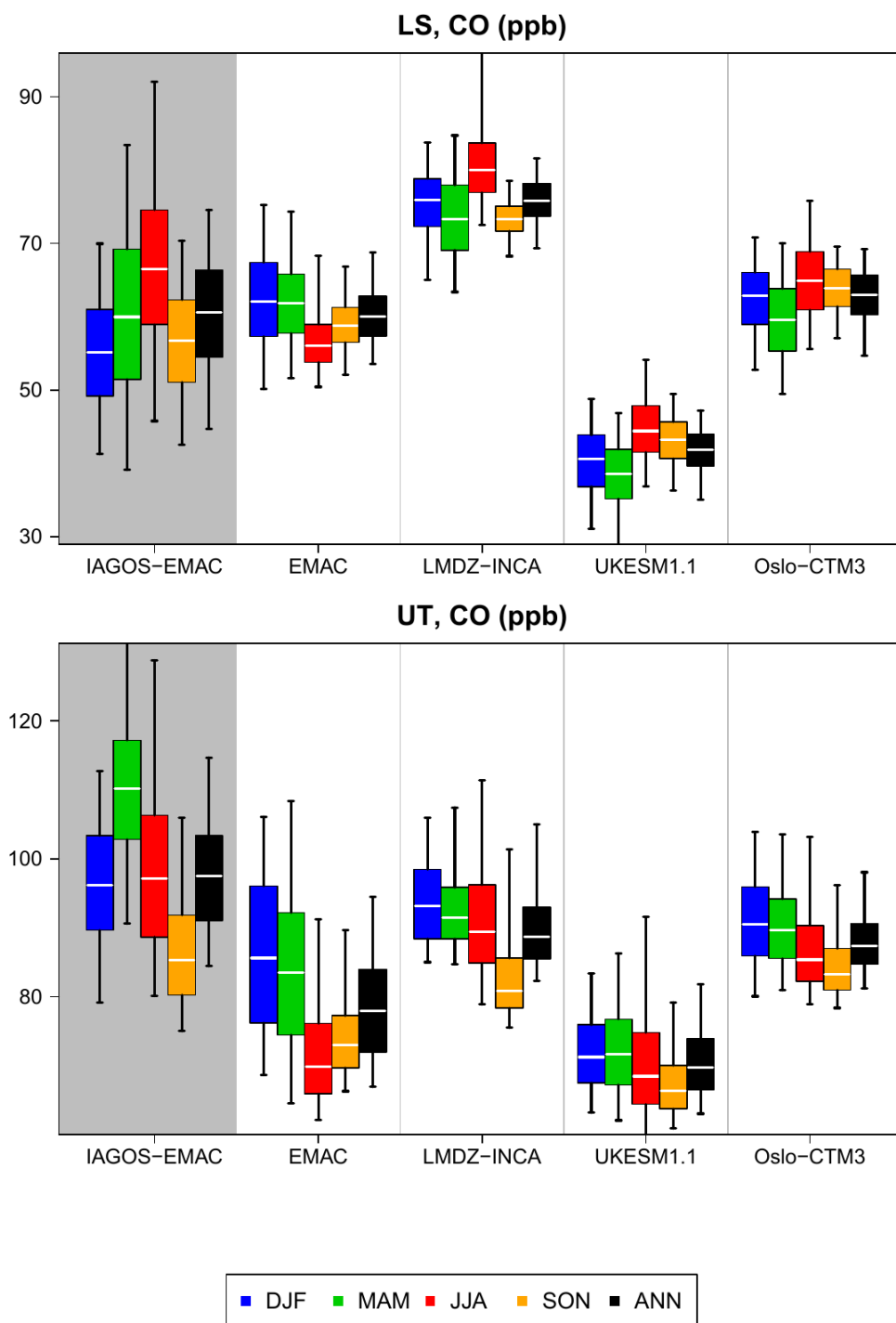
Figure 6. Same as 5 for CO.

NO_y and HNO_3 mixing ratios in UKESM1.1 are unlikely due to the different representation of the Brewer–Dobson circulation in the reanalyses, as the mean age of air in the northern LS is longer in ERA5 than in ERA-Interim (Ploeger et al., 2021; Li et al., 2022), which would tend to convert further N_2O into HNO_3 in UKESM1.1. In the end, considering both ozone and NO_y in the LS, the similarities between observations and models, notably during spring, are encouraging regarding the stratospheric chemistry and diabatic transport for all the models.

As shown in Figs. B1–B2 and Fig. B4, NO_y partitioning changes substantially between the models. In the UT, a higher proportion of NO_y is represented by HNO_3 with OsloCTM3. As it is affected by wet scavenging, it can explain the lower NO_y mixing ratios with this model, combined with very low PAN quantities. On the contrary, the higher levels of NO_y in the UT with the EMAC model can be linked to the high proportion of PAN which is not soluble and has a several-month chemical lifetime (e.g. Fadnavis et al., 2015). The higher amounts of PAN themselves might be linked to the EMAC colder temperatures ($\sim -4K$), as it increases its lifetime against thermolysis. In the UT, the higher (lower) NO_x mixing ratios from the EMAC (LMDZ-INCA) model can also explain the higher (lower) ozone mixing ratios. The intermodel variability regarding PAN in the UT might also have consequences on the air quality evaluation in the subsidence regions, as PAN lifetime against thermolysis decreases drastically during the descending motion, from months down to minutes when the temperature reaches 20 °C. Regarding this variability, surface ozone production due to the PAN subsidence is thus likely to vary substantially across the models (at least in the remote areas with a NO_x-limited regime), with a maximum for EMAC and a minimum for OsloCTM3. In the LS, PAN intermodel variability is the most noticeable of all NO_y species, with a factor reaching 12 between the median mixing ratio from EMAC and OsloCTM3, and an important difference in every couple of models. The low (high) amounts with OsloCTM3 (EMAC) are, at least partially, related to the low (high) amounts in the UT as well.

The lower-stratospheric features described above are generally visible in the UTLS as well, as illustrated in Fig. 9, for the species with a strong positive vertical gradient. Notably, the springtime maximum is well represented by every model for ozone and almost all the models for NO_y, including MOZART3, which confirms that all the models catch the seasonality of the Brewer–Dobson circulation. The water vapour and temperature maximum in summer are also visible in the simulations. For the five models, NO_y seasonal cycle is characterized by a springtime maximum in HNO_3 due to the Brewer–Dobson circulation, and by a summertime maximum in both NO_x and PAN due to convection, photochemistry, and lightning emissions.

In the previous figures (Figs. 7–9), we can notice that when the annual means are noticeably biased, the sign of this bias is generally representative of all the seasons, though its magnitude is not. With this perspective, the annual means shown below still provide relevant information. Figure 10 synthesizes some model skills in terms of annual averages in the extra-tropics, and the intermodel ranges are indicated more precisely in Table 4. Ozone mixing ratio is generally more difficult to model in the
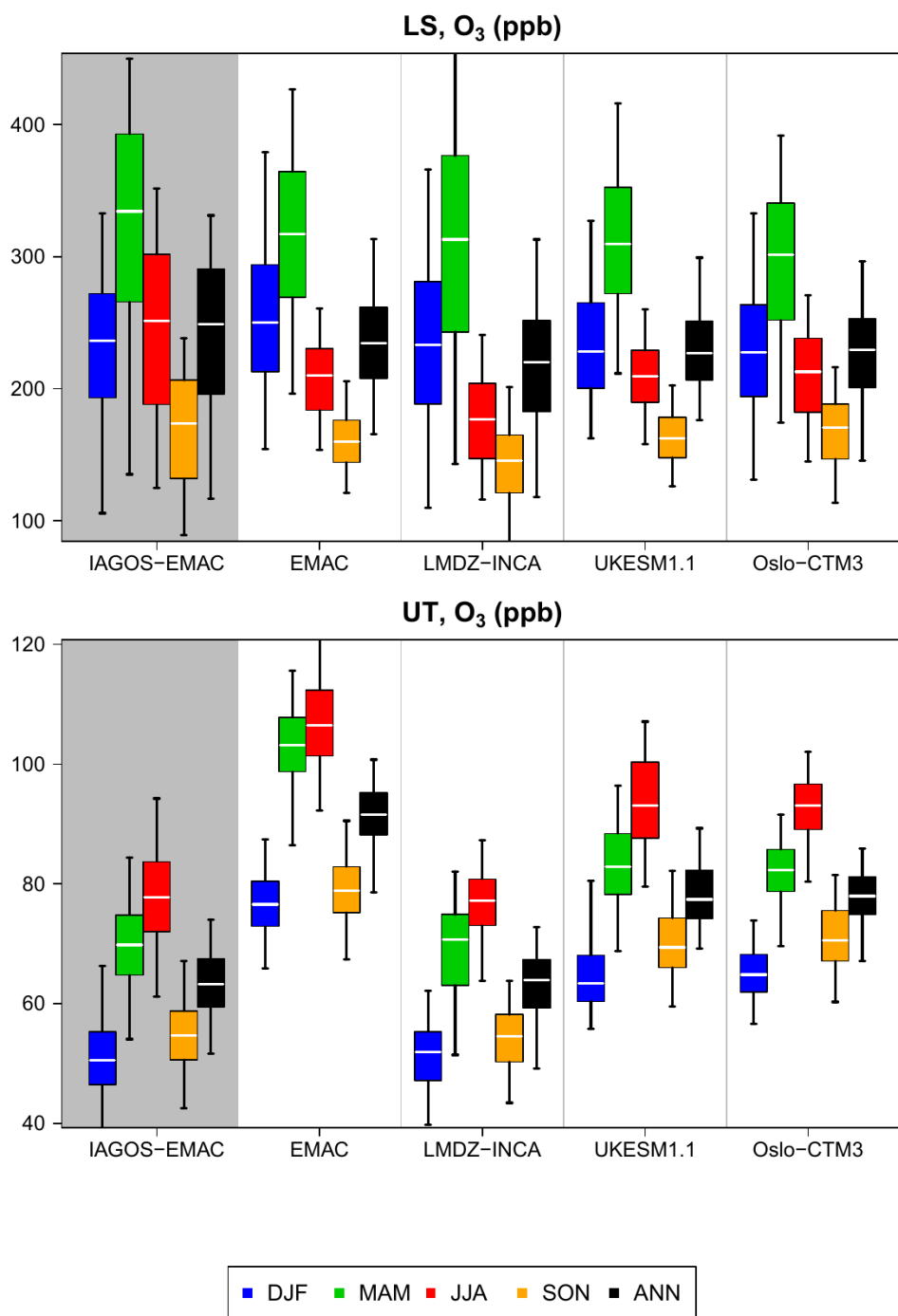
Figure 7. Same as 5 for ozone.
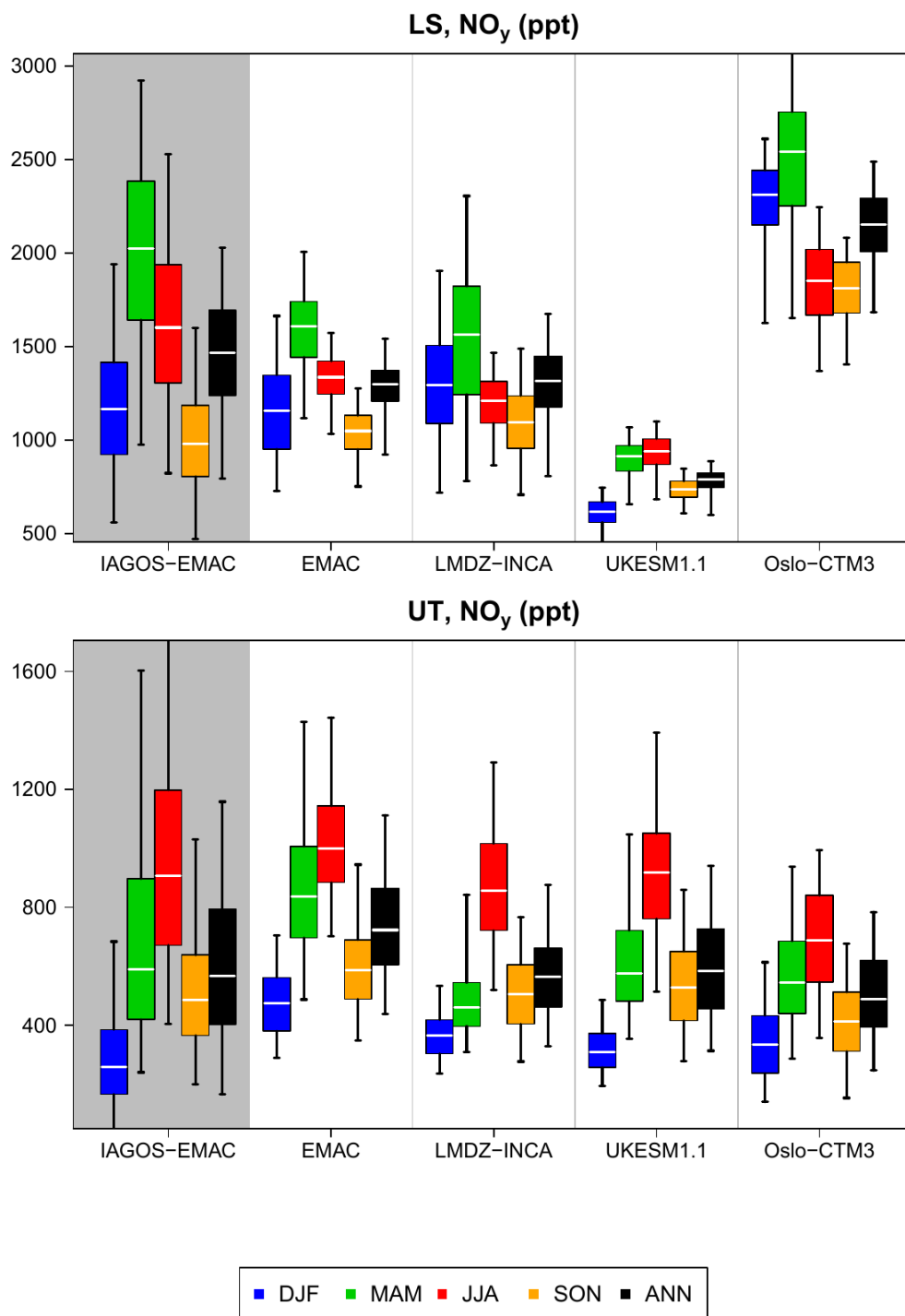
Figure 8. Same as 5 for NO_y.
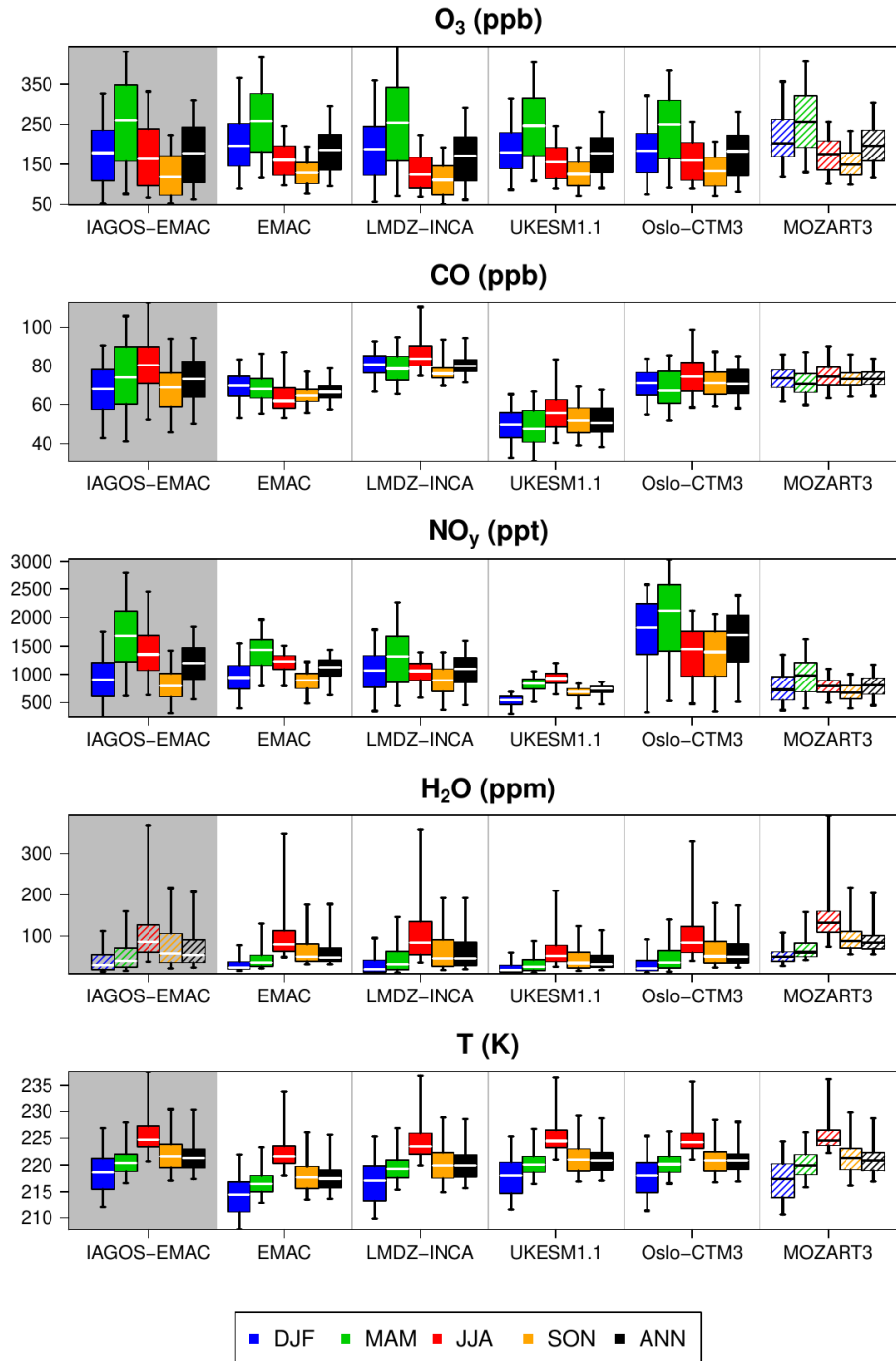
Figure 9. Boxplots synthesizing the mean geographical distribution in extratropical variables (from top to bottom: ozone, CO, NO_y, water vapour and temperature) in the non-separated UTLS, for the IAGOS–EMAC product and for the five model products (from left to right). Due to its uncertainty, observed H_2O in the LS shown here cannot be used for accurate quantification, hence the dashed IAGOS–EMAC boxplots. Boxplots are also dashed for MOZART3 to remind ones that the corresponding climatologies cannot be compared directly to the IAGOS–EMAC product, as it is based on a different meteorology.

UT than in the LS, in terms of geographical distribution ($r_{UT}(O_3)$ = 0.45–0.74, compared to $r_{LS}(O_3)$ = 0.75–90) as in terms of mean biases, the latter being essentially positive for most models in the UT (MNMB = 0.005–0.36, FGE $\sim$ MNMB for three models), and weak in the LS (MNMB = -0.08–0.006, with a maximum FGE at 0.16, particularly low). On the contrary, CO correlation coefficient is higher in the UT ($r_{UT}(CO)$ = 0.63–0.78) than in the LS ($r_{LS}(CO)$ = 0.11–0.70), probably reflecting

445 the difficulty in mapping the effects of the cross-tropopause exchanges. In the UT, ozone and CO biases tend to be respectively positive and negative. This antagonism can be linked with overestimated cross-tropopause exchanges and/or an overestimated photochemical activity, thus with more ozone production and more CO destruction. In the UT as well, both surface tracers (CO and H_2O) show good correlations ($r_{UT}(H_2O) \sim 0.95$ and, for most models, $r_{UT}(CO) \sim 0.8$). The skill difference between the two species can be explained either by uncertainties in CO emissions in each region, or an underestimation of the detrainment

450 altitude from pyroconvection consistently with the negative biases in CO in the UT. Interestingly, the bias magnitudes for both species are higher for EMAC and UKESM1.1. Concerning EMAC, the systematically negative temperature biases (-3.7 K on average) could be another factor controlling lower water vapour amounts in the UT via saturation, but it would not be consistent with the combination of lower temperatures (-4.0 K on average) with more water vapour in the LS, compared to the other models. A comparable cold bias with EMAC has been diagnosed in Righi et al. (2015) at 200 hPa with a similar

455 simulation set-up, who also identified a wet bias compared to the observations from the Halogen Occultation Experiment (HALOE: Grooß and Russell III, 2005), at 200 hPa in the extra-tropics. They concluded that an overestimation of lower-stratospheric water vapour would cause excessive radiative cooling and thus a cold bias, a relation that had already been shown in previous studies. This moisture overestimation in the LS is confirmed in Fig. 5, showing higher H_2O amounts in EMAC compared to the observations, given that the latter are probably overestimated. Concerning UKESM1.1, it is worth reminding

460 that the low mixing ratios in H_2O and CO in both layers (see Figs. 5–6) suggest an underestimation in the upward fluxes from the surface up to the UT. Last, NO_y shows the largest variability in the MNMB in the UT, and the lowest correlation coefficient among the four chemical species. It can be due to the important intermodel variability in the spatial distribution of lightning emissions (e.g. Hakim et al., 2019) or to the washout of HNO_3, which depends on the cloudiness representation and NO_y partitioning.

465   Figures A2–A5 provide further information on the annual geographical distribution mentioned above for each species, layer, and model, in the northern extra-tropics. The particularly high correlation for water vapour (r = 0.95) shown in Fig. A2 is characterized by a well-reproduced meridional structure, notably with the strong variability in the lowest latitudes (orange and red dots) due to dry subsiding and moist convective regions. It is notably characterized by a linear regression slope close to 1 for EMAC, LMDZ-INCA, and OsloCTM3. All of these features are representative of all the seasons, with the highest
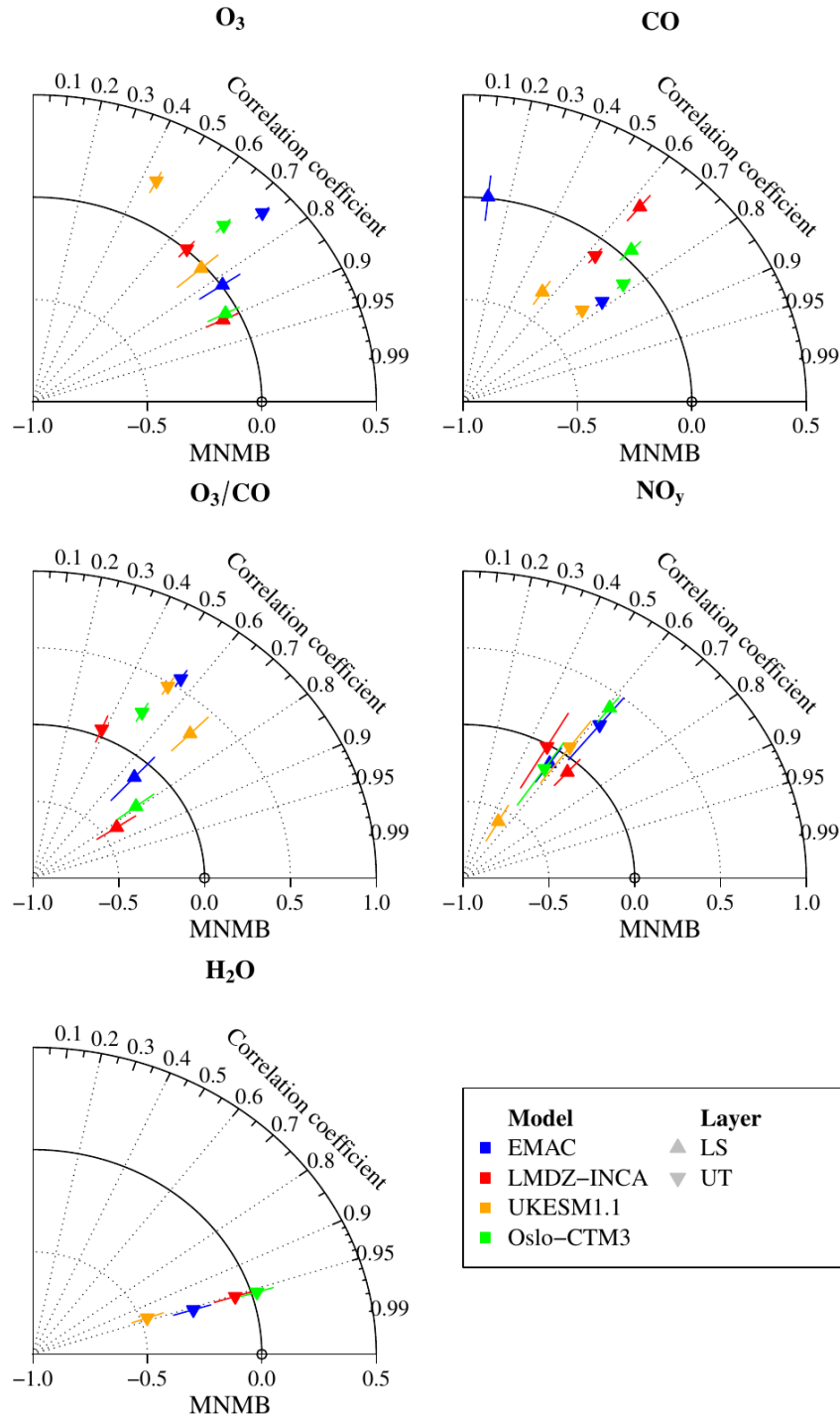
Figure 10. Modified Taylor diagrams synthesizing the assessment of the yearly climatologies beyond $25°$ N derived from the five model output against their respective IAGOS–DM product, for O_3, CO, O_3/CO ratio, NO_y, and upper-tropospheric H_2O. Each model is represented by a color and each layer by a point shape. The radial axis corresponds to the modified normalized mean bias (MNMB) for the chemical compounds, and the orthoradial axis refers to the r correlation coefficient. The error bars are the quartiles 1 and 3 of the normalized biases shown in Figs. 1–4.

Table 4. Annual metrics synthesizing the assessment of O_3, CO, O_3/CO ratio, NO_y, H_2O, and temperature climatologies from the model simulations against their respective IAGOS–DM product in the UT and the LS, as shown in Fig. 10 and in Appendix (Figs. A2–A5). From left to right: the Pearson correlation coefficient (r), the modified normalized mean bias (MNMB), the fractional gross error (FGE) and the sample size (N_{cells}). For temperature, the absolute bias and its associated error are equivalent to the MNMB and the FGE without the normalizing factors. Each metric is represented with an intermodel range.

Species	Layer	r	MNMB	FGE	N_{cells}
O_3	LS	0.75–0.90	[-0.08, 0.006]	0.11–0.16	4,368–4,604
	UT	0.45–0.74	[0.005, 0.36]	0.07–0.36	3,144–3,577
CO	LS	0.11–0.70	[-0.36, 0.23]	0.09–0.36	4,458–4,702
	UT	0.63–0.78	[-0.31, -0.08]	0.09–0.31	3,145–3,636
O_3/CO	LS	0.69–0.83	[-0.41, 0.32]	0.26–0.42	4,135–4,470
	UT	0.39–0.54	[0.04, 0.56]	0.12–0.56	2,778–3,260
NO_y	LS	0.49–0.66	[-0.58, 0.40]	0.17–0.58	3,077–3,274
	UT	0.50–0.62	[-0.14, 0.28]	0.32–0.38	1,831–2,187
H_2O	UT	0.94–0.96	[-0.47, 0.025]	0.11–0.47	3,289–3,642
			Abs. bias (K)	Abs. error (K)	
T	LS	0.79–0.86	[-4.0,-0.4]	0.7–4.0	4,952–5,132
	UT	0.98–0.99	[-3.7,-0.5]	0.8–3.7	3,646–4,002

470   correlation and linear regression slope during summer, when the tropospheric humidity reaches its maximum. These features are encouraging concerning the modelled impact of meteorological systems on the extratropical UT in terms of geographical variability, despite the negative mean biases present in most models.

In the lowermost stratosphere, Fig. A3 shows that ozone geographical variability is relatively well reproduced by the models with a distinct northward gradient. This gradient tends to be underestimated because of a positive bias in the lowest values (in

475   the subtropics) for most models, and a negative bias in the highest values in the subpolar regions. The northward gradient is also visible for NO_y (Fig. A5) with an underestimated regression slope as well, but with a substantially lower correlation coefficient. Contrary to ozone, this is characterized by poor correlations inside each zonal band. It suggests that NO_y correlation in the LS is mostly due to the northward gradient and that the smaller scales are hardly captured by the models for this variable.

Concerning the upper troposphere in Fig. A3, the observed ozone climatology does not show any latitude gradient, with

480   yearly means ranging between ∼50 and 80 ppb independently of the latitude bin, except for some subtropical locations that are poorer in ozone and can reach ∼35 ppb. The EMAC model reproduces this feature relatively well, though with a systematic overestimation. The other models do not differentiate the northernmost two bins (45–55° N and 55–65° N), but they tend to make a distinction between 25–35° N, 35–45° N, and 45–65° N. LMDZ–INCA and OsloCTM3 tend to simulate a northward gradient. As it is a characteristic of the LS, it would be consistent with an overestimated stratosphere–troposphere transport.

485   Concerning UKESM1.1, a significant part of subtropical ozone values are higher than in all the high latitudes. It might be a consequence of the lower-stratospheric biases into the UT through cross-tropopause exchanges, as in the LS, subtropical ozone

is particularly overestimated and high-latitude ozone is less abundant than in the other models. For NO_y in the UT shown in Fig. A5, we also notice that the models simulate more NO_y in the high latitudes and less in the subtropics as in the LS, which is not consistent with the observations and suggests overestimated cross-tropopause exchanges as well.

It has to be noticed that these diagrams average values through the whole sampled extra-tropics in the northern hemisphere. An assessment based on regional-specific characteristics could provide more information on specific processes, such as tropopause folds during the Middle East summer or isentropic transport from the tropical troposphere into the extratropical lowermost stratosphere (Cohen et al., 2018). Another limitation of this approach is that the tropopause altitude decreases with the latitude whereas the cruise altitude does not depend on latitude. Consequently, the subtropics are more sampled in the UT than in the LS, and reversely, the high latitudes are more sampled in the LS than the UT. The scores shown for the different layers are thus not completely representative of the same geographical area.

The comparison with previous model assessment studies provides complementary information. First, most of the CCMVal-2 free-running models assessed in Hegglin et al. (2010) underestimated the vertical stability in the northern mid-latitudes (40–60° N), especially for the semi-Lagrangian models and the models with the lowest vertical resolution. As a consequence, they generally underestimated ozone and HNO_3, and overestimated water vapour at 200 hPa, which is included in the lowermost stratosphere at these latitudes. Though all the CCMVal-2 models did not have a specific tropospheric chemical scheme, and though only the EMAC model is involved in both studies, our results tend to confirm the ability of the models to reproduce the seasonality of the Brewer–Dobson circulation through ozone and HNO_3 tracers, and the overestimation of cross-tropopause mixing, notably the effect of the tropospheric influence on lower-stratospheric ozone that maximizes during summer and fall. On this last point, the effect of the vertical resolution is visible on lower-stratospheric ozone with the less resolved model (LMDZ-INCA) showing the lowest vertical gradient in ozone. Still, it does not seem to be the most controlling factor for water vapour, as the EMAC model is one of the most resolved models but has the weakest water vapour vertical gradient, unless the nudging makes this inter-model hierarchy less evident. Concerning the impact from the Brewer–Dobson circulation on the LS, a better understanding of the simulations' biases could be brought by assessing the dynamical behaviour exclusively, hence adding other variables like stratospheric age of air would be relevant for a more complete model evaluation, or the zonal momentum (e.g. Diallo et al., 2021).

In addition to the model assessment, the model intercomparison of background CO, ozone and NO_x in the UT and the LS (Figs. 6, 7, and B1 respectively) can provide further understanding of each model's ozone sensitivity to aircraft NO_x emissions, as the critical NO mixing ratio separating net production and net destruction of ozone depends on these three parameters (Grooß et al., 1998). It remains uncertain as it ignores the behaviour of lots of non-measured VOCs and methane, but it still provides

a comparison of several factors controlling the sensitivity of the net ozone production to NO_x emissions. In the UT, we can expect the most different ozone responses between the EMAC and LMDZ-INCA models, as EMAC shows higher NO_x and ozone values and lower CO values, contrary to LMDZ-INCA. In the LS, it can also be expected that the LMDZ-INCA model maximizes ozone response since NO_x (CO) is relatively low (high), and this difference can be enhanced during summer and fall with relatively lower ozone values. The two models showing the highest NO_x values (EMAC and especially OsloCTM3, with more than twice the median compared to LMDZ-INCA and UKESM1.1) can be expected to have a lower ozone response.

3.3 Tropics

The zonal cross sections shown in Figs. 11 and 12 compare the reference runs with the observations in three tropical regions: South America–Atlantic (called South America hereafter), Africa, and South Asia. First, we present a brief summary of some observed patterns that have been investigated in Cohen et al. (2023), notably based on Livesey et al. (2013), Lannuque et al. (2021), and Gottschaldt et al. (2018) for the three regions, respectively from west to east. In a second step, we present an overview of model skill. The mean pressure is represented as well, in order to identify the changes in the observed variable that can be associated with changes in the sampling mean altitude. This case occurs at the edge of the sampled regions, notably for NO_y during December–February above South America, and during June–October above Africa. The IAGOS–OsloCTM3 profiles are represented as well, as their sampling period is shorter than the other three models (2001–2017 instead of 1995–2017), which causes important differences only in the IAGOS–OsloCTM3 transects in ozone during July–August in South America, and in water vapour during June–October above Africa.

Most of the observed features have been investigated in Cohen et al. (2023), as the impacts of wet and dry seasons, linked to the shifts in the inter-tropical convergence zone (ITCZ). In the two western regions (South America and Africa) where the zonal cross sections cover most of the tropical latitudes, the wet season is characterized by a collocated maximum in water vapour and a minimum in ozone, both linked with intense convection of humid surface air. The latter is rather rich in fresh pollutants and gets enriched in NO_x emitted by lightning during convective uplift. In the upper branch of both Hadley cells, ozone is produced by photochemistry during its poleward transport.

Above Africa, the seasons with the northernmost and the southernmost ITCZ (resp. June–October and December–March) are particularly visible in the IAGOS observations. During the meridional transport in the upper branch of the strongest Hadley cell, CO accumulates in the areas where zonal wind shear is greater (Sauvage et al., 2007; Lannuque et al., 2021) as for NO_y, reaching a maximum at approximately $10°$ away from the ITCZ. Using a method based on the FLEXPART Lagrangian dispersion model (SOFT-IO: Sauvage et al., 2017), Lannuque et al. (2021) found that these CO peaks originated from intense
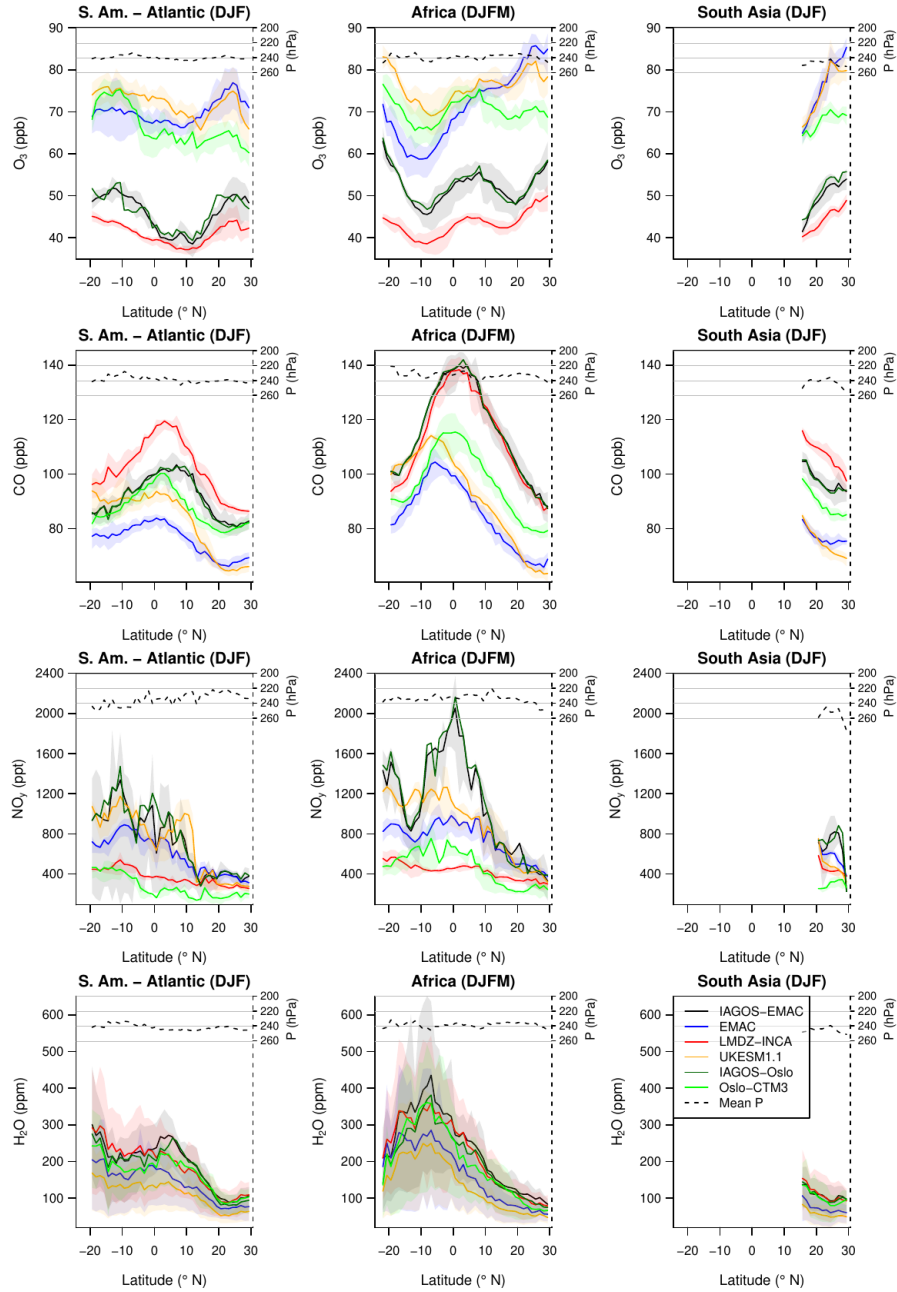
Figure 11. Zonal cross sections between 25° S and 30° N from December until February or March. Each row represents a measured variable, and each column represents the corresponding region: from left to right, South America–Atlantic Ocean, Africa, and South Asia. The uncertainties shown here correspond to the spatial variability, defined as the interval between the quartiles 1 and 3. The solid black, and dark-green lines correspond respectively to IAGOS–EMAC, and IAGOS–Oslo. For further visibility, the observational variability is shown only for the IAGOS–EMAC profiles. The blue, red, orange, and green lines correspond respectively to the reference simulation from EMAC, LMDZ-INCA, UKESM1.1, and OsloCTM3. The dashed line at the top of each graphic shows the mean pressure derived from IAGOS–EMAC. Its values are reported on the right axis.
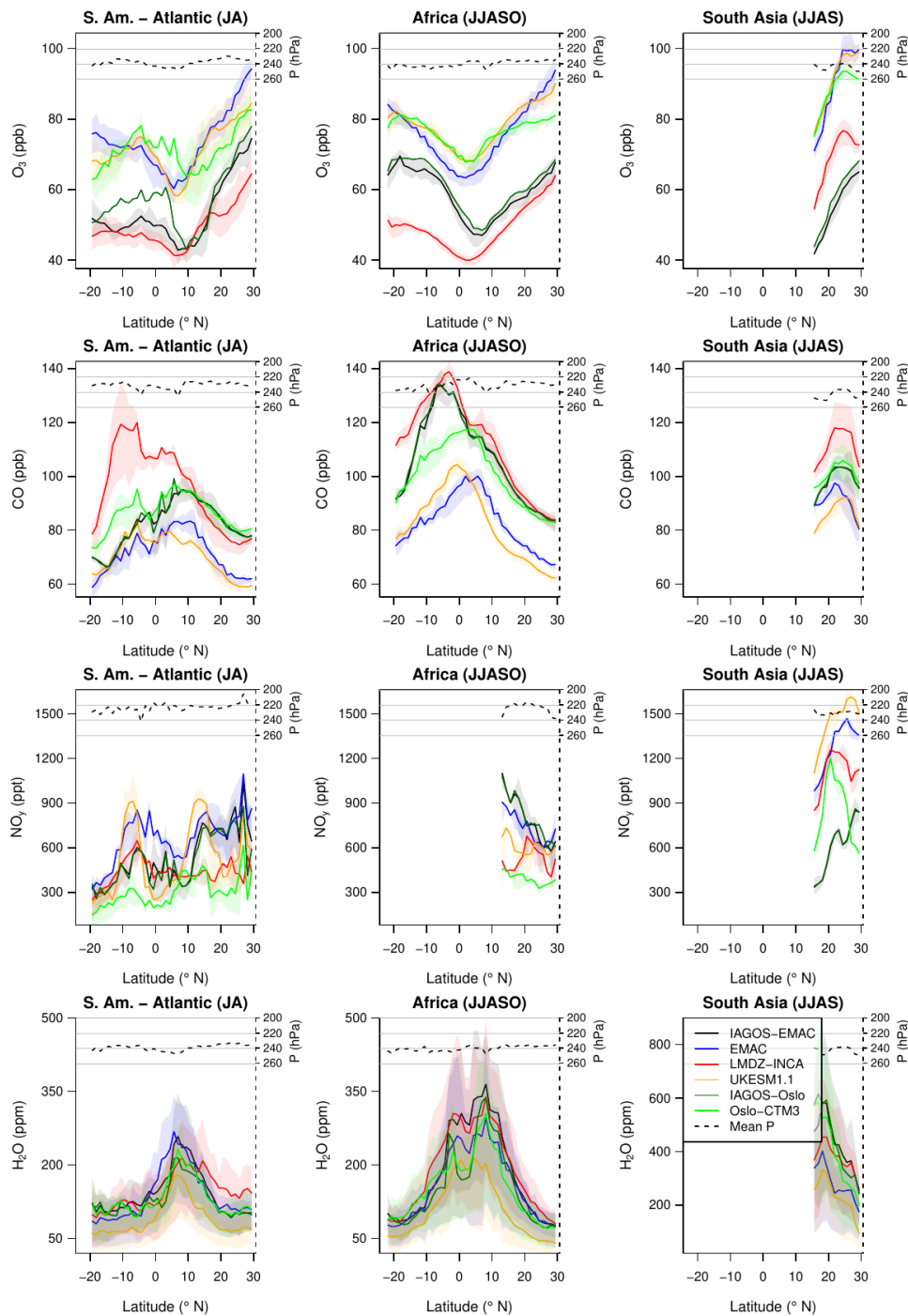
Figure 12. Same as Fig. 11 for July–August, June–October and June–September, from left to right. Please note the different scale for water vapour in the right column.

biomass burning in the dry season. A sensitivity test regarding biomass burning with the LMDZ-INCA model (Cohen et al., 2023) found similar conclusions. In the monsoon season (June–October), both studies agree on a major biomass-burning contribution to the southward shift of the peak of CO. Last, the Asian Summer Monsoon (right panels) is characterized by the warmest and most humid air masses, as expected from the strongest convective system. During this season, the subtropical jet stream and its subsequent stratospheric intrusions are confined on the northern side of the Himalayas (Cristofanelli et al., 2010), thus ensuring a weak stratospheric influence in this season (Gottschaldt et al., 2018).

The analysis of the modelled local and seasonal features provides interesting information about the representation of the convective systems and their outflows. All the models capture the location of the peaks in water vapour in the African upper troposphere whatever the season, the maximized water vapour amounts (as well as temperature, not shown) above the Asian summer monsoon (Fig. 12, right column), and the strongest CO peaks above Africa. More precisely above Africa, the December–March (June–October) season, the models capture relatively well the southward (northward) shift of the ITCZ, characterized by an ozone minimum collocated with the water vapour maximum. This agreement among the models and with the observations highlights a realistic representation of the strongest convective systems. It is probably improved by the nudging, by the use of a common surface temperature field based on observations, and by a common (or similar) inventory for biomass burning emissions.

Regarding the effects of convection, the variability between the models can be found in the water vapour and CO peaks' intensity, and CO peak location. In most cases, water vapour shows a small bias with LMDZ-INCA and OsloCTM3, and a dry bias with EMAC and UKESM1.1. The EMAC dry bias is possibly explained by a cold bias in the UT ($\sim$ -5 K, not shown) lowering the saturation vapour pressure and/or the detrainment altitudes. The other models show particularly well reproduced temperatures, and all the modelled temperature profiles are well correlated with the observations (not shown).

The location and the width of CO maximum depend on the model, notably above Africa: it is rather collocated with the ITCZ for the EMAC and UKESM1.1 models, and shifted 5–10° equatorward for the other models, in agreement with the observations. Concerning June–October, with the same observation data set, Lannuque et al. (2021) show a peak in anthropogenic contribution to upper-tropospheric CO collocated with the ITCZ (as with EMAC and, to a lesser extent, UKESM1.1 and OsloCTM3) and a peak in biomass burning contribution shifted 10° southward, as with the LMDZ-INCA model. OsloCTM3 seems to show a compromise between the two categories, with a flatter and wider maximum including both the ITCZ position and the observed CO peak. A sensitivity test (Cohen et al., 2023) using the LMDZ-INCA model that reproduces well CO peak in CO during December–March and June–October (with its location as well as its magnitude near 140 ppb) concluded on the biomass burning being the main factor of the peak intensity with a contribution reaching 30 and 45 ppb during DJFM and

JJASO respectively, but also in the southward shift of CO peak during June–October. The negative CO bias combined with the absence of the southward shift in the EMAC and UKESM1.1 simulations is thus likely to reflect an underestimation of the
575   impact from biomass burning in the tropical UT. As the dry bias in the water vapour peaks in these two models suggests a less intense convection, it implies a weaker Hadley circulation. Consequently, the lower-tropospheric entrainment into convective motions in the ITCZ has a reduced geographical extent and thus includes less air from the dry region. It could explain the lack of CO accumulation in the higher tropical latitudes with these two models. Inversely, the LMDZ-INCA model and, to a lesser extent OsloCTM3, show another peak in CO in July–August above South America at relatively similar latitudes as for the peak
580   in Africa, absent from the observation profiles. As it is mainly due to biomass burning for LMDZ-INCA (Cohen et al., 2023), and as LMDZ-INCA and OsloCTM3 show similar behaviours with CO, it suggests that both models overestimate the effects from the intercontinental connection with Africa during this season (in duration and/or in intensity) or from local biomass burning emissions.

Contrary to CO, the peaks in NO_y observed in December–February (December–March) show an important negative bias
585   in LMDZ-INCA and OsloCTM3, whereas the negative bias is lower with EMAC and UKESM1.1, especially above South America. Concerning the Asian summer monsoon, all the represented models overestimate ozone and NO_y mixing ratios, possibly reflecting an overestimation of the lightning flash rate, as it is known for LMDZ-INCA (Hauglustaine et al., 2004), an underestimation of HNO_3 uptake, and/or an overestimation of the entrained surface pollutants.

Most of the models tend to overestimate ozone, except the LMDZ-INCA model that rather shows negative biases. The
590   overestimation of ozone in the tropical UT from UKESM1.1 is consistent with a recent comparison based on ozone partial columns between UM–UKCA and the OMI–MLS satellite observations (Russo et al., 2023) during the 2005–2018 period and in the 450–170 hPa pressure range. The overestimation is representative of the whole tropospheric ozone column in the tropics, and the main factor in the UT is probably an overestimation of the lightning NO_x emissions. The LMDZ-INCA model shows particularly low NO_x levels with lowest (highest) mean values near 18 ppt (195 ppt) whereas the other models have NO_x
595   minimum (maximum) levels at 52–91 ppt (278–430 ppt). This first order statement can be sufficient to explain most of the LMDZ-INCA lower ozone values, but also most of the higher CO values with longer photochemical lifetimes for CO. Each of these two factors favour ozone production efficiency from lightning and aviation. A similar diagnostic applies to HNO_3. Though the stronger convection with LMDZ-INCA compared to EMAC theoretically produces more NO_x due to a higher lightning activity, it is thus possible that the LMDZ-INCA model overestimates NO_y removal by HNO_3 wet scavenging, both
600   with a more efficient conversion of NO_x into HNO_3, and with further precipitation due to a stronger convection.

4 Conclusion

The present study consists of a descriptive evaluation of 4 global chemistry-climate and chemistry-transport models (CCMs and CTMs) against the airborne IAGOS observations. The assessment is based on ozone, carbon monoxide (CO), water vapour (H_2O), reactive nitrogen (NO_y) and, to a lesser extent, temperature. It relies on airborne measurements during the cruise phases, i.e. in the extratropical upper troposphere–lower stratosphere (UTLS) and in the tropical upper troposphere.

A direct comparison between the model outputs and the IAGOS data set is made possible with the use of the Interpol-IAGOS software, which projects the IAGOS data onto the model grid with a daily resolution (Cohen et al., 2023). Meanwhile, a daily mask is applied to the model output with respect to the IAGOS sampling. For each grid cell, a weighted monthly average is then derived from both gridded observations and model output. For a given model, the subsequent IAGOS and model products are called IAGOS-DM-model and model-M respectively, the –DM and –M suffixes referring to the distribution onto the model grid, and to the IAGOS mask respectively. This way, each model product is directly comparable to the corresponding IAGOS-DM-model product. In the extra-tropics, the model potential vorticity (PV) is used to treat separately the upper troposphere (UT) and the lower stratosphere (LS). The assessment is based on the climatologies derived from these products, between 1995 until 2017 for most models. A synthesis of the model skill in reproducing the main observed atmospheric features is proposed in Table 5.

In the northern mid-latitudes, the results suggest that most models tend to overestimate the cross-tropopause mixing, which might be linked to a too-diffusive extratropical transition layer. The stratospheric tracers (O_3 and, to a lesser extent, NO_y) tend to be overestimated in the UT and underestimated in the LS. Concerning the tropospheric tracers (CO and H_2O), all the models systematically underestimate CO in the UT whereas only two of them systematically underestimate water vapour in this layer. It would be consistent with an underestimation of CO emissions from the CEDS inventory, and/or with an overestimation of CO photochemical loss. The geographical distributions are particularly well correlated with observations for ozone in the LS, and water vapour in the UT. Respectively, the former and the latter suggest a realistic distribution of the impacts from the stratospheric circulation, and of the synoptic-scale processes in the troposphere. The impact from biomass burning and lightning is harder to reproduce, notably because of the difficulty of parameterizing pyroconvection, lightning and the washout of soluble species.

The seasonality is generally consistent between models and observations, both in the UT, the LS, and the non-separated UTLS. Discrepancies are visible with CO in the UT, and ozone in the LS. The former is characterized by a modelled seasonal maximum gathering winter and spring contrary to the observed springtime maximum, and with an important negative bias in spring, which may suggest an underestimation of CO emissions in winter and spring, as it concerns all the models. Ozone

shows a stronger summertime decrease in the models than in the observations, probably caused by an overestimated influence from the troposphere, particularly during summer and fall. For each season, the models tend to underestimate the geographical variability in every measured species. One possible consequence is an excess of horizontal homogeneity in ozone response to aircraft NO_x emissions, but it is hard to conclude as the background NO_x cannot be compared with the observations in the same way as the other species.

Table 5. Synthesis of the model abilities to reproduce the main features from their respective IAGOS–DM products, regardless to their mean biases.

Layer	Species	Main features from IAGOS–DM	Reproduced by:				
			EMAC	LMDZ–INCA	UKESM1.1	OsloCTM3	MOZART3
LS*	O_3	Springtime maximum	Yes	Yes	Yes	Yes	Yes
		Northward gradient	Yes	Yes	Yes	Yes	-
	NO_y	Springtime maximum	Yes	Yes	No	Yes	Yes
		Northward gradient	Yes	Yes	Yes	Yes	-
	H_2O	Summertime maximum	Yes	Yes	Yes	Yes	Yes
	CO	Summertime maximum	No	Yes	Yes	Yes	-
		Southward gradient	No	Yes	Yes	Yes	-
UT	O_3	Summertime maximum	Yes	Yes	Yes	Yes	-
(extra-	NO_y	Summertime maximum	Yes	Yes	Yes	Yes	-
tropics)	H_2O	Summertime maximum	Yes	Yes	Yes	Yes	-
		Southward gradient	Yes	Yes	Yes	Yes	-
		High variability at low lat.	Yes	Yes	Yes	Yes	-
	CO	Springtime maximum	No	No	No	No	-
(tropics)	O_3	ITCZ minimum	Yes	Yes	Yes	Yes	-
	NO_y	Boreal winter: high south-north difference	Yes	No	Yes	Yes (Africa)	-
	H_2O	ITCZ maximum	Yes	Yes	Yes	Yes	-
		More H_2O in the ASM**	Yes	Yes	Yes	Yes	-
	CO	Africa: max. shifted from the ITCZ	No	Yes	No	Yes	-

Table 5. *Or UTLS for MOZART3, if the feature is also visible in the UTLS with IAGOS–DM.
**ASM: Asian Summer Monsoon.

The intermodel variability is particularly noticeable with NO_y individual species, in the UT as in the LS. The median NO_x level varies by a factor up to 3 in the UT, and up to 7 in the LS. It reflects both different chemical and physical behaviours, as NO_x conversion into HNO_3 or PAN, and HNO_3 wet scavenging that removes gaseous NO_y from this atmospheric region, or also the aerosol uptake of HNO_3. It has implications on the model sensitivity to NO_x injection in the UTLS from subsonic aviation as it changes NO_x regime, and on the evaluation of air quality from the models in the subsidence regions as PAN varies substantially across the models and is rapidly converted into NO_x at typical surface temperatures.

The addition of NO_x measurements from CARIBIC will allow an evaluation of NO_x biases, at least in the most sampled regions. In the longer term, the IAGOS-CORE measurements of NO_x will open the opportunity of calculating NO_x climatologies as well, with a higher level of sampling. The particulate matter measurements will also provide another variable for the assessment, and further explanation for the chemical processes related to HNO_3. Concerning the models, a more accurate interpretation of the inter-model variability could be provided with additional variables such as horizontal wind velocities, potential temperature, and inert tropospheric and stratospheric tracers, in order to isolate further the role of dynamics or chemistry in the modelled mixing ratios. In the extra-tropics, the choice of more accurate dynamical coordinates as the equivalent latitudes (involving both potential temperature and PV) or the jet-related tropopause (Millán et al., 2024) will probably improve the model assessment, as well as vertical profiles with tropopause-relative coordinates. Last, the models' ability to simulate long-term trends has to be evaluated as well, as a complementary part of the current analysis.

Appendix A: Geographical distributions
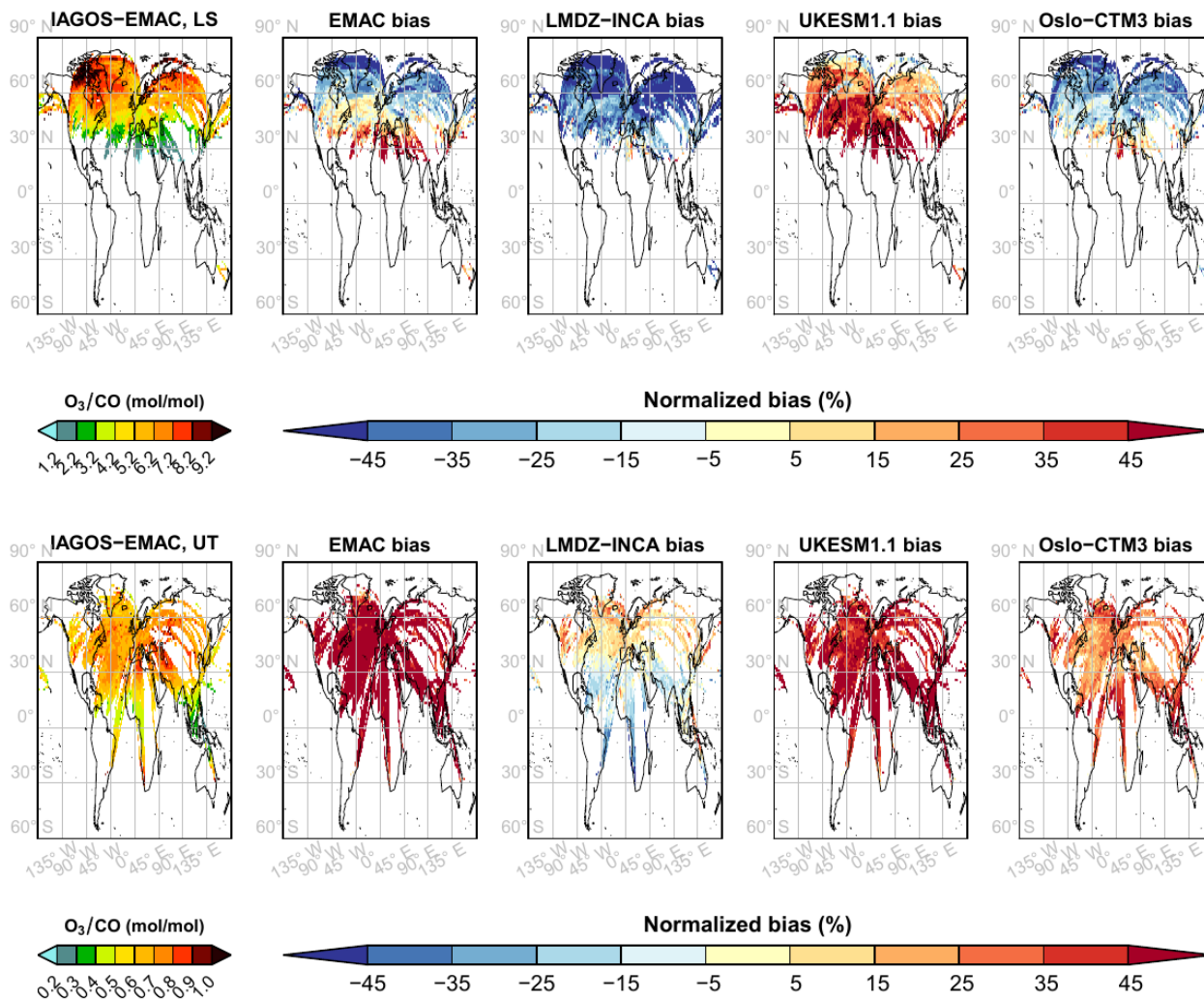
Figure A1. Same as Fig. 1 for the O_3/CO ratio, over the period 2002–2017.
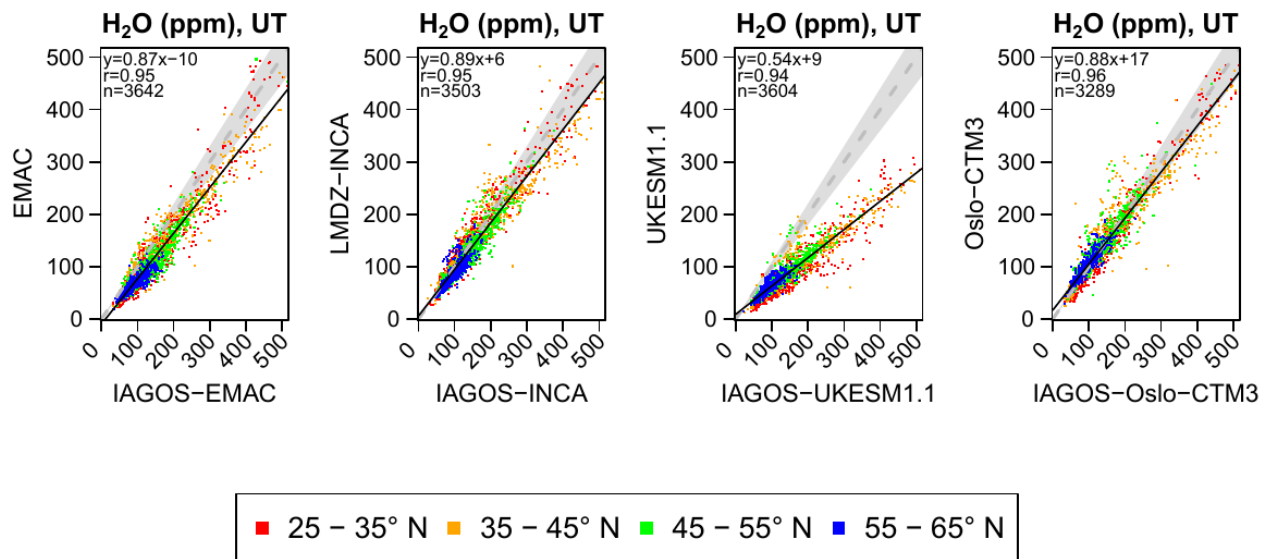
Figure A2. Scatterplots comparing the geographical distributions in water vapour in the extratropical UT between the models' output (Y axis) and their respective IAGOS products (X-axis), in terms of annual means. The colors display a latitude band, from subtropical (red) to subpolar latitudes (blue).
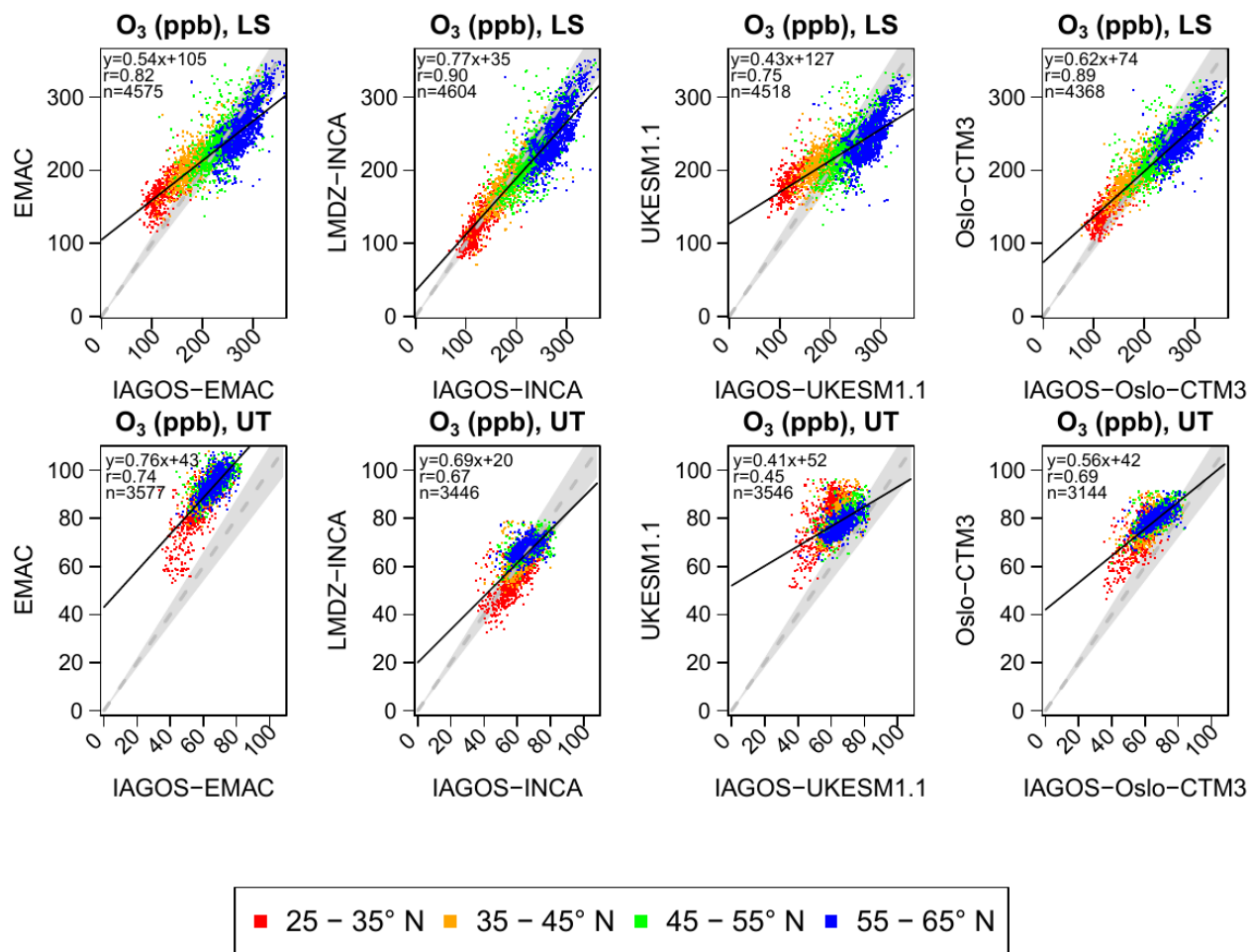
Figure A3. Same as Fig. A2 with ozone, in the LS (top panels) and the UT (bottom panels).
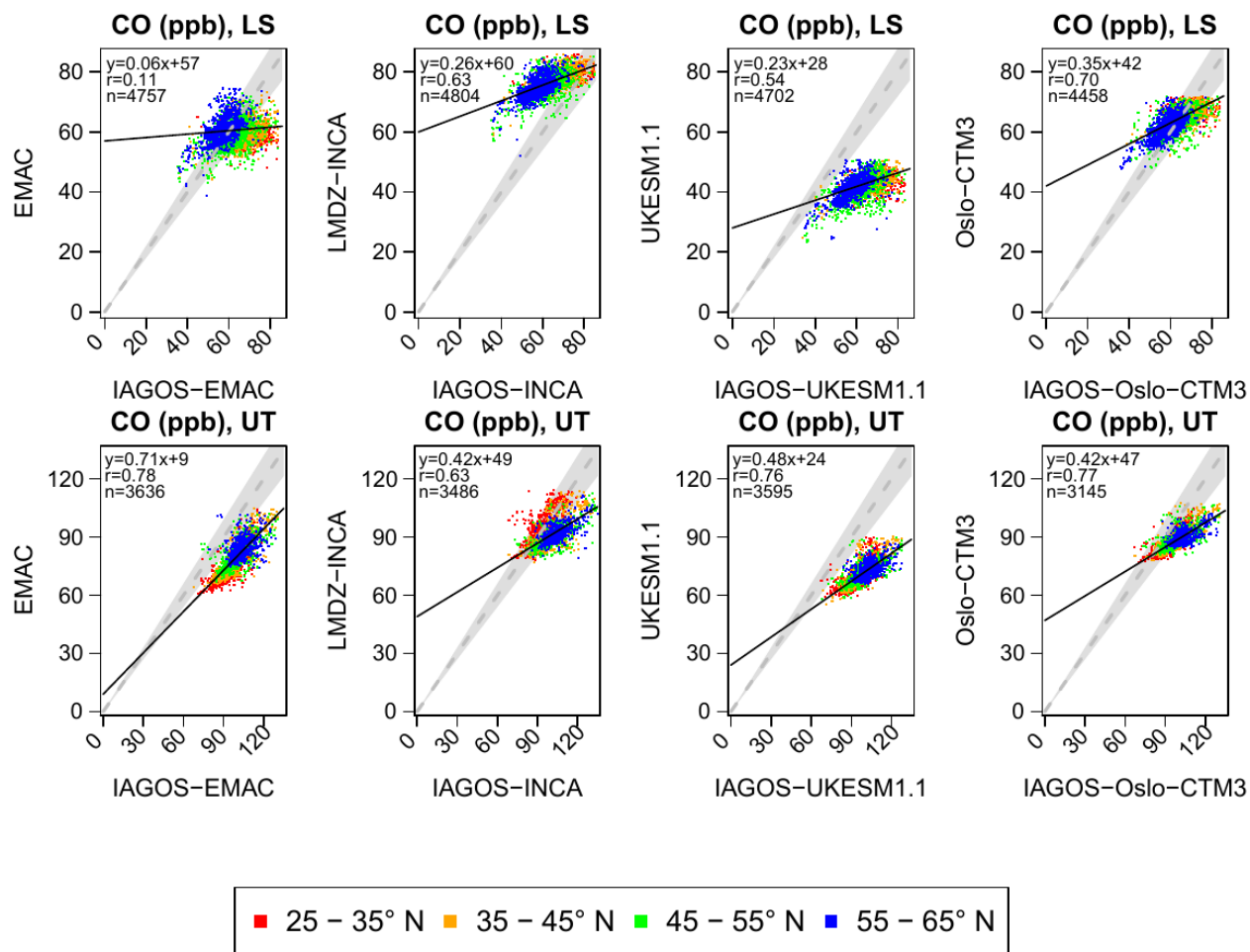
Figure A4. Same as Fig. A3 for CO.
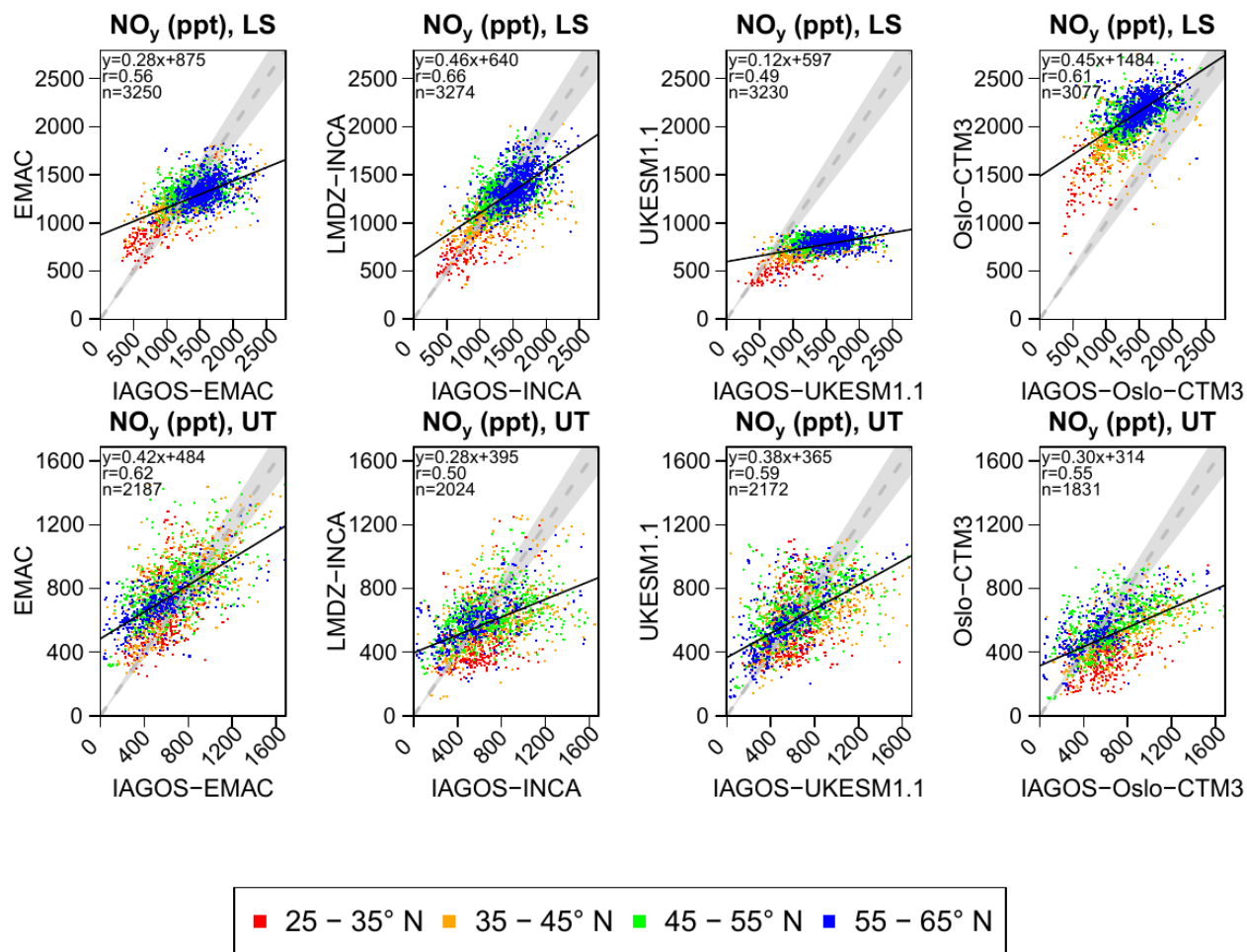
Figure A5. Same as Fig. A3 for NO_y.

Appendix B: Individual NO_y species
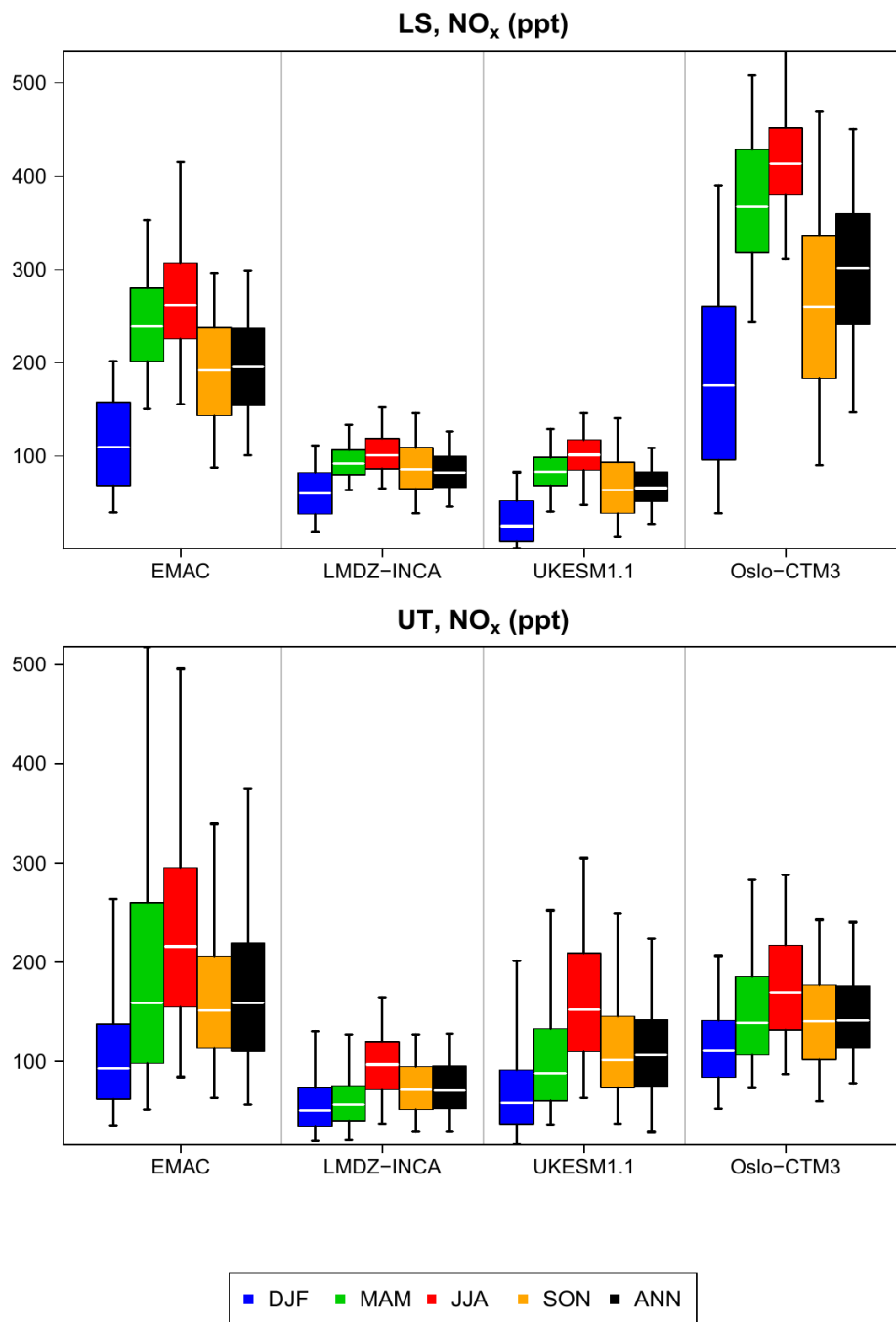
Figure B1. Boxplots synthesizing the contribution of NO_x to NO_y levels shown in Fig. 8 in the LS (top) and the UT (bottom), for the four model products.
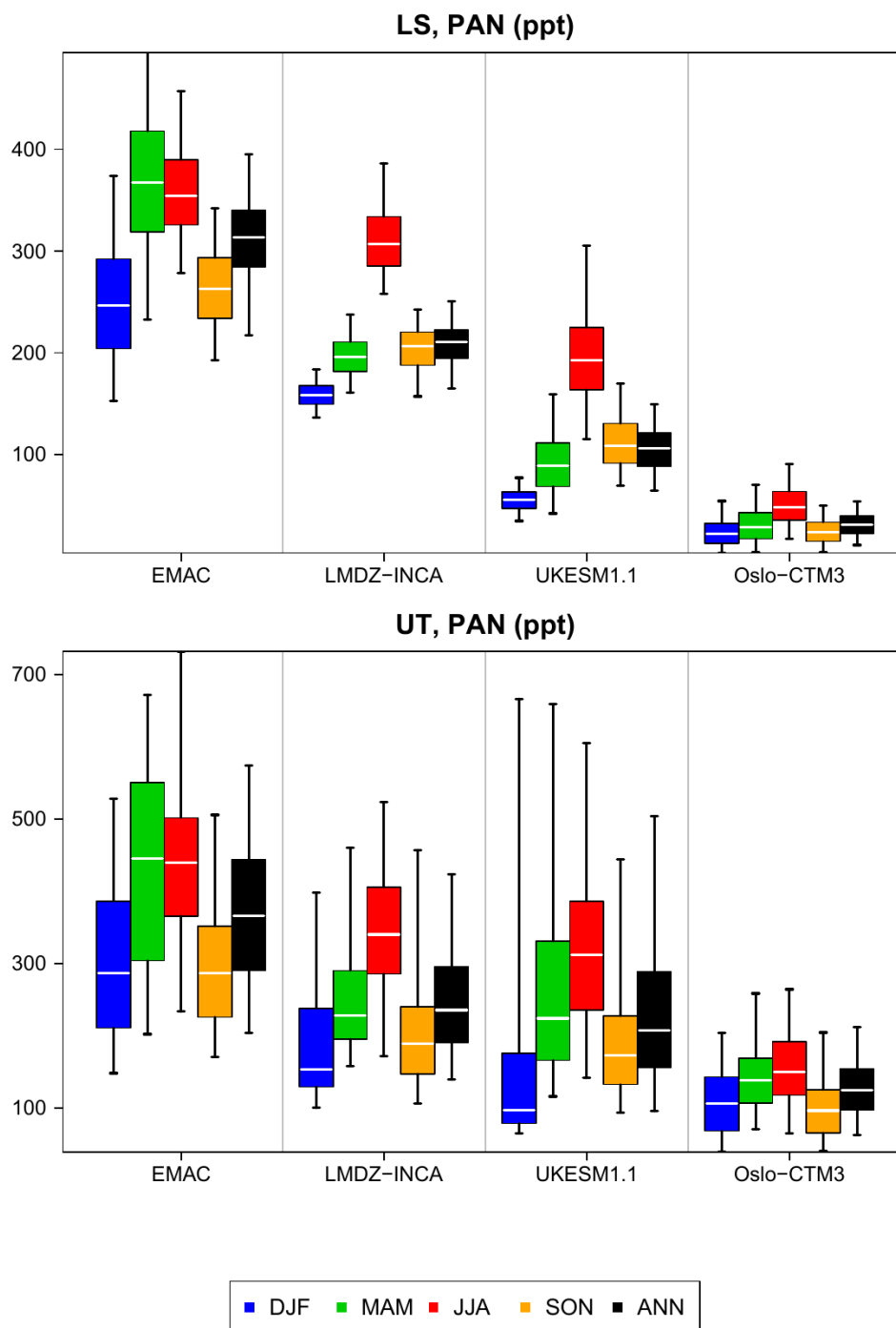
Figure B2. Same as Fig. B1 for peroxyacetyl nitrate (PAN).
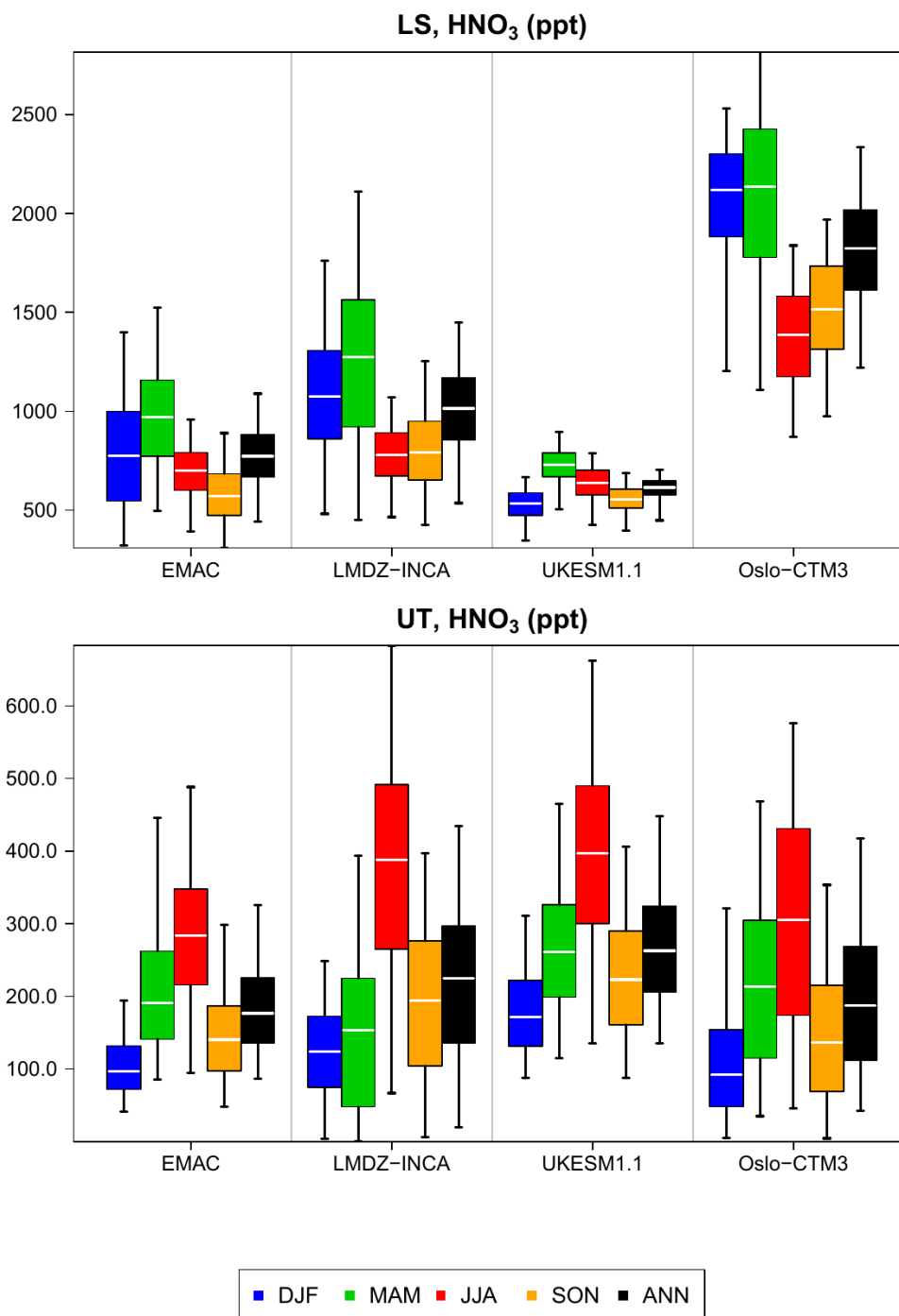
Figure B3. Same as Fig. B1 for nitric acid (HNO_3).
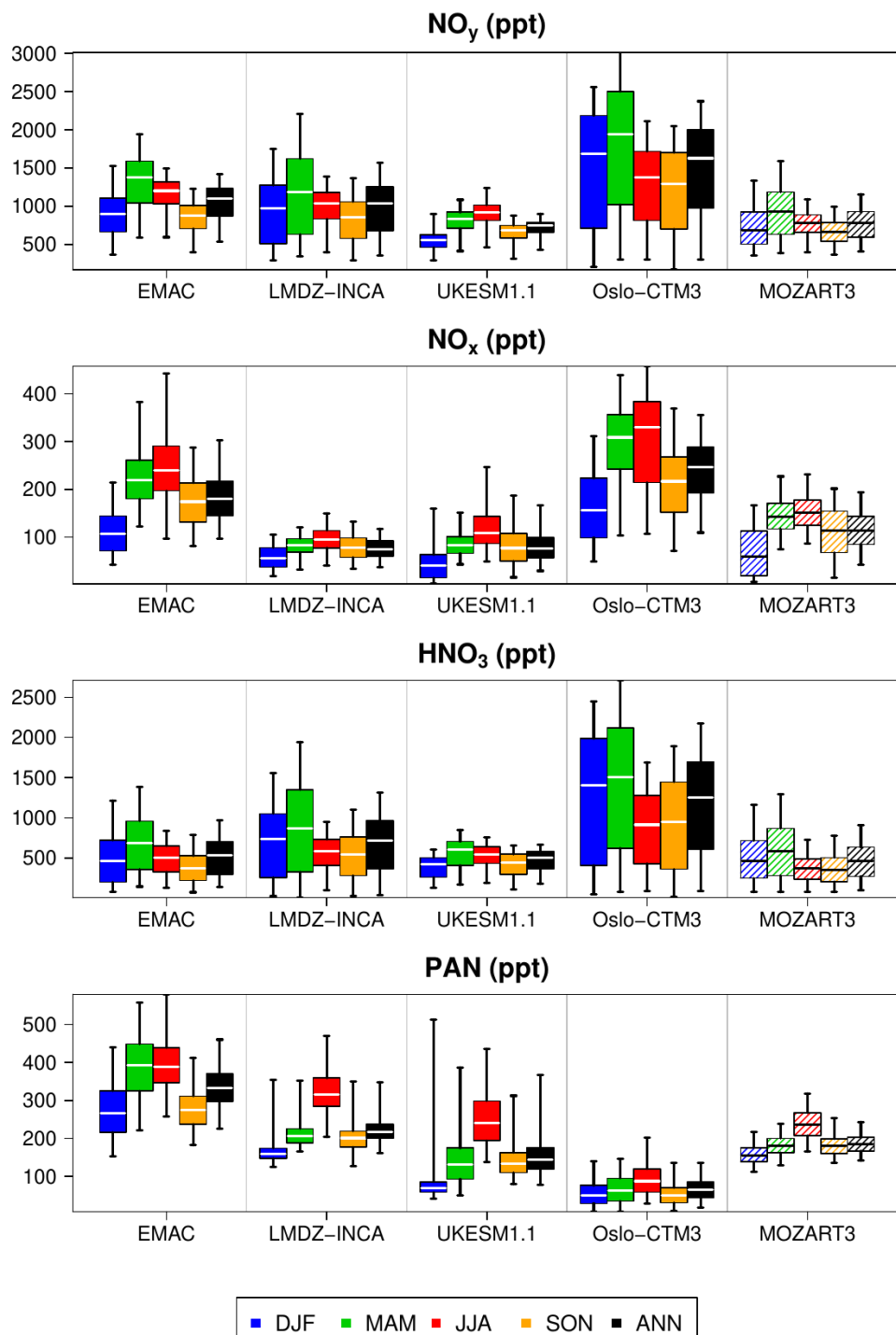
Figure B4. Boxplots synthesizing the contribution of NO_x, HNO_3 and PAN to NO_y levels shown in Fig. 9 in the non-separated UTLS, for the five model products. The upper panel is the same as in Fig. 9.

Appendix C: Seasonal assessment of modelled reactive species in the northern extra-tropics
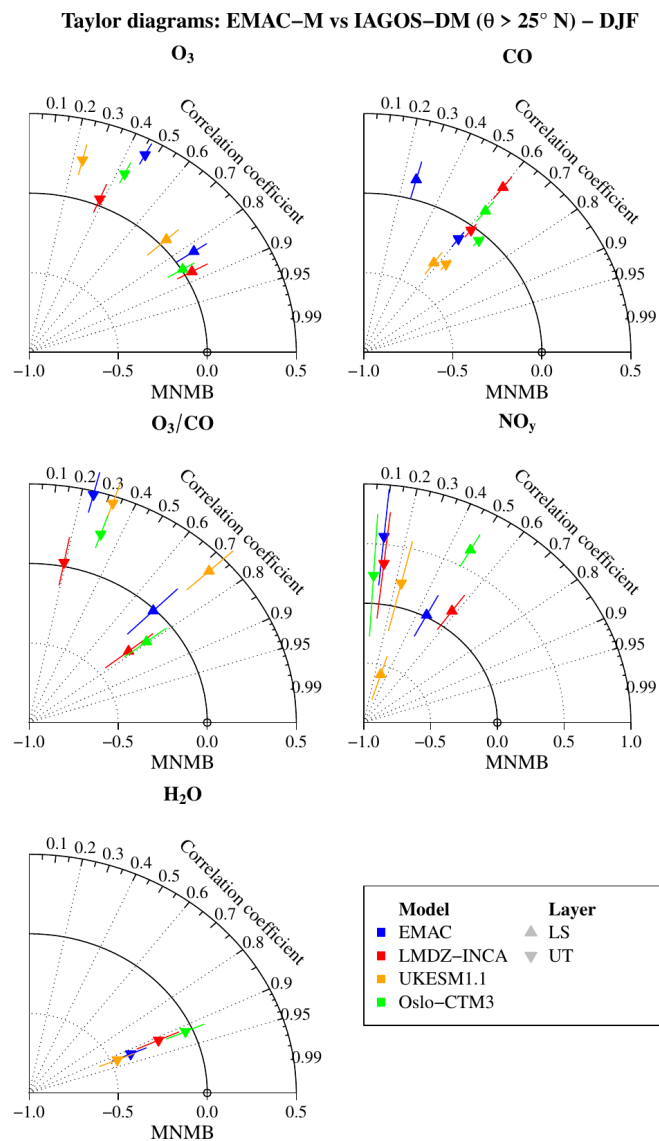
Figure C1. Same as Fig. 10 for boreal winter.
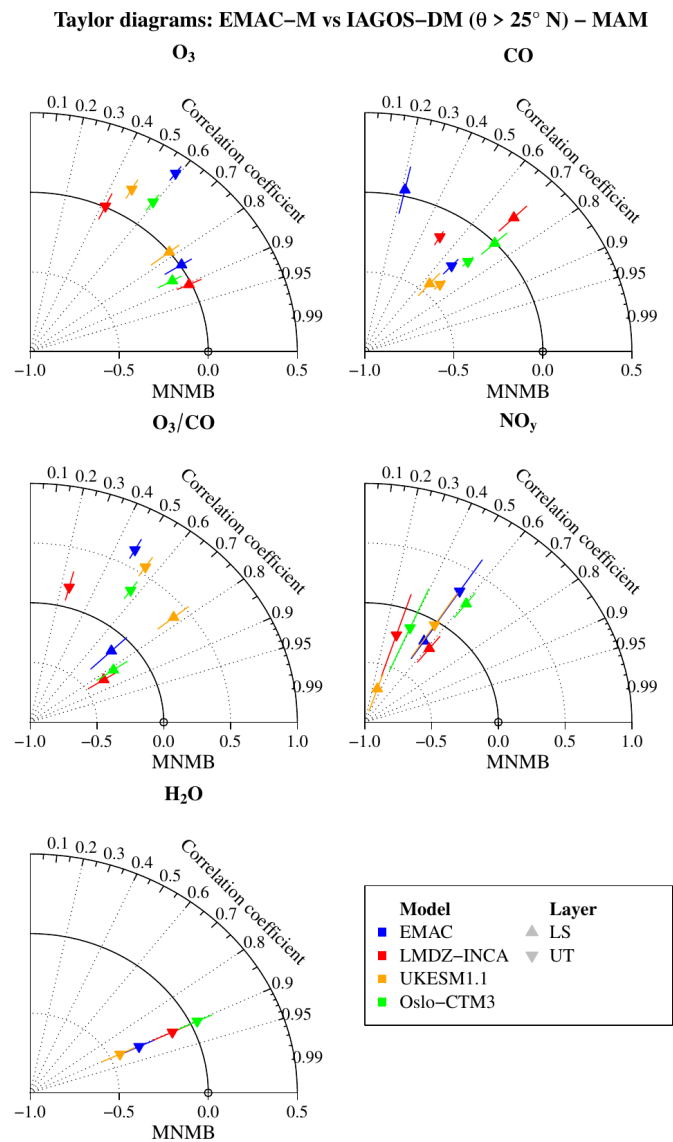
Figure C2. Same as Fig. 10 for boreal spring.
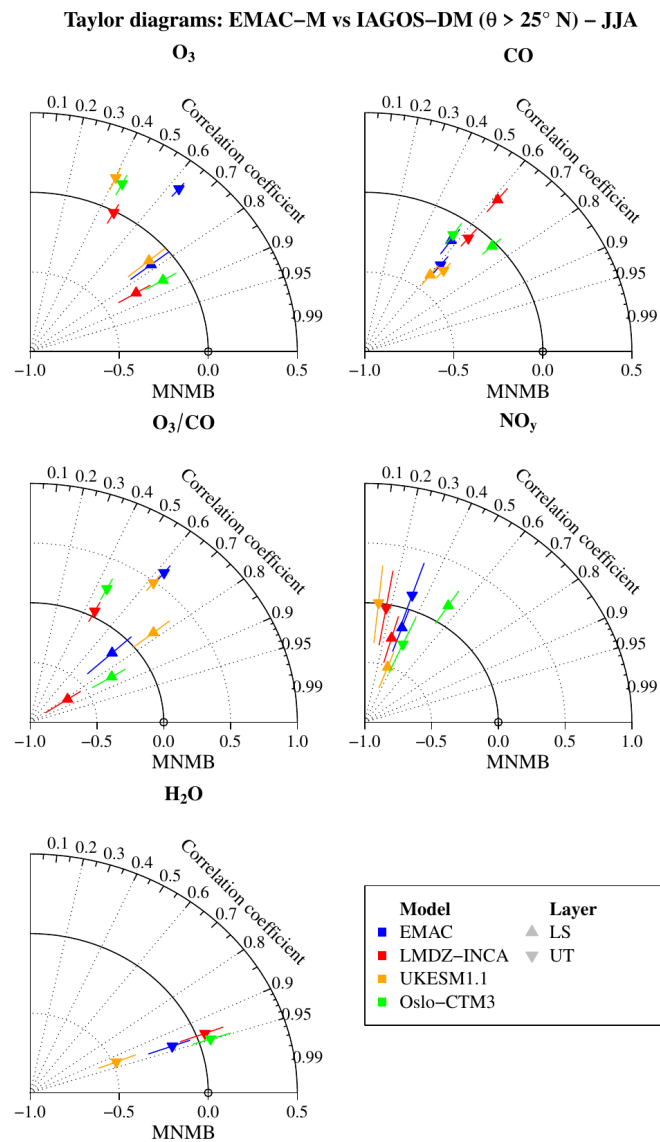
Figure C3. Same as Fig. 10 for boreal summer.
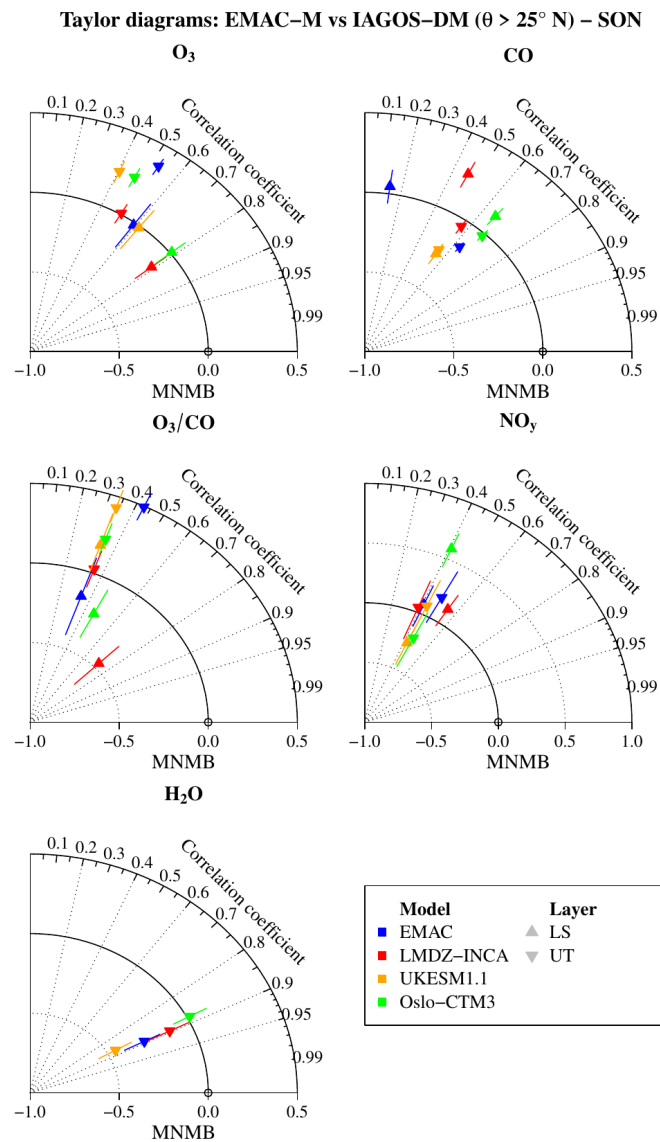
Figure C4. Same as Fig. 10 for boreal fall.

Code and data availability. The IAGOS data (IAGOS, 2022) are available at the IAGOS data portal (https://doi.org/10.25326/20) and more precisely, the time series data are found at https://doi.org/10.25326/06 (Boulanger et al., 2018). The Interpol-IAGOS software is available at https://doi.org/10.25326/81 (Cohen et al., 2020).

Author contributions. YC designed the study, and developed further the Interpol-IAGOS software. DH designed the modeling protocol shared by the models. The simulations output were provided by SM, RT for EMAC, YC and DH for LMDZ-INCA, AS for MOZART3, MTL for OsloCTM3, and NB for UKESM1.1. The IAGOS data were provided by VT, AP, SR, UB, AZ and HZ. The paper was written by YC and reviewed, commented, edited and approved by all the authors.

Acknowledgements. The authors acknowledge the strong support of the European Commission, Airbus, and the Airlines (Lufthansa, Air-France, Austrian, Air Namibia, Cathay Pacific, Iberia and China Airlines so far) who carry the IAGOS-CORE equipment and perform the maintenance since 1994. In its last 10 years of operation, IAGOS-CORE has been funded by INSU–CNRS (France), Météo-France, Université Paul Sabatier (Toulouse, France) and Research Center Jülich (FZJ, Jülich, Germany). IAGOS has been additionally funded by the EU projects IAGOS-DS and IAGOS-ERI. The IAGOS-CORE database is supported by AERIS. Data are also available on the AERIS web site www.aeris-data.fr. The simulations were performed using HPC resources from GENCI (Grand Équipement National de Calcul Intensif) under the gen2201 project. We also wish to acknowledge our colleagues from the IAGOS teams in FZJ, LAERO, DLR and KIT for all the preparation of the IAGOS and CARIBIC data used in this study. Notably for their contribution to the IAGOS–Core NO_y data, we thank their former PI Andreas Volz-Thomas, and Karin Thomas who was involved in the processing of the data.

Financial support. This research has been funded by the European Union Horizon 2020 research and innovation programme under the ACACIA (grant agreement no. 875036) project, and by the Direction Générale de l'Aviation Civile (DGAC) under the ClimAviation project. MTL acknowledges funding by the Research Council Norway (grant no. 300718 Aviate) and the resources from the National Infrastructure for High-Performance Computing and Data Storage in Norway (grant no. NN9188K).

Competing interests. At least one of the co-authors is a member of the editorial board of Atmospheric Chemistry and Physics.

References

Allen, D., Pickering, K., Duncan, B., and Damon, M.: Impact of lightning NO emissions on North American photochemistry as determined using the Global Modeling Initiative (GMI) model, J. Geophys. Res.-Atmos., 115, https://doi.org/10.1029/2010JD014062, 2010.

Archibald, A. T., O'Connor, F. M., Abraham, N. L., Archer-Nicholls, S., Chipperfield, M. P., Dalvi, M., Folberth, G. A., Dennison, F., Dhomse, S. S., Griffiths, P. T., Hardacre, C., Hewitt, A. J., Hill, R. S., Johnson, C. E., Keeble, J., Köhler, M. O., Morgenstern, O., Mulcahy, J. P., Ordóñez, C., Pope, R. J., Rumbold, S. T., Russo, M. R., Savage, N. H., Sellar, A., Stringer, M., Turnock, S. T., Wild, O., and Zeng, G.: Description and evaluation of the UKCA stratosphere–troposphere chemistry scheme (StratTrop vn 1.0) implemented in UKESM1, Geosci. Model Dev., 13, 1223–1266, https://doi.org/10.5194/gmd-13-1223-2020, 2020.

Berntsen, T. K. and Isaksen, I. S. A.: A global three-dimensional chemical transport model for the troposphere: 1. Model description and CO and ozone results, J. Geophys. Res.-Atmos., 102, 21 239–21 280, https://doi.org/10.1029/97JD01140, 1997.

Blot, R., Nédélec, P., Boulanger, D., Wolff, P., Sauvage, B., Cousin, J.-M., Athier, G., Zahn, A., Obersteiner, F., Scharffe, D., Petetin, H., Bennouna, Y., Clark, H., and Thouret, V.: Internal consistency of the IAGOS ozone and carbon monoxide measurements for the last 25 years, Atmos. Meas. Tech., 14, 3935–3951, https://doi.org/10.5194/amt-14-3935-2021, 2021.

Bojinski, S., Verstraete, M., Peterson, T. C., Richter, C., Simmons, A., and Zemp, M.: The Concept of Essential Climate Variables in Support of Climate Research, Applications, and Policy, B. Am. Meteorol. Soc., 95, 1431–1443, https://doi.org/10.1175/BAMS-D-13-00047.1, 2014.

Boulanger, D., Blot, R., Bundke, U., Gerbig, C., Hermann, M., Nédélec, P., Rohs, S., and Ziereis, H.: IAGOS time series, AERIS [data set], https://doi.org/10.25326/06, last access: 2022-10-06, 2018.

Brasseur, G. P., Hauglustaine, D. A., Walters, S., Rasch, P. J., Müller, J.-F., Granier, C., and Tie, X.: MOZART, a global chemical transport model for ozone and related tracers, Part 1: model description, J. Geophys. Res.-Atmos., 1998.

Brenninkmeijer, C. A. M., Crutzen, P. J., Fischer, H., Güsten, H., Hans, W., Heinrich, G., Heintzenberg, J., Hermann, M., Immelmann, T., Kersting, D., Maiss, M., Nolle, M., Pitscheider, A., Pohlkamp, H., Scharffe, D., Specht, K., and Wiedensohler, A.: CARIBIC–Civil Aircraft for Global Measurement of Trace Gases and Aerosols in the Tropopause Region, J. Atmos. Ocean Tech., 16, 1373–1383, https://doi.org/10.1175/1520-0426(1999)016<1373:CCAFGM>2.0.CO;2, 1999.

Brenninkmeijer, C. A. M., Crutzen, P., Boumard, F., Dauer, T., Dix, B., Ebinghaus, R., Filippi, D., Fischer, H., Franke, H., Frieß, U., Heintzenberg, J., Helleis, F., Hermann, M., Kock, H. H., Koeppel, C., Lelieveld, J., Leuenberger, M., Martinsson, B. G., Miemczyk, S., Moret, H. P., Nguyen, H. N., Nyfeler, P., Oram, D., O'Sullivan, D., Penkett, S., Platt, U., Pupek, M., Ramonet, M., Randa, B., Reichelt, M., Rhee, T. S., Rohwer, J., Rosenfeld, K., Scharffe, D., Schlager, H., Schumann, U., Slemr, F., Sprung, D., Stock, P., Thaler, R., Valentino, F., van Velthoven, P., Waibel, A., Wandel, A., Waschitschek, K., Wiedensohler, A., Xueref-Remy, I., Zahn, A., Zech, U., and Ziereis, H.: Civil Aircraft for the regular investigation of the atmosphere based on an instrumented container: The new CARIBIC system, Atmos. Chem. Phys., 7, 4953–4976, https://doi.org/10.5194/acp-7-4953-2007, 2007.

Brunner, D., Staehelin, J., Rogers, H. L., Köhler, M. O., Pyle, J. A., Hauglustaine, D., Jourdain, L., Berntsen, T. K., Gauss, M., Isaksen, I. S. A., Meijer, E., van Velthoven, P., Pitari, G., Mancini, E., Grewe, G., and Sausen, R.: An evaluation of the performance of chemistry transport models by comparison with research aircraft observations. Part 1: Concepts and overall model performance, Atmos. Chem. Phys., 3, 1609–1631, https://doi.org/10.5194/acp-3-1609-2003, 2003.

710 Cecil, D. J., Buechler, D. E., and Blakeslee, R. J.: Gridded lightning climatology from TRMM-LIS and OTD: Dataset description, Atmos. Res., 135-136, 404–414, https://doi.org/10.1016/j.atmosres.2012.06.028, 2014.

Cohen, Y., Petetin, H., Thouret, V., Marécal, V., Josse, B., Clark, H., Sauvage, B., Fontaine, A., Athier, G., Blot, R., Boulanger, D., Cousin, J.-M., and Nédélec, P.: Climatology and long-term evolution of ozone and carbon monoxide in the upper troposphere–lower stratosphere (UTLS) at northern midlatitudes, as seen by IAGOS from 1995 to 2013, Atmos. Chem. Phys., 18, 5415–5453, https://doi.org/10.5194/acp-18-5415-2018, 2018.

715 Cohen, Y., Thouret, V., Marécal, V., and Josse, B.: Interpol-IAGOS software, https://doi.org/10.25326/81, last access: 2022-10-06, 2020.

Cohen, Y., Marécal, V., Josse, B., and Thouret, V.: Interpol-IAGOS: a new method for assessing long-term chemistry–climate simulations in the UTLS based on IAGOS data, and its application to the MOCAGE CCMI REF-C1SD simulation, Geosci. Model Dev., 14, 2659–2689, https://doi.org/10.5194/gmd-14-2659-2021, 2021.

720 Cohen, Y., Hauglustaine, D., Sauvage, B., Rohs, S., Konjari, P., Bundke, U., Petzold, A., Thouret, V., Zahn, A., and Ziereis, H.: Evaluation of modelled climatologies of O_3, CO, water vapour and NO_y in the upper troposphere–lower stratosphere using regular in situ observations by passenger aircraft, Atmos. Chem. Phys., 23, 14 973–15 009, https://doi.org/10.5194/acp-23-14973-2023, 2023.

Cooper, O. R., Eckhardt, S., Crawford, J. H., Brown, C. C., Cohen, R. C., Bertram, T. H., Wooldridge, P., Perring, A., Brune, W. H., Ren, X., Brunner, D., and Baughcum, S. L.: Summertime buildup and decay of lightning NOx and aged thunderstorm outflow above North America, J. Geophys. Res.-Atmos., 114, https://doi.org/10.1029/2008JD010293, d01101, 2009.

725 Cristofanelli, P., Bracci, A., Sprenger, M., Marinoni, A., Bonafè, U., Calzolari, F., Duchi, R., Laj, P., Pichon, J. M., Roccato, F., Venzac, H., Vuillermoz, E., and Bonasoni, P.: Tropospheric ozone variations at the Nepal Climate Observatory-Pyramid (Himalayas, 5079 m a.s.l.) and influence of deep stratospheric intrusion events, Atmos. Chem. Phys., 10, 6537–6549, https://doi.org/10.5194/acp-10-6537-2010, 2010.

David, L. M., Ravishankara, A., Brewer, J. F., Sauvage, B., Thouret, V., Venkataramani, S., and Sinha, V.: Tropospheric ozone over the

730 Indian subcontinent from 2000 to 2015: Data set and simulation using GEOS-Chem chemical transport model, Atmos. Environ., 219, https://doi.org/10.1016/j.atmosenv.2019.117039, 2019.

de F. Forster, P. M. and Shine, K. P.: Radiative forcing and temperature trends from stratospheric ozone changes, J. Geophys. Res.-Atmos., 102, 10 841–10 855, https://doi.org/10.1029/96JD03510, 1997.

Deckert, R., Jöckel, P., Grewe, V., Gottschaldt, K.-D., and Hoor, P.: A quasi chemistry-transport model mode for EMAC, Geosci. Model

735 Dev., 4, 195–206, 2011.

Diallo, M., Ern, M., and Ploeger, F.: The advective Brewer–Dobson circulation in the ERA5 reanalysis: climatology, variability, and trends, Atmos. Chem. Phys., 21, 7515–7544, https://doi.org/10.5194/acp-21-7515-2021, 2021.

Dietmüller, S., Jöckel, P., Tost, H., Kunze, M., Gellhorn, C., Brinkop, S., Frömming, C., Ponater, M., Steil, B., Lauer, A., et al.: A new radiation infrastructure for the Modular Earth Submodel System (MESSy, based on version 2.51), Geosci. Model Dev., 9, 2209–2222, 2016.

Dyroff, C., Zahn, A., Christner, E., Forbes, R., Tompkins, A. M., and van Velthoven, P. F. J.: Comparison of ECMWF analysis and forecast humidity data with CARIBIC upper troposphere and lower stratosphere observations, Q. J. Roy. Meteor. Soc., 141, 833–844, https://doi.org/10.1002/qj.2400, 2015.

Eyring, V., Lamarque, J.-F., Hess, P., Arfeuille, F., Bowman, K., Chipperfield, M. P., Duncan, B., Fiore, A., Gettelman, A., Giorgetta, M. A., Granier, C., Hegglin, M., Kinnison, D., Kunze, M., Langematz, U., Luo, B., Martin, R., Matthes, K., Newman, P. A., Peter, T., Robock, A., Ryerson, T., Saiz-Lopez, A., Salawitch, A., Schultz, M., Shepherd, T. G., Shindell, D., Staehelin, J., Tegtmeier, S., Thomason, L., Tilmes, S., Vernier, J.-P., Waugh, D. W., and Young, P. J.: Overview of IGAC/SPARC Chemistry-Climate Model Initiative (CCMI) Community Simulations in Support of Upcoming Ozone and Climate Assessments, SPARC Newsletter, pp. 48–66, 2013.

Fadnavis, S., Semeniuk, K., Schultz, M. G., Kiefer, M., Mahajan, A., Pozzoli, L., and Sonbawane, S.: Transport pathways of peroxyacetyl nitrate in the upper troposphere and lower stratosphere from different monsoon systems during the summer monsoon season, Atmos. Chem. Phys., 15, 11 477–11 499, https://doi.org/10.5194/acp-15-11477-2015, 2015.

Finney, D. L., Doherty, R. M., Wild, O., Young, P. J., and Butler, A.: Response of lightning NO_x emissions and ozone production to climate change: Insights from the Atmospheric Chemistry and Climate Model Intercomparison Project, Geophys. Res. Lett., 43, 5492–5500, https://doi.org/10.1002/2016GL068825, 2016.

Folberth, G. A., Hauglustaine, D. A., Lathière, J., and Brocheton, F.: Interactive chemistry in the Laboratoire de Météorologie Dynamique general circulation model: model description and impact analysis of biogenic hydrocarbons on tropospheric chemistry, Atmos. Chem. Phys., 6, 2273–2319, https://doi.org/10.5194/acp-6-2273-2006, 2006.

Gaudel, A., Clark, H., Thouret, V., Jones, L., Inness, A., Flemming, J., Stein, O., Huijnen, V., Eskes, H., Nédélec, P., and Boulanger, D.: On the use of MOZAIC-IAGOS data to assess the ability of the MACC reanalysis to reproduce the distribution of ozone and CO in the UTLS over Europe, Tellus B, 67, 27 955, https://doi.org/10.3402/tellusb.v67.27955, 2015.

Gettelman, A., Hegglin, M. I., Son, S.-W., Kim, J., Fujiwara, M., Birner, T., Kremser, S., Rex, M., Añel, J. A., Akiyoshi, H., Austin, J., Bekki, S., Braesike, P., Brühl, C., Butchart, N., Chipperfield, M., Dameris, M., Dhomse, S., Garny, H., Hardiman, S. C., Jöckel, P., Kinnison, D. E., Lamarque, J. F., Mancini, E., Marchand, M., Michou, M., Morgenstern, O., Pawson, S., Pitari, G., Plummer, D., Pyle, J. A., Rozanov, E., Scinocca, J., Shepherd, T. G., Shibata, K., Smale, D., Teyssèdre, H., and Tian, W.: Multimodel assessment of the upper troposphere and lower stratosphere: Tropics and global trends, J. Geophys. Res.-Atmos., 115, https://doi.org/10.1029/2009JD013638, d00M08, 2010.

Gettelman, A., Hoor, P., Pan, L. L., Randel, W. J., Hegglin, M. I., and Birner, T.: The extratropical upper troposphere and lower stratosphere, Rev. Geophys., 49, https://doi.org/10.1029/2011RG000355, rG3003, 2011.

Giannakopoulos, C., Chipperfield, T., Law, K., and Pyle, J.: Validation and intercomparison of wet and dry deposition schemes using Pb-210 in a global three-dimensional off-line chemical transport model, J. Geophys. Res., 104, 23 761—23 784, 1999.

770 Gidden, M. J., Riahi, K., Smith, S. J., Fujimori, S., Luderer, G., Kriegler, E., van Vuuren, D. P., van den Berg, M., Feng, L., Klein, D., Calvin, K., Doelman, J. C., Frank, S., Fricko, O., Harmsen, M., Hasegawa, T., Havlik, P., Hilaire, J., Hoesly, R., Horing, J., Popp, A., Stehfest, E., and Takahashi, K.: Global emissions pathways under different socioeconomic scenarios for use in CMIP6: a dataset of harmonized emissions trajectories through the end of the century, Geosci. Model Dev., 12, 1443–1475, https://doi.org/10.5194/gmd-12-1443-2019, 2019.

775 Gottschaldt, K.-D., Schlager, H., Baumann, R., Cai, D. S., Eyring, V., Graf, P., Grewe, V., Jöckel, P., Jurkat-Witschas, T., Voigt, C., Zahn, A., and Ziereis, H.: Dynamics and composition of the Asian summer monsoon anticyclone, Atmos. Chem. Phys., 18, 5655–5675, https://doi.org/10.5194/acp-18-5655-2018, 2018.

Granier, C., Lamarque, J.-F., Mieville, A., Muller, J.-F., Olivier, J., Orlando, J., Peters, J., Petron, G., Tyndall, G., and Wallens, S.: POET, a database of surface emissions of ozone precursors, 2005.

780 Grewe, V., Brunner, D., Dameris, M., Grenfell, J., Hein, R., Shindell, D., and Staehelin, J.: Origin and variability of upper tropospheric nitrogen oxides and ozone at northern mid-latitudes, Atmos. Environ., 35, 3421–3433, https://doi.org/10.1016/S1352-2310(01)00134-0, 2001.

Grooß, J.-U. and Russell III, J. M.: Technical note: A stratospheric climatology for O_3, H_2O, CH_4, NO_x, HCl and HF derived from HALOE measurements, Atmos. Chem. Phys., 5, 2797–2807, https://doi.org/10.5194/acp-5-2797-2005, 2005.

785 Grooß, J.-U., Brühl, C., and Peter, T.: Impact of aircraft emissions on tropospheric and stratospheric ozone. Part I: chemistry and 2-D model results, Atmos. Environ., 32, 3173–3184, https://doi.org/10.1016/S1352-2310(98)00016-8, 1998.

Guth, J., Josse, B., Marécal, V., Joly, M., and Hamer, P.: First implementation of secondary inorganic aerosols in the MOCAGE version R2.15.0 chemistry transport model, Geosci. Model Dev., 9, 137–160, https://doi.org/10.5194/gmd-9-137-2016, 2016.

Hack, J. J.: Parameterization of moist convection in the NCAR community climate model (CCM2), J. Geophys. Res.-Atmos., 99, 5833–5866,
790 https://doi.org/10.1029/93JD03478, 1994.

Hakim, Z. Q., Archer-Nicholls, S., Beig, G., Folberth, G. A., Sudo, K., Abraham, N. L., Ghude, S., Henze, D. K., and Archibald, A. T.: Evaluation of tropospheric ozone and ozone precursors in simulations from the HTAPII and CCMI model intercomparisons – a focus on the Indian subcontinent, Atmos. Chem. Phys., 19, 6437–6458, https://doi.org/10.5194/acp-19-6437-2019, 2019.

Hauglustaine, D. A., Hourdin, F., Jourdain, L., Filiberti, M.-A., Walters, S., Lamarque, J.-F., and Holland, E. A.: Interactive chemistry in
795 the Laboratoire de Météorologie Dynamique general circulation model: Description and background tropospheric chemistry evaluation, J. Geophys. Res.-Atmos., 109, https://doi.org/10.1029/2003JD003957, 2004.

Hauglustaine, D. A., Balkanski, Y., and Schulz, M.: A global model simulation of present and future nitrate aerosols and their direct radiative forcing of climate, Atmos. Chem. Phys., 14, 11 031–11 063, https://doi.org/10.5194/acp-14-11031-2014, 2014.

Hegglin, M. I., Gettelman, A., Hoor, P., Krichevsky, R., Manney, G. L., Pan, L. L., Son, S.-W., Stiller, G., Tilmes, S., Walker, K. A., Eyring,
800 V., Shepherd, T. G., Waugh, D., Akiyoshi, H., Añel, J. A., Austin, J., Baumgaertner, A., Bekki, S., Braesicke, P., Brühl, C., Butchart, N., Chipperfield, M., Dameris, M., Dhomse, S., Frith, S., Garny, H., Hardiman, S. C., Jöckel, P., Kinnison, D. E., Lamarque, J.-F., Mancini,

E., Michou, M., Morgenstern, O., Nakamura, T., Olivié, D., Pawson, S., Pitari, G., Plummer, D. A., Pyle, J. A., Rozanov, E., Scinocca, J. F., Shibata, K., Smale, D., Teyssèdre, H., Tian, W., and Yamashita, Y.: Multimodel assessment of the upper troposphere and lower stratosphere: Extratropics, J. Geophys. Res.-Atmos., 115, https://doi.org/10.1029/2010JD013884, 2010.

805 Helten, M., Smit, H. G. J., Sträter, W., Kley, D., Nédélec, P., Zöger, M., and Busen, R.: Calibration and performance of automatic compact instrumentation for the measurement of relative humidity from passenger aircraft, J. Geophys. Res.-Atmos., 103, 25 643–25 652, https://doi.org/10.1029/98JD00536, 1998.

Hesstvedt, E., Hov, O., and Isaksen, I. S. A.: Quasi-steady-state approximations in air pollution modeling: Comparison of two numerical schemes for oxidant prediction, Int. J. Chem. Kinetics, 10, 971–994, https://doi.org/10.1002/kin.550100907, 1978.

810 Hodnebrog, Ø., Berntsen, T. K., Dessens, O., Gauss, M., Grewe, V., Isaksen, I. S. A., Koffi, B., Myhre, G., Olivié, D., Prather, M. J., Pyle, J. A., Stordal, F., Szopa, S., Tang, Q., van Velthoven, P., Williams, J. E., and Ødemark, K.: Future impact of non-land based traffic emissions on atmospheric ozone and OH – an optimistic scenario and a possible mitigation strategy, Atmos. Chem. Phys., 11, 11 293–11 317, https://doi.org/10.5194/acp-11-11293-2011, 2011.

Hodnebrog, Ø., Berntsen, T. K., Dessens, O., Gauss, M., Grewe, V., Isaksen, I. S. A., Koffi, B., Myhre, G., Olivié, D., Prather, M. J., Stordal, 815 F., Szopa, S., Tang, Q., van Velthoven, P., and Williams, J. E.: Future impact of traffic emissions on atmospheric ozone and OH based on two scenarios, Atmos. Chem. Phys., 12, 12 211–12 225, https://doi.org/10.5194/acp-12-12211-2012, 2012.

Hoesly, R. M., Smith, S. J., Feng, L., Klimont, Z., Janssens-Maenhout, G., Pitkanen, T., Seibert, J. J., Vu, L., Andres, R. J., Bolt, R. M., Bond, T. C., Dawidowski, L., Kholod, N., Kurokawa, J.-I., Li, M., Liu, L., Lu, Z., Moura, M. C. P., O'Rourke, P. R., and Zhang, Q.: Historical (1750–2014) anthropogenic emissions of reactive gases and aerosols from the Community Emissions Data System (CEDS), 820 Geosci. Model Dev., 11, 369–408, https://doi.org/10.5194/gmd-11-369-2018, 2018.

Holtslag, A. and Boville, B. A.: Local versus nonlocal boundary-layer diffusion in a global climate model, J. Clim., 6, 1825—-1842, https://doi.org/10.1175/1520-0442(1993)006<1825:LVNBLD>2.0.CO;2, 1993.

Holtslag, A. A. M., De Bruijn, E. I. F., and Pan, H.-L.: A high resolution air mass transformation model for short-range weather forecasting, Mon. Weather Rev., 118, 1561–1575, https://doi.org/10.1175/1520-0493(1990)118<1561:AHRAMT>2.0.CO;2, 1990.

825 Hoor, P., Borken-Kleefeld, J., Caro, D., Dessens, O., Endresen, O., Gauss, M., Grewe, V., Hauglustaine, D., Isaksen, I. S. A., Jöckel, P., Lelieveld, J., Myhre, G., Meijer, E., Olivié, D., Prather, M., Schnadt Poberaj, C., Shine, K. P., Staehelin, J., Tang, Q., van Aardenne, J., van Velthoven, P., and Sausen, R.: The impact of traffic emissions on atmospheric ozone and OH: results from QUANTIFY, Atmos. Chem. Phys., 9, 3113–3136, https://doi.org/10.5194/acp-9-3113-2009, 2009.

Hourdin, F., Musat, I., Bony, S., Braconnot, P., Codron, F., Dufresne, J.-L., Fairhead, L., Filiberti, M.-A., Friedlingstein, P., Grandpeix, J.-Y., 830 Krinner, G., LeVan, P., Li, Z.-X., and Lott, F.: The LMDZ4 general circulation model: climate performance and sensitivity to parametrized physics with emphasis on tropical convection, Clim. Dynam., 27, https://doi.org/10.1007/s00382-006-0158-0, 2006.

IAGOS: IAGOS-Core and IAGOS-CARIBIC data, available at:, http://www.iagos.org/, last access: 2022-10-06, 2022.

Iglesias-Suarez, F., Kinnison, D. E., Rap, A., Maycock, A. C., Wild, O., and Young, P. J.: Key drivers of ozone change and its radiative forcing over the 21st century, Atmos. Chem. Phys., 18, 6121–6139, https://doi.org/10.5194/acp-18-6121-2018, 2018.

835 Jöckel, P., Kerkweg, A., Pozzer, A., Sander, R., Tost, H., Riede, H., Baumgaertner, A., Gromov, S., and Kern, B.: Development cycle 2 of the Modular Earth Submodel System (MESSy2), Geosci. Model Dev., 3, 717–752, 2010.

Jöckel, P., Tost, H., Pozzer, A., Kunze, M., Kirner, O., Brenninkmeijer, C. A. M., Brinkop, S., Cai, D. S., Dyroff, C., Eckstein, J., Frank, F., Garny, H., Gottschaldt, K.-D., Graf, P., Grewe, V., Kerkweg, A., Kern, B., Matthes, S., Mertens, M., Meul, S., Neumaier, M., Nützel, M., Oberländer-Hayn, S., Ruhnke, R., Runde, T., Sander, R., Scharffe, D., and Zahn, A.: Earth System Chemistry integrated Modelling (ES-

840 CiMo) with the Modular Earth Submodel System (MESSy) version 2.51, Geosci. Model Dev., 9, 1153–1200, https://doi.org/10.5194/gmd-9-1153-2016, 2016.

Joppe, P., Schneider, J., Kaiser, K., Fischer, H., Hoor, P., Kunkel, D., Lachnitt, H.-C., Marsing, A., Röder, L., Schlager, H., Tomsche, L., Voigt, C., Zahn, A., and Borrmann, S.: The influence of extratropical cross-tropopause mixing on the correlation between ozone and sulfate aerosol in the lowermost stratosphere, EGUsphere, 2024, 1–28, https://doi.org/10.5194/egusphere-2024-7, 2024.

845 Josse, B., Simon, P., and Peuch, V.-H.: Radon global simulations with the multiscale chemistry and transport model MOCAGE, Tellus B, 56, 339–356, https://doi.org/10.3402/tellusb.v56i4.16448, 2004.

Jourdain, L. and Hauglustaine, D. A.: The global distribution of lightning NO_x simulated on-line in a general circulation model, Physics and Chemistry of the Earth, Part C: Solar, Terrestrial & Planetary Science, 26, 585–591, https://doi.org/10.1016/S1464-1917(01)00051-4, 2001.

850 Kinnison, D. E., Brausser, G. P., Walters, S., Garcia, R. R., Marsh, D. R., Sassi, F., Harvey, V. L., Randall, C. E., Emmons, L., Lamarque, J. F., Hess, P., Orlando, J. J., Tie, X. X., Randel, W., Pan, L. L., Gettelman, A., Granier, C., Diehl, T., Niemeier, U., and Simmons, A. J.: Sensitivity of chemical tracers to meteorological parameters in the MOZART-3 chemical transport model, J. Geophys. Res.-Atmos., 112, D20 302, https://doi.org/10.1029/2006JD007879, 2007.

Krinner, G., Viovy, N., de Noblet-Ducoudré, N., Ogée, J., Polcher, J., Friedlingstein, P., Ciais, P., Sitch, S., and Prentice, I. C.:

855 A dynamic global vegetation model for studies of the coupled atmosphere-biosphere system, Global Biogeochem. Cy., 19, https://doi.org/10.1029/2003GB002199, 2005.

Lacis, A. A., Wuebbles, D. J., and Logan, J. A.: Radiative forcing of climate by changes in the vertical distribution of ozone, J. Geophys. Res.-Atmos., 95, 9971–9981, https://doi.org/10.1029/JD095iD07p09971, 1990.

Lamarque, J.-F., Shindell, D. T., Josse, B., Young, P. J., Cionni, I., Eyring, V., Bergmann, D., Cameron-Smith, P., Collins, W. J., Doherty, R.,

860 Dalsoren, S., Faluvegi, G., Folberth, G., Ghan, S. J., Horowitz, L. W., Lee, Y. H., MacKenzie, I. A., Nagashima, T., Naik, V., Plummer, D., Righi, M., Rumbold, S. T., Schulz, M., Skeie, R. B., Stevenson, D. S., Strode, S., Sudo, K., Szopa, S., Voulgarakis, A., and Zeng, G.: The Atmospheric Chemistry and Climate Model Intercomparison Project (ACCMIP): overview and description of models, simulations and climate diagnostics, Geosci. Model Dev., 6, 179–206, https://doi.org/10.5194/gmd-6-179-2013, 2013.

Lannuque, V., Sauvage, B., Barret, B., Clark, H., Athier, G., Boulanger, D., Cammas, J.-P., Cousin, J.-M., Fontaine, A., Le Flochmoën, E.,
865   Nédélec, P., Petetin, H., Pfaffenzeller, I., Rohs, S., Smit, H. G. J., Wolff, P., and Thouret, V.: Origins and characterization of CO and O_3
     in the African upper troposphere, Atmos. Chem. Phys., 21, 14 535–14 555, https://doi.org/10.5194/acp-21-14535-2021, 2021.

Law, K. S., Plantevin, P.-H., Thouret, V., Marenco, A., Asman, W. A. H., Lawrence, M., Crutzen, P. J., Muller, J.-F., Hauglustaine, D. A., and
     Kanakidou, M.: Comparison between global chemistry transport model results and Measurement of Ozone and Water Vapor by Airbus
     In-Service Aircraft (MOZAIC) data, J. Geophys. Res.-Atmos., 105, 1503–1525, https://doi.org/10.1029/1999JD900474, 2000.

870 Lee, D., Fahey, D., Skowron, A., Allen, M., Burkhardt, U., Chen, Q., Doherty, S., Freeman, S., Forster, P., Fuglestvedt, J., Get-
     telman, A., De León, R., Lim, L., Lund, M., Millar, R., Owen, B., Penner, J., Pitari, G., Prather, M., Sausen, R., and Wilcox,
     L.: The contribution of global aviation to anthropogenic climate forcing for 2000 to 2018, Atmos. Environ., 244, 117 834,
     https://doi.org/10.1016/j.atmosenv.2020.117834, 2021.

Li, Y., Dhomse, S. S., Chipperfield, M. P., Feng, W., Chrysanthou, A., Xia, Y., and Guo, D.: Effects of reanalysis forcing fields on ozone
875   trends and age of air from a chemical transport model, Atmos. Chem. Phys., 22, 10 635–10 656, https://doi.org/10.5194/acp-22-10635-
     2022, 2022.

Lin, S. J. and Rood, R. B.: A fast flux form semi-Lagrangian transport scheme on the sphere, Mon. Weather Rev., 124, 2046–2070,
     https://doi.org/10.1175/1520- 0493(1996)124<2046:MFFSLT>2.0.CO;2, 1996.

Liu, Y., Liu, C. X., Wang, H. P., Tie, X. X., Gao, S. T., Kinnison, D., and Brasseur, G.: Atmospheric tracers during the 2003–2004 stratospheric
880   warming event and impact of ozone intrusions in the troposphere, Atmos. Chem. Phys., 9, 2157–2170, https://doi.org/10.5194/acp-9-2157-
     2009, 2009.

Livesey, N. J., Logan, J. A., Santee, M. L., Waters, J. W., Doherty, R. M., Read, W. G., Froidevaux, L., and Jiang, J. H.: Interrelated
     variations of O_3, CO and deep convection in the tropical/subtropical upper troposphere observed by the Aura Microwave Limb Sounder
     (MLS) during 2004–2011, Atmos. Chem. Phys., 13, 579–598, https://doi.org/10.5194/acp-13-579-2013, 2013.

885 Lund, M. T., Myhre, G., Haslerud, A. S., Skeie, R. B., Griesfeller, J., Platt, S. M., Kumar, R., Myhre, C. L., and Schulz, M.: Concentrations
     and radiative forcing of anthropogenic aerosols from 1750 to 2014 simulated with the Oslo CTM3 and CEDS emission inventory, Geosci.
     Model Dev., 11, 4909–4931, https://doi.org/10.5194/gmd-11-4909-2018, 2018.

Marenco, A., Thouret, V., Nédélec, P., Smit, H., Helten, M., Kley, D., Karsher, F., Simon, P., Law, K., Pyle, J., Poschmann, G., Von Wrede,
     R., Hume, C., and Cook, T.: Measurement of ozone and water vapour by Airbus in-service aircraft : The MOZAIC airborne programme,
890   an overview, J. Geophys. Res., 103, 25 631–25 642, https://doi.org/10.1029/98JD00977, 1998.

Messina, P., Lathière, J., Sindelarova, K., Vuichard, N., Granier, C., Ghattas, J., Cozic, A., and Hauglustaine, D. A.: Global biogenic volatile
     organic compound emissions in the ORCHIDEE and MEGAN models and sensitivity to key parameters, Atmos. Chem. Phys., 16, 14 169–
     14 202, https://doi.org/10.5194/acp-16-14169-2016, 2016.

Millán, L. F., Hoor, P., Hegglin, M. I., Manney, G. L., Boenisch, H., Jeffery, P., Kunkel, D., Petropavlovskikh, I., Ye, H., Leblanc, T., and Walker, K.: Exploring ozone variability in the upper troposphere and lower stratosphere using dynamical coordinates, EGUsphere, 2024, 1–45, https://doi.org/10.5194/egusphere-2024-144, 2024.

Morgenstern, O., Braesicke, P., O'Connor, F. M., Bushell, A. C., Johnson, C. E., Osprey, S. M., and Pyle, J. A.: Evaluation of the new UKCA climate-composition model – Part 1: The stratosphere, Geosci. Model Dev., 2, 43–57, https://doi.org/10.5194/gmd-2-43-2009, 2009.

Mulcahy, J. P., Jones, C., Sellar, A., Johnson, B., Boutle, I. A., Jones, A., Andrews, T., Rumbold, S. T., Mollard, J., Bellouin, N., Johnson, C. E., Williams, K. D., Grosvenor, D. P., and McCoy, D. T.: Improved aerosol processes and effective radiative forcing in HadGEM3 and UKESM1, J. Adv. Model. Earth Sys., 10, 2786–2805, https://doi.org/10.1029/2018MS001464, 2018.

Murray, L. T., Jacob, D. J., Logan, J. A., Hudman, R. C., and Koshak, W. J.: Optimized regional and interannual variability of lightning in a global chemical transport model constrained by LIS/OTD satellite data, J. Geophys. Res.-Atmos., 117, https://doi.org/10.1029/2012JD017934, 2012.

Müller, J.-F.: Geographical distribution and seasonal variation of surface emissions and deposition velocities of atmospheric trace gases, J. Geophys. Res.-Atmos., 97, 3787–3804, https://doi.org/10.1029/91JD02757, 1992.

Nédélec, P., Cammas, J.-P., Thouret, V., Athier, G., Cousin, J.-M., Legrand, C., Abonnel, C., Lecoeur, F., Cayez, G., and Marizy, C.: An improved infrared carbon monoxide analyser for routine measurements aboard commercial Airbus aircraft: technical validation and first scientific results of the MOZAIC III programme, Atmos. Chem. Phys., 3, 1551–1564, https://doi.org/10.5194/acp-3-1551-2003, 2003.

Nédélec, P., Blot, R., Boulanger, D., Athier, G., Cousin, J.-M., Gautron, B., Petzold, A., Volz-Thomas, A., and Thouret, V.: Instrumentation on commercial aircraft for monitoring the atmospheric composition on a global scale: the IAGOS system, technical overview of ozone and carbon monoxide measurements, Tellus B, 67, 27 791, https://doi.org/10.3402/tellusb.v67.27791, 2015.

Neis, P., Smit, H. G. J., Krämer, M., Spelten, N., and Petzold, A.: Evaluation of the MOZAIC Capacitive Hygrometer during the airborne field study CIRRUS-III, Atmos. Meas. Tech., 8, 1233–1243, https://doi.org/10.5194/amt-8-1233-2015, 2015a.

Neis, P., Smit, H. G. J., Rohs, S., Bundke, U., Krämer, M., Spelten, N., Ebert, V., Buchholz, B., Thomas, K., and Petzold, A.: Quality assessment of MOZAIC and IAGOS capacitive hygrometers: insights from airborne field studies, Tellus B, 67, https://doi.org/10.3402/tellusb.v67.28320, 2015b.

Neu, J. L., Prather, M. J., and Penner, J. E.: Global atmospheric chemistry: Integrating over fractional cloud cover, J. Geophys. Res.-Atmos., 112, https://doi.org/10.1029/2006JD008007, 2007.

Nussbaumer, C. M., Fischer, H., Lelieveld, J., and Pozzer, A.: What controls ozone sensitivity in the upper tropical troposphere?, Atmos. Chem. Phys., 23, 12 651–12 669, https://doi.org/10.5194/acp-23-12651-2023, 2023.

O'Connor, F. M., Johnson, C. E., Morgenstern, O., Abraham, N. L., Braesicke, P., Dalvi, M., Folberth, G. A., Sanderson, M. G., Telford, P. J., Voulgarakis, A., Young, P. J., Zeng, G., Collins, W. J., and Pyle, J. A.: Evaluation of the new UKCA climate-composition model – Part 2: The Troposphere, Geosci. Model Dev., 7, 41–91, https://doi.org/10.5194/gmd-7-41-2014, 2014.

925   Orbe, C., Plummer, D. A., Waugh, D. W., Yang, H., Jöckel, P., Kinnison, D. E., Josse, B., Marecal, V., Deushi, M., Abraham, N. L., Archibald, A. T., Chipperfield, M. P., Dhomse, S., Feng, W., and Bekki, S.: Description and Evaluation of the specified-dynamics experiment in the Chemistry-Climate Model Initiative, Atmos. Chem. Phys., 20, 3809–3840, https://doi.org/10.5194/acp-20-3809-2020, 2020.

Ott, L. E., Pickering, K. E., Stenchikov, G. L., Allen, D. J., DeCaria, A. J., Ridley, B., Lin, R.-F., Lang, S., and Tao, W.-K.: Production of lightning NO_x and its vertical distribution calculated from three-dimensional cloud-scale chemical transport model simulations, J.

930   Geophys. Res.-Atmos., 115, https://doi.org/10.1029/2009JD011880, 2010.

Pätz, H.-W., Volz-Thomas, A., Hegglin, M. I., Brunner, D., Fischer, H., and Schmidt, U.: In-situ comparison of the NO_y instruments flown in MOZAIC and SPURT, Atmos. Chem. Phys., 6, 2401–2410, https://doi.org/10.5194/acp-6-2401-2006, 2006.

Petzold, A., Thouret, V., Gerbig, C., Zahn, A., Brenninkmeijer, C., Gallagher, M., Hermann, M., Pontaud, M., Ziereis, H., Boulanger, D., Marshall, J., Nédélec, P., Smit, H., Friess, U., Flaud, J.-M., Wahner, A., Cammas, J.-P., and Volz-Thomas, A.: Global-scale atmosphere

935   monitoring by in-service aircraft - current achievements and future prospects of the European Research Infrastructure IAGOS, Tellus B, 67, https://doi.org/10.3402/tellusb.v67.28452, 2015.

Petzold, A., Neis, P., Rütimann, M., Rohs, S., Berkes, F., Smit, H. G. J., Krämer, M., Spelten, N., Spichtinger, P., Nédélec, P., and Wahner, A.: Ice-supersaturated air masses in the northern mid-latitudes from regular in situ observations by passenger aircraft: vertical distribution, seasonality and tropospheric fingerprint, Atmos. Chem. Phys., 20, 8157–8179, https://doi.org/10.5194/acp-20-8157-2020, 2020.

940   Pickering, K. E., Wang, Y. S., Tao, W. K., Price, C., and Müller, J.: Vertical distributions of lightning NOx for use in regional and global chemical transport models, J. Geophys. Res.-Atmos, 103, 31 203–31 216, https://doi.org/10.1029/98JD02651, 1998.

Pletzer, J., Hauglustaine, D., Cohen, Y., Jöckel, P., and Grewe, V.: The climate impact of hydrogen-powered hypersonic transport, Atmos. Chem. Phys., 22, 14 323–14 354, https://doi.org/10.5194/acp-22-14323-2022, 2022.

Ploeger, F., Diallo, M., Charlesworth, E., Konopka, P., Legras, B., Laube, J. C., Grooß, J.-U., Günther, G., Engel, A., and Riese, M.:

945   The stratospheric Brewer–Dobson circulation inferred from age of air in the ERA5 reanalysis, Atmos. Chem. Phys., 21, 8393–8412, https://doi.org/10.5194/acp-21-8393-2021, 2021.

Prather, M. J.: Numerical advection by conservation of second-order moments, J. Geophys.Res.-Atmos., 91, 6671–6681, https://doi.org/10.1029/JD091iD06p06671, 1986.

Prather, M. J.: Fast-JX version 6.5, http://www.ess.uci.edu/~prather/fastJX.html, last access: 1 September 2009, 2009.

950   Price, C. and Rind, D.: A simple lightning parameterization for calculating global lightning distributions, J. Geophys. Res.-Atmos., 97, 9919–9933, https://doi.org/10.1029/92JD00719, 1992.

Price, C., Penner, J., and Prather, M.: NOx from lightning: 1. Global distribution based on lightning physics, J. Geophys. Res.-Atmos., 102, 5929–5941, https://doi.org/10.1029/96JD03504, 1997.

Riese, M., Ploeger, F., Rap, A., Vogel, B., Konopka, P., Dameris, M., and Forster, P.: Impact of uncertainties in atmospheric mixing on

955   simulated UTLS composition and related radiative effects, J. Geophys. Res., 117, D16 305, https://doi.org/10.1029/2012JD017751, 2012.

Righi, M., Eyring, V., Gottschaldt, K.-D., Klinger, C., Frank, F., Jöckel, P., and Cionni, I.: Quantitative evaluation of ozone and selected climate parameters in a set of EMAC simulations, Geosci. Model Dev., 8, 733–768, https://doi.org/10.5194/gmd-8-733-2015, 2015.

Roeckner, E., Brokopf, R., Esch, M., Giorgetta, M., Hagemann, S., Kornbaleh, L., Manzini, E., Schlese, U., and Schulzweida, U.: Sensitivity of Simulated Climate to Horizontal and Vertical Resolution in the ECHAM5 Atmosphere Model, J. Clim., 19, 3771–3791, https://doi.org/10.1175/JCLI3824.1, 2006.

Rolf, C., Rohs, S., Smit, H., G.J., Krämer, M., Bozóki, Z., Hofmann, S., Franke, H., Maser, R., Hoor, P., and Petzold, A.: Evaluation of compact hygrometers for continuous airborne measurements, Meteorol. Z., https://doi.org/10.1127/metz/2023/1187, 2023.

Russo, M. R., Kerridge, B. J., Abraham, N. L., Keeble, J., Latter, B. G., Siddans, R., Weber, J., Griffiths, P. T., Pyle, J. A., and Archibald, A. T.: Seasonal, interannual and decadal variability of tropospheric ozone in the North Atlantic: comparison of UM-UKCA and remote sensing observations for 2005–2018, Atmos. Chem. Phys., 23, 6169–6196, https://doi.org/10.5194/acp-23-6169-2023, 2023.

Sander, R., Baumgaertner, A., Cabrera-Perez, D., Frank, F., Gromov, S., Grooß, J.-U., Harder, H., Huijnen, V., Jöckel, P., Karydis, V. A., et al.: The community atmospheric chemistry box model CAABA/MECCA-4.0, Geosci. Model Dev., 12, 1365–1385, 2019.

Sander, S. P., Golden, D. M., Kurylo, M. J., Moortgat, G. K., Wine, P. H., Ravishankara, A. R., Kolb, C. E., Molina, M. J., Finlayson-Pitts, B. J., Huie, R. E., Orkin, V. L., Friedl, R. R., and Keller-Rudek, H.: Chemical kinetics and photochemical data for use in atmospheric studies : evaluation number 15, https://doi.org/2014/39839, last access: 6 September 2006, 2006.

Sauvage, B., Thouret, V., Cammas, J.-P., Brioude, J., Nédélec, P., and Mari, C.: Meridional ozone gradients in the African upper troposphere, Geophys. Res. Lett., 34, https://doi.org/10.1029/2006GL028542, l03817, 2007.

Sauvage, B., Fontaine, A., Eckhardt, S., Auby, A., Boulanger, D., Petetin, H., Paugam, R., Athier, G., Cousin, J.-M., Darras, S., Nédélec, P., Stohl, A., Turquety, S., Cammas, J.-P., and Thouret, V.: Source attribution using FLEXPART and carbon monoxide emission inventories: SOFT-IO version 1.0, Atmos. Chem. Phys., 17, 15 271–15 292, https://doi.org/10.5194/acp-17-15271-2017, 2017.

Scharffe, D., Slemr, F., Brenninkmeijer, C. A. M., and Zahn, A.: Carbon monoxide measurements onboard the CARIBIC passenger aircraft using UV resonance fluorescence, Atmos. Meas. Tech., 5, 1753–1760, https://doi.org/10.5194/amt-5-1753-2012, 2012.

Sellar, A. A., Jones, C. G., Mulcahy, J. P., Tang, Y., Yool, A., Wiltshire, A., O'Connor, F. M., Stringer, M., Hill, R., Palmieri, J., Woodward, S., de Mora, L., Kuhlbrodt, T., Rumbold, S. T., Kelley, D. I., Ellis, R., Johnson, C. E., Walton, J., Abraham, N. L., Andrews, M. B., Andrews, T., Archibald, A. T., Berthou, S., Burke, E., Blockley, E., Carslaw, K., Dalvi, M., Edwards, J., Folberth, G. A., Gedney, N., Griffiths, P. T., Harper, A. B., Hendry, M. A., Hewitt, A. J., Johnson, B., Jones, A., Jones, C. D., Keeble, J., Liddicoat, S., Morgenstern, O., Parker, R. J., Predoi, V., Robertson, E., Siahaan, A., Smith, R. S., Swaminathan, R., Woodhouse, M. T., Zeng, G., and Zerroukat, M.: UKESM1: Description and Evaluation of the U.K. Earth System Model, J. Adv. Model. Earth Sys., 11, 4513–4558, https://doi.org/10.1029/2019MS001739, 2019.

Skowron, A., Lee, D. S., and De León, R. R.: Variation of radiative forcings and global warming potentials from regional aviation NO_x/emissions, Atmos. Environ., 104, https://doi.org/10.1016/j.atmosenv.2014.12.043, 2015.

Skowron, A., Lee, D. S., De León, R. R., Lim, L. L., and Owen, B.: Greater fuel efficiency is potentially preferable to reducing NO_x/emissions for aviation's climate impacts, Nature Comm., 12, https://doi.org/10.1038/s41467-020-20771-3, 2021.

Smit, H. G. J., Rohs, S., Neis, P., Boulanger, D., Krämer, M., Wahner, A., and Petzold, A.: Technical Note: Reanalysis of upper troposphere humidity data from the MOZAIC programme for the period 1994 to 2009, Atmos. Chem. Phys., 14, 13 241–13 255, https://doi.org/10.5194/acp-14-13241-2014, 2014.

Søvde, O. A., Prather, M. J., Isaksen, I. S. A., Berntsen, T. K., Stordal, F., Zhu, X., Holmes, C. D., and Hsu, J.: The chemical transport model Oslo CTM3, Geosci. Model Dev., 5, 1441–1469, https://doi.org/10.5194/gmd-5-1441-2012, 2012.

Søvde, O. A., Matthes, S., Skowron, A., Iachetti, D., Lim, L., Owen, B., Hodnebrog, Ø., Di Genova, G., Pitari, G., Lee, D. S., Myhre, G., and Isaksen, I. S.: Aircraft emission mitigation by changing route altitude: A multi-model estimate of aircraft NO_x emission impact on O_3 photochemistry, Atmos. Env., 95, 468–479, https://doi.org/10.1016/j.atmosenv.2014.06.049, 2014.

Stordal, F., Isaksen, I. S. A., and Horntveth, K.: A diabatic circulation two-dimensional model with photochemistry: Simulations of ozone and long-lived tracers with surface sources, J. Geophys. Res.-Atmos., 90, 5757–5776, https://doi.org/10.1029/JD090iD03p05757, 1985.

Stratmann, G., Ziereis, H., Stock, P., Brenninkmeijer, C., Zahn, A., Rauthe-Schöch, A., Velthoven, P., Schlager, H., and Volz-Thomas, A.: {NO} and {NOy} in the upper troposphere: Nine years of {CARIBIC} measurements onboard a passenger aircraft, Atmos. Environ., 133, 93–111, https://doi.org/10.1016/j.atmosenv.2016.02.035, 2016.

Terrenoire, E., Hauglustaine, D. A., Cohen, Y., Cozic, A., Valorso, R., Lefèvre, F., and Matthes, S.: Impact of present and future aircraft NO_x and aerosol emissions on atmospheric composition and associated direct radiative forcing of climate, Atmos. Chem. Phys., 22, 11 987–12 023, https://doi.org/10.5194/acp-22-11987-2022, 2022.

Thor, R. N., Mertens, M., Matthes, S., Righi, M., Hendricks, J., Brinkop, S., Graf, P., Grewe, V., Jöckel, P., and Smith, S.: An inconsistency in aviation emissions between CMIP5 and CMIP6 and the implications for short-lived species and their radiative forcing, Geosci. Model Dev., 16, 1459–1466, https://doi.org/10.5194/gmd-16-1459-2023, 2023.

Thouret, V., Marenco, A., Logan, J. A., Nédélec, P., and Grouhel, C.: Comparisons of ozone measurements from the MOZAIC airborne program and the ozone sounding network at eight locations, J. Geophys. Res., 103, 25 695–25 720, https://doi.org/10.1029/98JD02243, 1998.

Thouret, V., Cammas, J.-P., Sauvage, B., Athier, G., Zbinden, R. M., Nédélec, P., Simon, P., and Karcher, F.: Tropopause referenced ozone climatology and inter-annual variability (1994–2003) from the MOZAIC programme, Atmos. Chem. Phys., 6, 1033–1051, https://doi.org/10.5194/acp-6-1033-2006, 2006.

Tiedtke, M.: A comprehensive mass flux scheme for cumulus parameterization in large-scale models, Mon. Weather Rev., 117, 1779 – 1800, https://doi.org/10.1175/1520-0493(1989)117<1779:ACMFSF>2.0.CO;2, 1989.

Tilmes, S., Pan, L. L., Hoor, P., Atlas, E., Avery, M. A., Campos, T., Christensen, L. E., Diskin, G. S., Gao, R.-S., Herman, R. L., Hintsa, E. J., Loewenstein, M., Lopez, J., Paige, M. E., Pittman, J. V., Podolske, J. R., Proffitt, M. R., Sachse, G. W., Schiller, C., Schlager, H.,

Smith, J., Spelten, N., Webster, C., Weinheimer, A., and Zondlo, M. A.: An aircraft-based upper troposphere lower stratosphere O_3, CO, and H_2O climatology for the Northern Hemisphere, J. Geophys. Res.-Atmos., 115, https://doi.org/10.1029/2009JD012731, d14303, 2010.

1020   Tilmes, S., Lamarque, J.-F., Emmons, L. K., Kinnison, D. E., Marsh, D., Garcia, R. R., Smith, A. K., Neely, R. R., Conley, A., Vitt, F., Val Martin, M., Tanimoto, H., Simpson, I., Blake, D. R., and Blake, N.: Representation of the Community Earth System Model (CESM1) CAM4-chem within the Chemistry-Climate Model Initiative (CCMI), Geosci. Model Dev., 9, 1853–1890, https://doi.org/10.5194/gmd-9-1853-2016, 2016.

van Marle, M. J. E., Kloster, S., Magi, B. I., Marlon, J. R., Daniau, A.-L., Field, R. D., Arneth, A., Forrest, M., Hantson, S., Kehrwald, N. M.,
1025   Knorr, W., Lasslop, G., Li, F., Mangeon, S., Yue, C., Kaiser, J. W., and van der Werf, G. R.: Historic global biomass burning emissions for CMIP6 (BB4CMIP) based on merging satellite observations with proxies and fire models (1750–2015), Geosci. Model Dev., 10, 3329–3357, https://doi.org/10.5194/gmd-10-3329-2017, 2017.

Volz-Thomas, A., Berg, M., Heil, T., Houben, N., Lerner, A., Petrick, W., Raak, D., and Pätz, H.-W.: Measurements of total odd nitrogen (NO_y) aboard MOZAIC in-service aircraft: instrument design, operation and performance, Atmos. Chem. Phys., 5, 583–595,
1030   https://doi.org/10.5194/acp-5-583-2005, 2005.

Walters, D., Baran, A. J., Boutle, I., Brooks, M., Earnshaw, P., Edwards, J., Furtado, K., Hill, P., Lock, A., Manners, J., Morcrette, C., Mulcahy, J., Sanchez, C., Smith, C., Stratton, R., Tennant, W., Tomassini, L., Van Weverberg, K., Vosper, S., Willett, M., Browse, J., Bushell, A., Carslaw, K., Dalvi, M., Essery, R., Gedney, N., Hardiman, S., Johnson, B., Johnson, C., Jones, A., Jones, C., Mann, G., Milton, S., Rumbold, H., Sellar, A., Ujiie, M., Whitall, M., Williams, K., and Zerroukat, M.: The Met Office Unified Model Global
1035   Atmosphere 7.0/7.1 and JULES Global Land 7.0 configurations, Geosci. Model Dev., 15, 1909–1963, https://doi.org/10.5194/gmd-12-1909-2019, 2019.

Wuebbles, D. J., Patten, K. O., Wang, D., Youn, D., Martínez-Avilés, M., and Francisco, J. S.: Three-dimensional model evaluation of the ozone depletion potentials for n-propyl bromide, trichloroethylene and perchloroethylen, Atmos. Chem. Phys., 11, 2371–2380, https://doi.org/10.5194/acp-11-2371-2011, 2011.

1040   Young, P. J., Naik, V., Fiore, A. M., Gaudel, A., Guo, J., Lin, M. Y., Neu, J. L., Parrish, D. D., Rieder, H. E., Schnell, J. L., Tilmes, S., Wild, O., Zhang, L., Ziemke, J. R., Brandt, J., Delcloo, A., Doherty, R. M., Geels, C., Hegglin, M. I., Hu, L., Im, U., Kumar, R., Luhar, A., Murray, L., Plummer, D., Rodriguez, J., Saiz-Lopez, A., Schultz, M. G., Woodhouse, M. T., and Zeng, G.: Tropospheric Ozone Assessment Report: Assessment of global-scale model performance for global and regional ozone distributions, variability, and trends, Elem. Sci. Anth., 6, https://doi.org/10.1525/elementa.265, 2018.

1045   Zahn, A., Weppner, J., Widmann, H., Schlote-Holubek, K., Burger, B., Kühner, T., and Franke, H.: A fast and precise chemiluminescence ozone detector for eddy flux and airborne application, Atmos. Meas. Tech., 5, 363–375, https://doi.org/10.5194/amt-5-363-2012, 2012.

Zahn, A., Christner, E., van Velthoven, P. F. J., Rauthe-Schöch, A., and Brenninkmeijer, C. A. M.: Processes controlling water vapor in the upper troposphere/lowermost stratosphere: An analysis of 8 years of monthly measurements by the IAGOS-CARIBIC observatory, J. Geophys. Res.-Atmos., 119, 11,505–11,525, https://doi.org/10.1002/2014JD021687, 2014JD021687, 2014.

1050   Zhang, G. J. and McFarlane, N. A.: Sensitivity of climate simulations to the parameterization of cumulus convection in the Canadian climate centre general circulation model, Atmos.-Ocean, 33, 407–446, https://doi.org/10.1080/07055900.1995.9649539, 1995.

Ziereis, H., Schlager, H., Schulte, P., van Velthoven, P. F. J., and Slemr, F.: Distributions of NO, NO_x , and NO_y in the upper troposphere and lower stratosphere between $28°$ and $61°$ N during POLINAT 2, J. Geophys. Res.-Atmos., 105, 3653–3664, https://doi.org/10.1029/1999JD900870, 2000.